

Mirror Thermal Noise in Interferometric Gravitational Wave Detectors

Thesis by
Shanti R. Rao

In Partial Fulfillment of the Requirements
for the Degree of
Doctor of Philosophy



California Institute of Technology
Pasadena, California

2003
(Defended May 15, 2003)

© 2003

Shanti R. Rao

All Rights Reserved

Acknowledgements

Thank you to Ken Libbrecht and Eric Black for supporting me and turning me loose on a lab full of expensive toys, and to the whole LIGO family for their constant encouragement, especially Matt Evans, Jim Mason, Phil Willems, Alan Weinstein, and Stan Whitcomb for their guidance, Jay Heefner for teaching me how to build low-noise electronics, and Rich and Ben Abbott for helping me with all those nifty gizmos. Seiji Kawamura's assistance on the TNI was invaluable, and Vladimir Braginsky and Richard O'Shaughnessy helped me understand the photothermal data.

I am indebted to many people at the University of Washington for getting me started in physics: Chris Stubbs, Norval Fortson, Mike Schick, Henry Lubatti, Steve Ellis, David Bowler, and Heinz Guldenmann, who taught me much of what I know about metal.

My friends at Caltech made this work worth doing. Thanks go to Samantha Edgington, Michael Hartl, and Luke Sollitt for cheering me on toward the end, Keith Matthews for teaching me how to love Los Angeles, James Boyk and Delores Bing for teaching me about Art, Cheryl von Buskirk, Jennifer Ottesen, Paul Rothemun, and Jasper Simon for entertaining me, Jen Shively for introducing me to orchids, the Penultimate Frisbee Club for keeping me in shape, and the Prufrock Dinner Group for keeping me company.

Most of all, thank you to Martha Kirouac for loving me and for proofreading this, and thank you to my parents for always encouraging me to be different.

Finally, thank you to the American taxpayers for funding this work. Experimental physics is an expensive undertaking, and I hope I can give them a good return on their investment. The LIGO Observatories were constructed by the California Institute of Technology and Massachusetts Institute of Technology with funding from the National Science Foundation under cooperative agreement PHY 9210038. The LIGO Laboratory operates under cooperative agreement PHY-0107417. This thesis has been assigned LIGO Document Number LIGO-P030025.

Abstract

The LIGO (Laser Interferometer Gravitational-wave Observatory) project has begun its search for gravitational waves, and efforts are being made to improve its ability to detect these. The LIGO observatories are long, Fabry-Perot-Michelson interferometers, where the interferometer mirrors are also the gravitational wave test masses. LIGO is designed to detect the ripples in spacetime caused by cataclysmic astrophysical events, with a target gravitational wave minimum strain sensitivity of 4×10^{-22} [7] around 100 Hz. The Advanced LIGO concept [57] calls for an order of magnitude improvement in strain sensitivity, with a better signal to noise ratio to increase the rate of detection of events. Some of Advanced LIGO's major requirements are improvements over the LIGO design for thermal noise in the test mass substrates and reflective coatings [57].

Thermal noise in the interferometer mirrors is a significant challenge in LIGO's development. This thesis reviews the theory of test mass thermal noise and reports on several experiments conducted to understand this theory.

Experiments to measure the thermal expansion of mirror substrates and coatings use the photothermal effect in a cross-polarized Fabry-Perot interferometer, with displacement sensitivity of 10^{-15} m/rHz. Data are presented from 10 Hz to 4kHz on solid aluminum, and on sapphire, BK7, and fused silica, with and without commercial $\text{TiO}_2/\text{SiO}_2$ dielectric mirror coatings. The substrate contribution to thermal expansion is compared to theories by Cerdonio *et al.* [32] and Braginsky, Vyatchanin, and Gorodetsky [22]. New theoretical models are presented for estimating the coating contribution to the thermal expansion. These results can also provide insight into how heat flows between coatings and substrates relevant to predicting coating thermoelastic noise [26, 108].

The Thermal Noise Interferometer (TNI) project is a interferometer built specifically to study thermal noise, and this thesis describes its construction and commissioning. Using LIGO-like designs, components, and processes, the TNI has a minimum length noise in each of two arm cavities of 5×10^{-18} m/rHz around 1 kHz.

Contents

Acknowledgements	iii
Abstract	iv
1 Introduction	1
2 Theory of Thermal Noise	5
2.1 Introduction	5
2.2 Background	7
2.2.1 Spectral densities	7
2.2.2 Thermal length scales	8
2.3 Intrinsic noise	8
2.3.1 The fluctuation-dissipation theorem	9
2.3.2 Bulk internal friction	10
2.3.3 Coating structural damping	11
2.3.4 Bulk thermoelastic noise	12
2.3.5 Coating thermoelastic noise	13
2.3.6 Coating thermorefractive noise	15
2.3.7 Bulk thermorefractive noise	15
2.4 Photon-driven noise	16
2.4.1 Bulk expansion	16
2.4.2 Coating expansion	17
2.4.2.1 High-conductivity substrates	18
2.4.2.2 Low-conductivity substrates	21
2.4.2.3 Photothermal noise summary	23
2.4.3 Coating dn/dT	23

2.5	Summary	26
3	The Photothermal Effect	28
3.1	Introduction	28
3.2	Materials and Methods	30
	3.2.0.1 Aluminum measurements	30
	3.2.0.2 BK7, Fused Silica, Sapphire	32
	3.2.1 Mode matching	35
	3.2.2 Polarization optics	36
	3.2.3 Alignment	37
	3.2.4 Length sensing, control, and calibration	39
	3.2.5 Components	43
	3.2.5.1 Mounting hardware	43
	3.2.5.2 Photodiode	43
	3.2.5.3 Laser	45
	3.2.5.4 Chopper	46
	3.2.5.5 Cavity	47
	3.2.6 Sample preparation	48
	3.2.6.1 Aluminum	50
	3.2.6.2 BK7	50
	3.2.6.3 Sapphire	51
	3.2.6.4 Fused silica	51
	3.2.7 Experimental procedure	51
	3.2.7.1 Configurations	51
	3.2.7.2 Data acquisition	53
	3.2.7.3 Computation	55
	3.2.7.4 Scattering	56
	3.2.7.5 Power absorption	56
	3.2.7.6 Systematic errors	58
3.3	Results	61
	3.3.1 Aluminum	62
	3.3.2 Sapphire	65

3.3.3	BK7	68
3.3.4	Fused silica	70
3.3.5	Summary	73
4	The Thermal Noise Interferometer	75
4.1	Introduction	75
4.2	Design	75
4.2.1	Optics	76
4.2.2	Mode cleaner	78
4.2.3	Arm cavity mirrors	78
4.2.4	Mechanics	81
4.2.4.1	Seismic isolation	81
4.2.4.2	Suspensions	81
4.3	Mode cleaner and laser servo	81
4.4	Local damping	84
4.5	Vacuum equipment	85
4.6	Results and summary	86
5	Summary	88
	Appendix	90
5.1	Coating photothermal effect in low-conductivity substrates	90
5.2	Cross-coupling noise	92
5.3	Interferometer identities	95
5.4	TNI	96
5.4.1	Mode cleaner electronics	96
5.4.2	Alignment procedure	97
5.5	Calibration procedure	98
5.5.1	OSEM optimization procedure	98
5.5.2	Venting the vacuum chamber	99
	Bibliography	101

Chapter 1

Introduction

Astronomy has a curious position in human society. Once essential for daily commerce, it now figures in the minds of most people as a source of pretty pictures in the newspaper. What then for gravitational radiation? Often hailed as a “new window on the universe,” gravitational waves promise to tell us about massive compact objects in the universe that we might not find by conventional optical astronomy. The state-of-the-art gravitational wave (GW) detectors are long-baseline Michelson interferometers with Fabry-Perot arms (see Fig. 1.1): the LIGO [1, 8], GEO [58], TAMA [119], and VIRGO [44] observatories. Located around the globe, they wait for ripples in spacetime to shake their test mass mirrors, indicating distant cataclysmic events like supernovae [87, 120] and mergers among black holes and neutron stars [11, 47].

To search for astrophysical events, GW detectors are intended to run continuously, recording what they observe. Events are identified by comparing the data stream from the detectors to matched filter templates based on astrophysical models [21, 98]. Combining data from multiple observatories [37] helps to suppress false positives. Algorithms for searching the data for events improve [4, 100], but advancements in the ability to identify and understand faint GW events still depends on lower-noise instruments [64]. With that goal in mind, can better detectors be built?

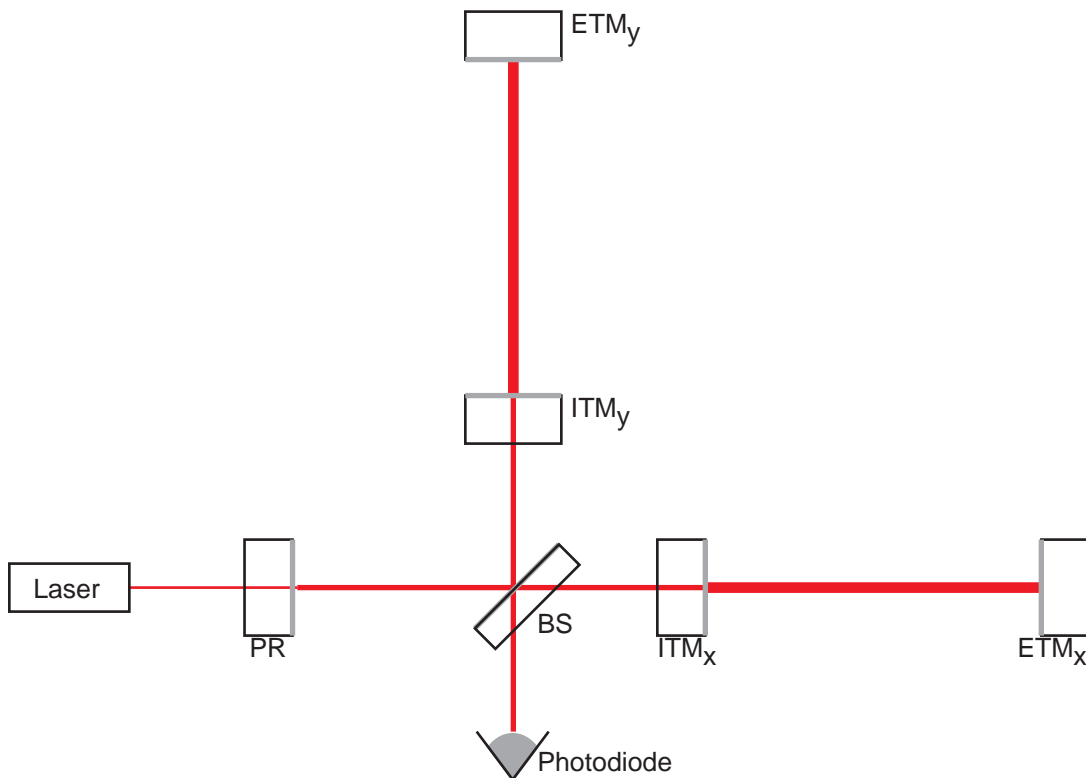
GWs appear at earth as a strain in spacetime, and it’s predicted that, every year, a few waves pass through the earth with strength $h \sim 10^{-21}$ to 10^{-22} at around 100 Hz [11, 117], based on estimated abundances of compact binary objects in other galaxies. Detector projects have made great strides in reducing instrument noise: in 1991, the detectable GW strain was $h \sim 4 \times 10^{-19}$ in resonant bars [59], and LIGO reported a noise level of $h \sim 3 \times 10^{-22}$ in 2003 [109]. Note that there is a difference between a detector’s noise level and the detectable GW strain. An interferometer’s noise level is where the signal to noise ratio (S/N) equal to one. With the LIGO observatories combined and the S/N threshold set to 5, the detectable GW strain is 11 times higher than the noise in a single

interferometer, when the incoming waves are averaged over all angles and polarizations [57].

As the current generation of GW interferometers advances [109], they draw closer to fundamental limits to detector noise. One of these limits appears to be thermal noise: at non-zero temperature, everything vibrates, which can overwhelm the gravitational signal from a burst event and can impede the ability to observe stochastic background events [64]. The LIGO masses are large transparent cylinders of fused silica, 25 cm diameter by 10 cm thick [14, 71], coated with thin reflective dielectric mirrors¹. In these test masses, the major ways that intrinsic thermal noise is believed to arise is through thermoelastic damping and internal friction, which have been observed in two-arm interferometers in bulk materials [55, 94]. Thermal noise in the mirror coatings themselves is also

¹The mirror coatings in LIGO are quarter-wave stacks of $\text{Ta}_2\text{O}_5/\text{SiO}_2$. The coating thicknesses are 16 layers or 2.3×10^{-6} m on input test masses, and 40 layers or 5.8×10^{-6} m on end test masses [72].

Figure 1.1: Power-recycled GW detector. The x and y arms are Fabry-Perot cavities, made from an Input Test Mass (ITM) and an End Test Mass (ETM). With the beam splitter (BS), these form a Michelson interferometer, with the photodiode operating at the dark fringe. A power recycling (PR) mirror is at the bright fringe. In early 2003, the LIGO 4k interferometers operated with this configuration, with 2.3 kW circulating in each arm cavity [72]. Gray lines on the test mass edges represent high-reflectivity dielectric mirror coatings.



a concern, and is being investigated [26, 38, 60, 82, 108]. The GW community has devoted considerable effort to modelling these noise sources, and Chapter 2 reviews several current theories of mirror thermal noise. Special attention is paid to photoelastic noise, for which I present two models for the contribution from mirror coatings. Table 2.2 on page 27 is a convenient summary of many of the current theories.

The test mirrors in the LIGO interferometers invariably absorb a small amount of the light that strikes them, so there are light-induced noise sources in addition to intrinsic thermal noise. As the light itself is subject to photon shot noise and other intensity variations, this absorption process leads to mirror noise. Such absorption could affect an interferometer through fluctuating thermal expansion of the mirror surface [22, 32], known in the literature as the photothermal effect. A similar mechanism is the photorefractive (dn/dT) effect [23], in which optical heating changes the indices of refraction of multi-layer dielectric mirrors, causing variations in the phase shift of the light reflected from a mirror.²

The photothermal effect can be measured directly, by optically heating a mirror and measuring its length change in an interferometer. The theory for this effect in homogenous mirrors has been derived by Cerdonio *et al.* [32], and De Rosa *et al.* [106] have measured the bulk expansion in low-absorption (0.5 ppm) dielectric mirrors at low frequencies (10 mHz - 200 Hz). The extension of these measurements up to several kHz would allow the exploration of the LIGO and Advanced LIGO [57] frequency bands, and the examination of what happens in the mirror coatings — thermal expansion coefficients for the dielectric mirrors are expected to be much larger than for substrates [26].

In Chapter 3, I describe an instrument designed to measure the photothermal effect in an interferometer. In experiments with this instrument, I examine samples of sapphire, BK7, and fused silica, with and without high-reflectivity dielectric mirrors. To ensure that they have similar optical absorptivity and reflectivity, all the samples are coated with a thin layer of gold. To measure their photothermal response, two laser beams with orthogonal polarizations resonate in a Fabry-Perot cavity made from a sample and a reference mirror. One laser beam has its intensity modulated to heat the sample, while the second beam measures the length change of the cavity due to thermal expansion of the sample. The modulation frequency is varied from 10 Hz to 4 kHz to map out

²The term photothermal is ambiguous. It may refer purely to thermal expansion, or it may refer to a combination of thermal expansion and dn/dT , which is often the case for thin film thermal expansion coefficient measurements found in the literature [118]. In this thesis, “photothermal” refers solely to thermal expansion, with no index of refraction contribution.

the photothermal effect across the LIGO frequency band. From the results, I show that the coating makes a significant contribution to the thermal expansion of the mirror, particularly at high frequencies.

Many types of thermal noise can not be excited directly, and to measure these in low-noise materials requires a low-noise instrument. Chapter 4 describes the construction and the commissioning of LIGO's Thermal Noise Interferometer (TNI) [15] project, built to study thermal noise and evaluate new test mass materials in a small laboratory. The TNI's objective is to measure the differential noise between two suspended arm cavities with mirrors that are smaller than those used in LIGO but of a similar quality. The TNI helps identify the significant engineering challenges to building a fundamental noise limited interferometer by adopting designs, components, and processes from LIGO. While not obviously limited by thermal noise, the TNI's sensitivity is close to the expected level of thermal noise as of this writing.

The LIGO project, its collaborators, and its contemporaries seek continually to improve GW detection technology. The purpose of this work is to provide a measurement of the photothermal effect, information about the role that dielectric mirror coatings may play in mirror thermal noise, and tools with which to learn more about mirror thermal noise in interferometric gravitational wave detectors.

Chapter 2

Theory of Thermal Noise

2.1 Introduction

What we call thermal noise in LIGO's mirrors falls naturally into two broad categories of sources.

- Intrinsic (dissipative) noise is driven by thermal forcing from internal fluctuations. A mirror's *dissipation* describes coupling of a mechanical (or chemical, or electrical, etc...) motion to a heat reservoir. Just as this loss converts mechanical energy to thermal energy, random thermal fluctuations are spontaneously converted back to mechanical fluctuations, as described by the fluctuation-dissipation theorem (FDT) of Callen and Welton [29, 28]. Some types of thermal noise can be easily identified with temperature: thermal energy fluctuates [76, 78], and material properties such as length and index of refraction fluctuate with it.
- Extrinsic (non-dissipative) noise arises when externally imposed temperature variations drive thermal fluctuations. For instance, the mirror may absorb heat from a laser beam with fluctuating intensity, causing length changes by thermal expansion.

How these sources affect gravitational wave detection depends on where they appear. LIGO test masses are thin dielectric mirrors grown on top of thick, transparent substrates. Besides gravitational waves, the center of mass of the substrates can be moved by radiation pressure [99, 111], seismic noise [51, 105], changes in local gravity [65], and the people who work at the observatories [116]. But light senses the position of the mirror coating, not the position of the center of mass of the substrate, so there are also noise sources which appear at the mirror surfaces. Some types of mirror thermal noise, such as bulk internal friction (see §2.3.2), depend mostly on the properties of the substrate, while many depend on the coating, which is, in general, quite different from the substrate.

- The substrate has dimensions comparable to or larger than the laser spot size. It is a high-Q mechanical resonator made from high-purity, highly transparent glass or crystal.
- The dielectric mirror coating is only a few microns thick. While mirror substrates are carefully chosen for their low thermal noise and good performance, mirror coating materials are chosen mostly for their indices of refraction, and do not necessarily have high mechanical Qs or low thermal expansion.

The LIGO mirrors are made of quarter-wave stacks of $\text{Ta}_2\text{O}_5/\text{SiO}_2$, and a major uncertainty in predicting thermal noise is in understanding the coatings themselves. Thermoelastic and photothermal noise are expected to depend on the coating's thermal expansion coefficient, thermal conductivity, and Young's modulus, and recent research into optical materials suggests that the thin films layers in the coatings may have physical properties quite different from those of bulk materials. For instance, the thermal expansion coefficient of stressed, sub-micron vapor deposited SiO_2 films has been observed in the range of 0.6 to $4 \times 10^{-6}/\text{K}$ [5, 20, 30, 127], with elastic moduli from 40 - 60 GPa [68, 30], whereas bulk SiO_2 has a thermal expansion coefficient of $0.5 \times 10^{-6}/\text{K}$ and an elastic modulus of 73 GPa [35]. The picture is murkier for Ta_2O_5 , for which thin film thermal expansion coefficients of 3.6×10^{-6} [118] and -4.4×10^{-5} [66] have been observed. Recently, a bending-beam experiment measured the thermal expansion coefficient for Ta_2O_5 to be $5(\pm 2) \times 10^{-6}$ [25] in a LIGO silica/tantala multilayer coating.

The high thermal expansion of these materials could make them detrimental to test mass thermal noise, but switching to other materials is not likely to improve the situation. For Advanced LIGO [57], other coating materials have been considered [26, 108], such as Al_2O_3 (sapphire) and TiO_2 . Sapphire, which has a crystalline bulk form, is believed to be amorphous as a thin film [80, 81], with a thermal conductivity that decreases with the film thickness [69]. While bulk sapphire has a thermal conductivity of 40 W/m-K [39], it has been observed to be only 3.3 W/m-K in a $2 \times 10^{-7}\text{m}$ Al_2O_3 film [69]. The thermal expansion coefficient of TiO_2 thin films has been measured to be $50 \times 10^{-6}/\text{K}$ [56], several times higher than in bulk samples [42].

This chapter enumerates the thermal noise effects that are expected to affect LIGO mirrors. Representative values of material properties are listed in Table 2.3. Calculations use SI units, unless explicitly noted. Symbols used in this section are listed below.

- r_0 laser spot radius ($1/e$ of central power), meters

- λ laser wavelength, 1.064×10^{-6} meters
- $f = \omega/2\pi$ measurement frequency, Hz
- ρC_v = density \times heat capacity at constant volume, J/m^3
- κ thermal conductivity, W/mK
- σ Poisson's ratio, dimensionless
- α thermal expansion coefficient, $1/K$
- n index of refraction, dimensionless
- d coating thickness, usually $\sim 5 \times 10^{-6}m$
- $\beta = dn/dT$ temperature dependence of n , $1/K$
- ϕ loss angle, dimensionless
- r_t thermal diffusion length, $(\kappa/2\pi\rho C_v f)^{1/2}$
- E Elastic modulus (stress / strain), N/m^2
- P_{abs} power absorbed by a mirror, W
- k_B Boltzmann's constant, $1.39 \times 10^{-23} J/K$
- T temperature, generally $300K$

2.2 Background

2.2.1 Spectral densities

Random noise processes are described in terms of spectral densities [19]. The “one-sided” spectral density (defined for positive frequencies) of a random function $y(t)$ with mean value \bar{y} is the limit of the square of the Fourier transform, defined by the equation

$$S_y(f) = \lim_{T \rightarrow \infty} \frac{2}{T} \left| \int_{-T/2}^{T/2} [y(t) - \bar{y}] e^{i2\pi ft} dt \right|^2 \quad (2.1)$$

The variance of y is the integral of $S_y(f)$ over positive frequencies.

$$\langle (y - \bar{y})^2 \rangle = \int_0^\infty S_y(f) df \quad (2.2)$$

The spectrum of the root-mean-square of the noise in y is $\sqrt{S_y(f)}$. A spectral density S_y has units of y^2 per Hz. To calculate $\langle (y - \bar{y})^2 \rangle$ in an observation, multiply S_y by the bandwidth of the measurement. To convert from a test mirror displacement spectral density to a LIGO interferometer strain, multiply by the factor $1/L^2$, where L is the length of the arm cavity.

2.2.2 Thermal length scales

All the thermal effects we will be considering depend on heat flow, so it's useful to define the thermal diffusion length $r_t = \sqrt{\kappa/\rho C_p 2\pi f}$ and its corresponding characteristic frequency $f_c = \frac{\kappa}{2\pi x^2 \rho C_p}$, where x is the characteristic length scale being measured, usually the spot radius r_0 .

In a coating of thickness d made of two materials, where each layer is much thicker than the phonon mean free path, the effective thermal conductivity κ_e in the direction normal to the surface is dominated by the less conductive material [31].

$$\frac{d}{\kappa_e} \approx \frac{d_1}{\kappa_1} + \frac{d_2}{\kappa_2} \quad (2.3)$$

where κ_1 and κ_2 are the bulk conductivities. For a slab¹ of SiO₂/TiO₂, this would predict $\kappa_e \sim 2$ W/m-K. This puts the coating thermal diffusion length at around 100 microns at 100 Hz.

2.3 Intrinsic noise

Intrinsic thermal noise sources can be derived from the fluctuation-dissipation theorem when the dissipation mechanism is known. In cases where the dissipation mechanism is not obvious, noise effects can be identified by looking for material properties which depend on temperature, like thermal expansion and dn/dT . An introduction to the fluctuation-dissipation theorem is presented below, followed by a catalog of noise mechanisms.

¹Al₂O₃ can be used instead of SiO₂, but sub-micron Al₂O₃ films have low thermal conductivity like SiO₂ [69].

2.3.1 The fluctuation-dissipation theorem

The fluctuation-dissipation theorem (Eq. 2.4) shows that thermodynamic noise is a consequence of any irreversible dissipation process [28, 29]. Given a generalized resistance, R to a driving force F , there will arise at non-zero temperatures a spontaneous fluctuation in F . Force and resistance are defined such that the resistance R is the real part of the impedance Z for some oscillatory force $F(f)$ that drives a coordinate q .

$$\langle F^2 \rangle = 4k_B T \int R(f) df = \int S_F(f) df \quad (2.4)$$

$$(2.5)$$

The relationship between F and R is defined by an impedance Z , defined by

$$F(f) = Z(f) \dot{q}(f) \quad (2.6)$$

$$F(f) = Z(f) i2\pi f q(f) \quad (2.7)$$

$$R(f) = \Re[Z(f)] \quad (2.8)$$

Knowing $S_F(f)$, we can find the spectral density of fluctuations in q .

$$\begin{aligned} S_q(f) &= \frac{S_F(f)}{Z^2 4\pi^2 f^2} \\ &= \frac{k_B T}{\pi^2 f^2} \frac{R}{|Z|^2} \\ &= \frac{k_B T}{\pi^2 f^2} \Re\left[\frac{1}{Z}\right] \end{aligned} \quad (2.9)$$

To obtain $\Re(1/Z)$, we can compute the average power converted to heat (the dissipation, P_d) due to a sinusoidal forcing function $F = F_0 \sin 2\pi ft$. This formula (Eq. 2.10) is provided by Levin [82] for the case where F and q are both distributed over the same Gaussian spot on the surface of the mirror, which leads directly to a solution

$$\Re\left[\frac{1}{Z(f)}\right] = \frac{2 \times \text{Dissipated power}}{F_0^2} \quad (2.10)$$

The dissipated power differs for each noise source, and is often frequency dependent. The key to understanding each source of thermal noise is identifying how an imaginary applied force (mechanical, electrical, magnetic, etc.) is converted into heat.

2.3.2 Bulk internal friction

Internal friction in solids was identified by Kimball and Li [73, 74], who described it as a phase shift between stress and strain. For historical reasons, this is what people commonly mean when they refer to “thermal” and “Brownian motion” noise. The Brownian motion interpretation comes from thinking of the mirror’s recoil from its internal phonons, while the internal friction interpretation is a direct application of the fluctuation-dissipation theorem.

The figure of merit for internal friction in a material is its loss angle, ϕ , defined as the (small) phase of the complex elastic modulus $E = E_0(1 + i\phi)$, where the loss angle and quality factor Q are related by $Q = 1/\phi$. One model for internal friction, first identified by identified by Saulson [110] as a source of noise for LIGO, is “structural damping,” in which ϕ is independent of frequency. The assumption that $\phi(f)$ is constant may not be true (see [24, 13]) and there is evidence [124] to suggest that the loss angle of bulk materials increases with frequency.

There are two ways to calculate the noise from internal friction. In the Brownian motion model, each normal mode [111] has energy $k_B T$, and causes surface motion proportional to $f^{-1/2}$ below its resonant frequency. One can calculate the low-frequency thermal noise by numerically summing over the normal modes of the mirror [54].

The structural damping interpretation is easier to use. This was introduced by Levin [82] and identifies a force $F = F_0 \sin 2\pi ft$ as a periodic pressure on the mirror surface with a Gaussian spatial distribution matching that of the laser beam reflecting from the mirror. A method for extending Levin’s half-space model to finite-sized mirrors was introduced by Bondu, Hello, and Vinet [45], and revised and extended by Liu and Thorne [88]. Using a Green’s function technique, Nakagawa *et al.* [91, 92] derive the total interferometer thermal noise, accounting for multiple reflections in a Fabry-Perot interferometer or in a delay line interferometer. For a single mirror whose dimensions are much larger than the spot size, Levin derives the dissipated power.

$$\frac{\text{Dissipated power}}{F_0^2} \propto \frac{f\phi(f)(1-\sigma^2)}{E_0 r_0} \quad (2.11)$$

where E_0 is the real part of the elastic modulus. The spectral density of fluctuations given by Bondu, Hello, and Vinet is

$$S_{SD}^{bulk}(f) = \frac{4k_B T}{(2\pi)^{3/2} f} \frac{\phi(f)(1-\sigma^2)}{E_0 r_0} \quad (2.12)$$

Given this, the only difficulty in predicting structural damping noise is to identify the loss angle. Measurements in LIGO-like samples show that the Q of a low-loss fused silica mirror can vary by several orders of magnitude among resonant modes [27]. As Levin pointed out [82], this suggests that surface friction makes large contributions to mirror losses, but, depending on where they appear on the mirror, surface losses might not affect the bulk thermal noise. For instance, suspension point friction on the side of a mirror barrel might not figure highly in the vibrational modes that move the center of the mirror face.

It is generally believed that the loss angle that matters is that of the bulk material, and Numata's [94] data on BK7 ($Q \sim 4000$) mirrors support this. In high-Q mirrors, the TNI (Ch. 4) shows that this could still be true, even with friction from wire supports and magnets. There are other noise sources associated with the test mass suspension [63], including viscous gas damping, and pendulum thermal noise.

2.3.3 Coating structural damping

The potential for structural damping in the coating to produce noise was introduced by Levin [82] and a theory developed by Nakagawa *et al.* [93] and Harry *et al.* [60]. Allowing for anisotropy in the coating, they characterize the coating structural damping by the loss angles of the mirror layers parallel and perpendicular to the mirror surface, ϕ_{\parallel} and ϕ_{\perp} . Measurements made by Harry *et al.* [60] and Penn *et al.* [101] found ϕ_{\parallel} to be around 1×10^{-4} for Ta₂O₅/SiO₂ mirror coatings on superpolished fused silica and sapphire substrates, and measurements by Crooks *et al.* found coating loss angles of $\sim 6 \times 10^{-5}$ for Ta₂O₅/Al₂O₃ mirror coatings on fused silica. They estimate the thermal noise contribution as

$$S_{SD}^{layer}(f) = \frac{2}{\pi^2} \frac{k_B T d}{E_{bulk} r_0^2 f} \left(\frac{E_{coating}}{E_{bulk}} \phi_{\parallel} + \frac{E_{bulk}}{E_{coating}} \phi_{\perp} \right) \quad (2.13)$$

This model is designed to explain noise on fused silica substrates and assumes the losses come from the bulk materials themselves, not from friction at boundaries. Values for ϕ_{\perp} are unknown and are assumed to be equal to ϕ_{\parallel} .

2.3.4 Bulk thermoelastic noise

A system in equilibrium with a heat reservoir may have fluctuations in its energy E , according to the equation [104]

$$\begin{aligned} \langle (\Delta E)^2 \rangle &= \frac{\partial^2 \ln Z}{\partial \beta_t^2} \\ Z &= \sum_n e^{\beta_t E_n} \end{aligned} \quad (2.14)$$

where $\beta_t = 1/k_B T$ and Z is the partition function, summed over all possible states of the system. Since the mean energy can be written as $\bar{E} = -\frac{\partial}{\partial \beta_t} \ln Z$, Eq. 2.14 can be written as

$$\langle (\Delta E)^2 \rangle = k_B T^2 \left(\frac{\partial \bar{E}}{\partial T} \right)_V \quad (2.15)$$

Temperature fluctuations are a convenient way to think about these energy fluctuations, by taking $\Delta E = C_v V \Delta T$. According to Kittel [76], this is not strictly correct, since temperature, by definition, does not fluctuate. Nevertheless, it is a powerful tool for understanding fluctuations in temperature-dependent parameters. For this purpose, one can use an effective temperature fluctuation for a region of volume V [78]

$$\langle (\Delta T)^2 \rangle = \frac{k_B T^2}{\rho C_v V} \quad (2.16)$$

For instance, if the mirror substrate has a non-zero thermal expansion coefficient, these fluctuations will move its surface. Another way of thinking about this system is thermoelastic damping. Braginsky, Gorodetsky, and Vyatchanin (BGV99) [22] showed that a periodic pressure at the sur-

face of a material with non-zero thermal expansion leads to heat flux and energy dissipation. The fluctuation-dissipation theorem then relates the lost energy to the surface displacement. For laser spots significantly smaller than the mirror dimensions, the expected length noise is [32]

$$S_{\alpha,T}^{bulk}(f) = \frac{8}{\sqrt{2\pi}} \frac{\alpha^2(1+\sigma)^2 k_B T^2 r_0}{\kappa} \times \int_0^\infty du \int_{-\infty}^\infty dv \frac{\sqrt{2} u^3 e^{-u^2/2}}{\sqrt{\pi}(u^2+v^2)((u^2+v^2)^2+(f/f_c)^2)} \quad (2.17)$$

where $f_c = \frac{\kappa}{2\pi r_0^2 \rho C_p}$. In the limit of high frequencies or large spot sizes ($f \gg f_c$), Eq. 2.17 approaches the BGV99 prediction.

$$S_{\alpha,T}^{bulk}(f) = \frac{8}{\sqrt{2\pi}} \frac{\alpha^2(1+\sigma)^2 \kappa k_B T^2}{(2\pi \rho C_V)^2 r_0^3 f^2} \quad (2.18)$$

Where the spot size is comparable to the mirror dimensions (but still larger than the thermal diffusion length) and $f \gg f_c$, analytic approximations by Liu and Thorne [88] predict differences from the BGV99 formula on the order of 10-20%. This noise has been measured by Kenji Numata [94] in CaF₂ mirrors and agrees well with theory.

2.3.5 Coating thermoelastic noise

Thermodynamic fluctuations are local and depend on the volume of the affected region. Measured as an average over the entire test mass, the temperature is better defined than it is for a small region, say the volume of the dielectric mirror coating itself. These short-range temperature fluctuations are expected to be significant sources of noise for LIGO.

High-quality dielectric mirrors are made from alternating quarter-wave layers of high- and low-index materials. Preferred high-index compounds are Ta₂O₅ and TiO₂ which, as thin films, may have high thermal expansion and dn/dT coefficients [66, 56]. Preferred low-index compounds are SiO₂ and Al₂O₃.

To consider noise from the mirror coating, only the temperature changes near the surface of the mirror matter. The thermal diffusion length sets the length scale of regions with independently fluctuating temperatures, and a large laser spot will average the fluctuations of many of these regions.

If the coating has good thermal coupling to the substrate, the substrate and the coating can be expected to have the same temperature fluctuations. In this case, the coating may be thought of as a continuation of the substrate, just with a different thermal expansion. Braginsky and Vyatchanin

(BV03) [26] have estimated the spectral density of the surface fluctuations as observed by a Gaussian beam. For a uniform coating with thickness l , the temperature fluctuations are

$$S_{\Delta T}^{layer}(f) = \frac{\sqrt{2}k_B T^2}{\pi r_0^2 \sqrt{\kappa \rho C_v} 2\pi f} \quad (2.19)$$

and the thermal expansion averaged over a Gaussian beam is [26]

$$S_{\alpha, T}^{layer}(f) = \frac{4\sqrt{2} \alpha_{eff}^2 (1 + \sigma)^2 d^2 k_B T^2}{\pi r_0^2 \sqrt{\kappa \rho C_V} 2\pi f} \quad (2.20)$$

where d is the total layer thickness and α_{eff} is the coefficient of thermal expansion for the coating in the direction normal to the surface. A real dielectric mirror has upwards of 40 layers, and there could be a ‘‘bimetallic’’ stress effect to cause more surface displacement. By balancing the horizontal stresses, BV03 propose that the multilayer coating be treated by an effective thermal expansion coefficient.

$$\alpha_{eff} = \frac{\alpha_1 d_1}{d_1 + d_2} \frac{E_1(1 - 2\sigma)}{E(1 - 2\sigma_1)} + \frac{\alpha_2 d_2}{d_1 + d_2} \frac{E_2(1 - 2\sigma)}{E(1 - 2\sigma_2)} - \alpha_{bulk} \quad (2.21)$$

where d_1 and d_2 are individual layer thicknesses and the E 's and σ 's are the various elastic moduli and Poisson's ratios of the coating materials. Ignoring the Young's modulus and Poisson's ratio and assuming the lower values from Table 2.1, α_{eff} for a Ta₂O₅ / SiO₂ coating is $1.8 \times 10^{-6}/\text{K}$.

If the coating is much less stiff than the substrate, one might expect the coating to react as if it were compressed or stretched in the transverse plane. Then, simply by applying the definition of Poisson's ratio, the effective thermal expansion coefficient could take the form (see Eq. 7.12 in [78])

$$\alpha_{eff} = \frac{\alpha_1 d_1 (1 + 2\sigma_1)}{d_1 + d_2} + \frac{\alpha_2 d_2 (1 + 2\sigma_2)}{d_1 + d_2} - \alpha_{bulk} \quad (2.22)$$

Rowan and Fejer [108] present a different theory to account for differences in thermal diffusivity between the coating and substrate. Their estimate of the coating thermal expansion is

$$\begin{aligned}
S_{\alpha,T}^{layer*} &= \frac{4k_B T^2}{\pi^2 f r_0^2} \frac{\rho_{layer} C_{layer}}{\rho_{bulk}^2 C_{bulk}^2} \alpha_{eff}^2 d(1+\sigma)^2 g(\omega) \\
\alpha_{eff} &= \frac{\alpha_{layer} \rho_{layer} C_{bulk}}{2\rho_{bulk} C_{layer} (1-\sigma_{bulk})} \left(\frac{1+\sigma_{layer}}{1+\sigma_{bulk}} + (1-2\sigma_{bulk}) \frac{E_{layer}}{E_{bulk}} \right) - \alpha_{bulk} \\
g(\omega) &= \Im \left[\frac{-\sinh(\sqrt{i\omega\tau})}{\sqrt{i\omega\tau} \left(\cosh(\sqrt{i\omega\tau}) + \sqrt{\frac{\kappa_{layer} \rho_{layer} C_{layer}}{\kappa_{bulk} \rho_{bulk} C_{bulk}}} \sinh(\sqrt{i\omega\tau}) \right)} \right]
\end{aligned} \tag{2.23}$$

where $\tau = d^2 \rho C / \kappa$ for the coating. At high frequencies, $g(\omega)$ has a $f^{-1/2}$ dependence, and at $\omega = 1/\tau$, $g(\omega)$ is 0.26. Assuming that the material properties for the coating layers and the bulk are the same and taking the high-frequency limit, Eq. 2.23 differs from Eq. eq2:layertd by a factor of $1/\omega\tau$ (neglecting factors of order unity).

2.3.6 Coating thermorefractive noise

Fluctuations in the refractive index of the mirror coating layers also cause changes in the phase of the light they reflect. The formula for dn/dT noise follows directly from Eq. 2.20. For a dielectric mirror made from two materials with indices of refraction n_1 and n_2 and $\beta_i = dn_i/dT$ the length-equivalent noise was derived by BGV00 [23].

$$\begin{aligned}
S_{\beta,T}^{layer}(f) &= \beta_{eff}^2 \lambda^2 \frac{\sqrt{2} k_B T^2}{\pi r_0^2 \sqrt{2\pi} \rho C_v \kappa f} \\
\beta_{eff} &= \frac{n_2 n_1 (\beta_1 + \beta_2)}{4(n_1^2 - n_2^2)}
\end{aligned} \tag{2.24}$$

The loss mechanism behind dn/dT noise may be electrocaloric dissipation [123], so it is possible that S_{β}^{layer} and S_{α}^{layer} are at least partially uncorrelated, as both the lattice expansion and the temperature dependence of optical resonances affect dn/dT in glasses [49].

2.3.7 Bulk thermorefractive noise

Most GW Michelson interferometer designs involve passing light through at least one thick optic, the beamsplitter. As the index of refraction of the beamsplitter substrate depends on temperature, temperature fluctuations will impart phase fluctuations in the interferometer.

$$S_{\Delta\phi}^{\beta}(f) = \left(\frac{\beta l}{\lambda}\right)^2 \frac{\sqrt{2}k_B T^2}{\pi r_0^2 \sqrt{\rho C_v} 2\pi f} \quad (2.25)$$

where l is the mirror thickness. This could be a limiting noise source in an interferometer with high optical gain in the Michelson cavity (such as in GEO600[58]), but it is believed to not be a major problem for LIGO [123].

2.4 Photon-driven noise

Driven temperature fluctuations arise from the test mass being heated, such as by absorption of photons from a laser beam with intensity fluctuations. Photon-drive noise depends, of course, on the absorptivity of the mirror, which can depend strongly on the coating manufacturing process.

2.4.1 Bulk expansion

When a material absorbs light, it converts it to heat and thermal expansion ensues. This is commonly known as the “photothermal” effect, although a more specific name would be “photoelastic,” to distinguish it from the photorefractive (dn/dT) effect.

The photothermal effect is used (particularly in the semiconductor industry) to measure thermal properties of materials [67, 95, 9]. A common configuration is the modulated photothermal deflection experiment [83, 10], in which a “pump” laser beam, chopped into a square wave, strikes a sample at normal incidence, while a “probe” beam strikes the sample at a glancing angle. The pump beam is partially absorbed by the sample, raising a blister, which is observed by deflection of the probe beam.

There is less work on transparent materials like the glasses and crystals used for making mirror substrates. An interferometer is a natural tool to study these, where the photothermal distance changes may be less than a nanometer. De Rosa et al. [106] have reported observation of the photothermal effect in low-absorption (0.5 ppm) dielectric mirrors made by Research Electro-Optics (REO²) [107]. Their study was done at low frequencies (10 mHz - 200 Hz), using two Fabry-Perot interferometers with fused silica mirrors, and appears to agree well with theory. Measurements of this effect in several types of mirror in a higher frequency band are presented in the following chapter.

²REO claims absorption of 10 ppm or less, which is sometimes used as a conservative estimate for LIGO. LIGO’s specified limit on increase in optical absorption is 2 ppm/year [84]

For intensity fluctuations in the light absorbed by the mirror given by S_{abs} , the photothermal length change measured by an interferometer is [32]

$$S_{\alpha,P}(f) = \frac{2\alpha^2(1+\sigma)^2 S_{abs}}{\pi^2 \kappa^2} \times \left[\frac{1}{\pi} \int_0^\infty du \int_{-\infty}^\infty dv \left[\frac{u^2 e^{-u^2/2}}{(u^2+v^2)(u^2+v^2+if/f_c)} \right] \right]^2 \quad (2.26)$$

At high frequencies or large laser spots ($f \gg f_c$), this function simplifies to [22]

$$S_{\alpha,P}^{bulk}(f) = \frac{\alpha^2(1+\sigma)^2}{2\pi^2} \frac{S_{abs}(f)}{(\rho C_V \pi r_0^2)^2 f^2} \quad (2.27)$$

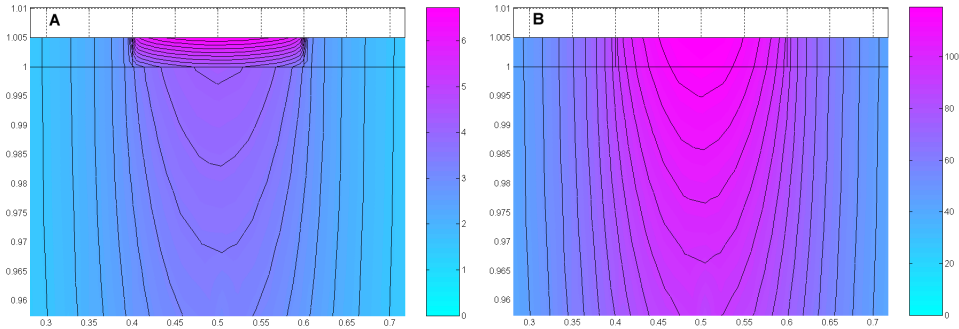
The shot noise limit S_{abs} depends on the average power absorbed by the mirror \bar{P}_{abs} and the photon energy $h\nu = hc/\lambda$. The average rate of photon absorption is $N = \bar{P}_{abs}/h\nu$, and, from Poisson statistics, the fluctuation in N is \sqrt{N} . Thus, the fluctuation in the absorbed power is $\sqrt{N}h\nu = \sqrt{\bar{P}_{abs}h\nu}$. The square of this gives the spectral density of the fluctuations, or simply $S_{abs} = \bar{P}_{abs}h\nu$.

2.4.2 Coating expansion

We would like to estimate how photon heating on a Gaussian spot at the mirror surface affects the temperature distribution $u(\vec{r}, t)$ throughout the mirror. At high frequencies, where r_t is less than the coating thickness, the coating expansion should behave like bulk thermal expansion, much like the situation described in §2.4.1. In the other limit, at low frequencies, the coating and the substrate should be at the same temperature, so that the coating's average length change just scales with substrate temperature, $\Delta x = \alpha_{layer} d \Delta T$. In between is a regime where the average coating and substrate temperatures may be different, and new models are needed. A calculation of the coating's thermal response in this range depends on how the thermal diffusivity $a^2 = \kappa/\rho C$ of the coating compares to that of the substrate.

Consider a two-dimensional model of a 5 micron $\text{SiO}_2/\text{TiO}_2$ coating on top of a sapphire or fused silica substrate, with heat applied steadily at a spot on the coating's surface and allowed to diffuse into the bulk. The heat flow patterns simulated with Matlab [114], shown in Fig. 2.1, are quite different for these two scenarios. In the sapphire case, heat diffuses slowly through the coating, and quickly through the substrate. In the coating, the heat flow does not have time to diffuse to the

Figure 2.1: Heat flow simulation created with Matlab and PDETool. A constant unit heat flow is applied to a 200 micron wide spot on at a mirror surface. Lines show contours of constant temperature. The scale shows the temperature in arbitrary units. The coating is 5 microns thick, an average of SiO_2 and TiO_2 , with $\rho = 3200 \text{ kg/m}^3$ - K, $C_v = 700 \text{ J/kg-K}$, $\kappa = 2 \text{ W/m-K}$ (from Eq. 2.3). The mirror coating away from the heated spot does not conduct heat, and the bottom and sides, far away, have fixed $T=0$. A: Sapphire substrate. B: Fused silica substrate.



side, so that the isotherms in the coating resemble plane waves until they reach the sapphire. On a fused silica substrate, heat sees the coating and substrate as nearly equivalent materials which diffuse heat at the same rate, so the pattern of isotherms in the coating resemble those in the substrate.

To extrapolate to real mirrors, I choose to model heat flow in the coating separately for these cases. On sapphire (‘high-conductivity’) substrates, I estimate the coating thermal expansion by treating the heat flow in the coating as purely one-dimensional, and solve for the average temperature of the coating. On fused silica (‘low-conductivity’) substrates, I use a different method, similar to that introduced in BGV00 [23]. With this technique, I solve for the heat flow in a uniform half-space, and then compute the average temperature for a layer near the surface with a frequency-dependent scale height determined by r_t .

2.4.2.1 High-conductivity substrates

In this model, heat flows much faster in the substrate than in the coating. Therefore heat flow in the coating is essentially one-dimensional, normal to the surface, and because the heat is transmitted directly through the coating, the substrate responds the same as it would without the coating. What then, does one-dimensional heat flow look like? The heat conduction equation is [46]

$$\frac{\partial u(z, t)}{\partial t} - \frac{\kappa}{\rho C_v} \frac{\partial^2 u(z, t)}{\partial z^2} = 0 \quad (2.28)$$

where $u(z)$ is the temperature at depth z and time t . This equation is separable, and has a solution of the form $u(z, t) = u(z)e^{-i\omega t}$. Substitution back into Eq. 2.28 gives

$$i\omega u(z) - \frac{\kappa}{\rho C_v} \frac{\partial^2 u(z)}{\partial z^2} = 0 \quad (2.29)$$

A trial solution of the form $u(z) = u_0 e^{bz}$ determines b .

$$i\omega - \frac{\kappa}{\rho C_v} b^2 = 0 \quad (2.30)$$

$$b = \pm \sqrt{\frac{i\omega \rho C_v}{\kappa}} \quad (2.31)$$

$$u(z, t) \propto e^{i\omega t} \left[c_1 e^{z \sqrt{\frac{i\omega \rho C_v}{\kappa}}} + c_2 e^{-z \sqrt{\frac{i\omega \rho C_v}{\kappa}}} \right] \quad (2.32)$$

where c_1 and c_2 are constants chosen to match the boundary conditions. Since $u(z, t)$ must vanish as $z \rightarrow \infty$, we know that $c_1 = 0$. This means that if the surface temperature is given by $u(z = 0, t) = T_0 e^{-i\omega t}$, then the temperature deeper inside the material is

$$u(z = d, t) = T_0 e^{i\omega t} e^{-d \sqrt{\frac{i\omega \rho C_v}{\kappa}}}. \quad (2.33)$$

For photon heating, the boundary conditions specify the derivative of the temperature at the surface. This can be written as [46]

$$\frac{\partial u(z, t)}{\partial t} - \frac{\kappa}{\rho C_v} \frac{\partial^2 u(z, t)}{\partial z^2} = \sum_n \frac{\dot{Q}_n}{\rho C_v} \delta(z - z_n) \quad (2.34)$$

where the amount of heat added is \dot{Q} at location z_n . For the coating on top of a substrate, heat is added by the laser beam at the $z = 0$ surface. Since the substrate has a much greater thermal

diffusivity than the coating, I make the simplifying assumption that the heat flux at the $z = d$ is fully removed from the coating into the substrate. Following [22], and letting $a^2 = \kappa/\rho C_v$, an estimate of the heat flow equation for the coating can be written as

$$\left(\frac{d}{dt} - a^2 \frac{\partial^2}{\partial z^2}\right) u(\vec{r}, t) = \frac{2P(\omega)}{\rho C_v} \left(\delta(z) - \delta(z-d) e^{-d\sqrt{i\omega/a^2}} \right) \quad (2.35)$$

$$\begin{aligned} 0 \leq z \leq d \\ P(\omega) &= \frac{P_0 e^{i\omega t} e^{-(x^2+y^2)/r_0^2}}{\pi r_0^2} \end{aligned} \quad (2.36)$$

In Eq. 2.35, the first δ term accounts for heat added by the laser, and the second δ term accounts for heat flow into the substrate, with a proportionality term from Eq. 2.33. To solve this, we take the Fourier transforms $t \rightarrow \omega$ and $z \rightarrow k_z$

$$\begin{aligned} (i\omega + a^2 k_z^2) \tilde{u}(k_z, \omega) &= \frac{2\tilde{P}(\omega)}{\rho C_v} \int_0^\infty \left(\delta(z) - \delta(z-d) e^{-d\sqrt{i\omega/a^2}} \right) e^{ik_z z} dz \\ &= \frac{2\tilde{P}(\omega)}{\rho C_v} \left(1 - e^{ik_z d - d\sqrt{i\omega/a^2}} \right) \end{aligned} \quad (2.37)$$

Next, invert the spatial transform to solve for the temperature throughout the coating.

$$u(z, \omega) = \frac{2\tilde{P}(\omega)}{\rho C_v} \int_{-\infty}^\infty \frac{dk_z}{2\pi} \frac{1 - e^{ik_z d - d\sqrt{i\omega/a^2}}}{i\omega + a^2 k^2} e^{-ik_z z} \quad (2.38)$$

Then, average $\bar{u}(\omega)$ over the thickness of the coating by integrating z from 0 to d to calculate the average temperature in the coating.

$$\bar{u}(\omega) = \frac{2\tilde{P}(\omega)}{\rho C_v} \int_0^d \frac{dz}{d} \int_{-\infty}^\infty \frac{dk_z}{2\pi} \frac{1 - e^{ik_z d - d\sqrt{i\omega/a^2}}}{i\omega + a^2 k^2} e^{-ik_z z} \quad (2.39)$$

Mathematica [125] can evaluate this integral¹, which simplifies to

¹Use $\int_{-\infty}^\infty \frac{1 - e^{ik_z d + b\sqrt{id^2\omega/a^2}}}{i\omega + a^2 k^2} e^{-ik_z z} dk$ and let $b \rightarrow -1$.

$$\bar{u}(\omega) = \frac{2\tilde{P}(\omega)}{\rho C_v} \frac{1}{d} \frac{\left(1 - e^{-d\sqrt{i\omega/a^2}}\right)^2}{i\omega} \quad (2.40)$$

The average displacement the interferometer will see is thus

$$\bar{X}(\omega) = \alpha_{layer} d \int_{-\infty}^{\infty} \int_{-\infty}^{\infty} dx dy \frac{\bar{u}(\omega) e^{-(x^2+y^2)/r_0^2}}{\pi r_0^2} \quad (2.41)$$

$$= \frac{\alpha_{layer} \tilde{P}(\omega)}{\rho C_v \pi r_0^2 i\omega} \left(1 - e^{-d\sqrt{i\omega/a^2}}\right)^2 \quad (2.42)$$

where $\tilde{P}(\omega)$ is the Fourier component of the fluctuations in the light heating the sample. This function approaches zero at low frequencies and Eq. 2.27 at high frequency, within factors of unity. To get the spectral density, we square this and replace $\tilde{P}(\omega)$ with the shot noise spectral density (see §2.4.1).

$$S_{\alpha,P}^{layer}(f) \approx \frac{\alpha_{layer}^2 S_{abs}(f)}{(\rho C_v 2\pi^2 r_0^2 f)^2} \left(1 - e^{-d\sqrt{i2\pi f/a^2}}\right)^4 \quad (2.43)$$

A simple estimate of the layer expansion is

$$\alpha_{layer} = \frac{\alpha_1 d_1}{d_1 + d_2} + \frac{\alpha_2 d_2}{d_1 + d_2} \quad (2.44)$$

2.4.2.2 Low-conductivity substrates

At high frequencies, where the thermal diffusion length is smaller than the coating thickness, we would expect the coating's photothermal response to act just like a bulk material, only with higher thermal expansion. In the limit of very low frequencies, the whole mirror is essentially isothermal, and the photothermal response should approach a constant value, with the thermal expansion dominated by the substrate. In between, there has to be a transition range, where thermal fluctuations in the coating are transmitted to and diluted by the substrate, but the fluctuations are larger near the surface than they are in the interior of the mirror.

Following BV03, a simple estimate for the temperature of the coating is to assume that the

average heat deposited at the surface is instantly distributed over a volume $V = r_0^2 r_t$ [26, 97]. From the per-cycle change in energy of this volume, $\Delta E \approx P_{abs}/f$, we get the spectrum of its temperature fluctuations.

$$\Delta T_{surface}(f) \approx \frac{\Delta E}{\rho C_v V}$$

Replacing ΔE with P_{abs}/f and V with $\pi r_0^2 r_t$, we get

$$\Delta T_{surface}(f) \approx \frac{P_{abs}(f)}{f \rho C_v r_0^2 r_t}$$

Since $r_t = \sqrt{\kappa/\rho C_v 2\pi f}$, we can write

$$\begin{aligned} \Delta T_{surface}(f) &\approx \frac{P_{abs}(f)}{\pi r_0^2 \sqrt{\rho C_v \kappa} 2\pi f} \\ \bar{X}(f) &= \frac{\alpha_{layer} d P_{abs}(f)}{\pi r_0^2 \sqrt{\rho C_v \kappa} 2\pi f} \end{aligned} \quad (2.45)$$

The spectral density of temperature fluctuations scales with $(\Delta T)^2$, as does the spectral density of the mirror displacement.

$$\begin{aligned} S_{\alpha, P}^{layer*}(f) &= \alpha_{layer}^2 d^2 (\Delta T_{surface}(f))^2 \\ S_{\alpha, P}^{layer*}(f) &= \frac{\alpha_{layer}^2 d^2 S_{abs}(f)}{2\pi^3 r_0^4 \rho C_v \kappa f} \end{aligned} \quad (2.46)$$

where $S_{abs} = P_{abs}^2$. This is intended to demonstrate that, by computing an average temperature near the surface, one finds the spectrum of temperature fluctuations to be proportional to $1/\sqrt{f}$. This clearly does not apply for high frequencies where the coating is not in thermal equilibrium with the substrate, or for low frequencies where the temperature should approach a constant value. A more sophisticated treatment of this problem is derived in the appendix (see §5.1), which arrives at an equation that differs from Eq. 2.46 by a factor of 2.

Eq. 2.46 is proportional to $f^{-1/2}$, while the photothermal response of the substrate scales as

f^{-1} . Comparing this to Eq. 2.27, coating thermal expansion will start to dominate that of the substrate at frequencies above $f_{min} = \frac{\kappa}{\rho C_v d^2} \frac{\alpha_{bulk}^2}{\alpha_{layer}^2}$. Another way of understanding this is that this crossover occurs when $\alpha_{layer} d > \alpha_{bulk} \tau_t$.

2.4.2.3 Photothermal noise summary

The strength of photothermal noise depends on the thermal properties of the substrate and the coating. The literature (see Table 2.1) suggests that the preferred low-index mirror materials, Al_2O_3 and SiO_2 , have low thermal diffusivity, which will dominate the coating's heat conduction. With sapphire and fused silica, the heat flow is expected to be qualitatively different. Fig. 2.1 compares numerical solutions to the heat equation in two dimensions under conditions similar to laser heating. On sapphire, heat flows straight down through the coating under the laser spot. On fused silica, heat diffuses sideways through the coating the same as it does through the substrate.

Shot noise driven photothermal noise is very small, given the low absorption of dielectric mirrors. For the case of LIGO with 800 kW beams, the estimated coating and bulk photothermal noise are plotted in Fig. 2.2.

2.4.3 Coating dn/dT

One would expect length-equivalent photorefractive noise to be like coating thermal expansion noise, substituting αd with $\beta \lambda$. By comparison with Eq. 2.43, we can estimate the photorefractive noise on a fused silica mirror.

$$S_{\beta,P}^{layer}(f) \approx \frac{\beta^2 \lambda^2 S_{abs}(f)}{4\pi^3 r_0^4 \rho C_v \kappa f} \quad (2.47)$$

and for a sapphire mirror,

$$S_{\beta,P}^{layer}(f) \approx \frac{\beta^2 \lambda^2 S_{abs}(f)}{d^2 (2\rho C_v \pi^2 r_0^2 f)^2} \left(1 - e^{-d\sqrt{i2\pi f/a^2}}\right)^4 \quad (2.48)$$

Figure 2.2: Relative coating and bulk photothermal strain noise in two Advanced LIGO arm cavities. The sapphire line plots coating expansion from Eq. 2.43, and the fused silica line shows the bulk expansion from Eq. 2.26. For coating noise, the end test mirrors (with thicker coatings) dominate. For bulk noise, the input test mirrors (with smaller spot size) dominate. For sapphire, the spot size is taken to be 4.2 cm. For fused silica, the ITM (Input Test Mass) and ETM (End Test Mass) spot sizes ($1/e$ of power) are taken to be 2.5 cm and 3.2 cm [71, 12], respectively. The coating absorption is 0.5 ppm, and the thermal expansion is from the lower values in Table 2.1. The sapphire substrate response is higher than fused silica's because of the difference in thermal expansion coefficients. The predictions of the coating noise use the equations derived in this chapter appropriate to the substrate medium.

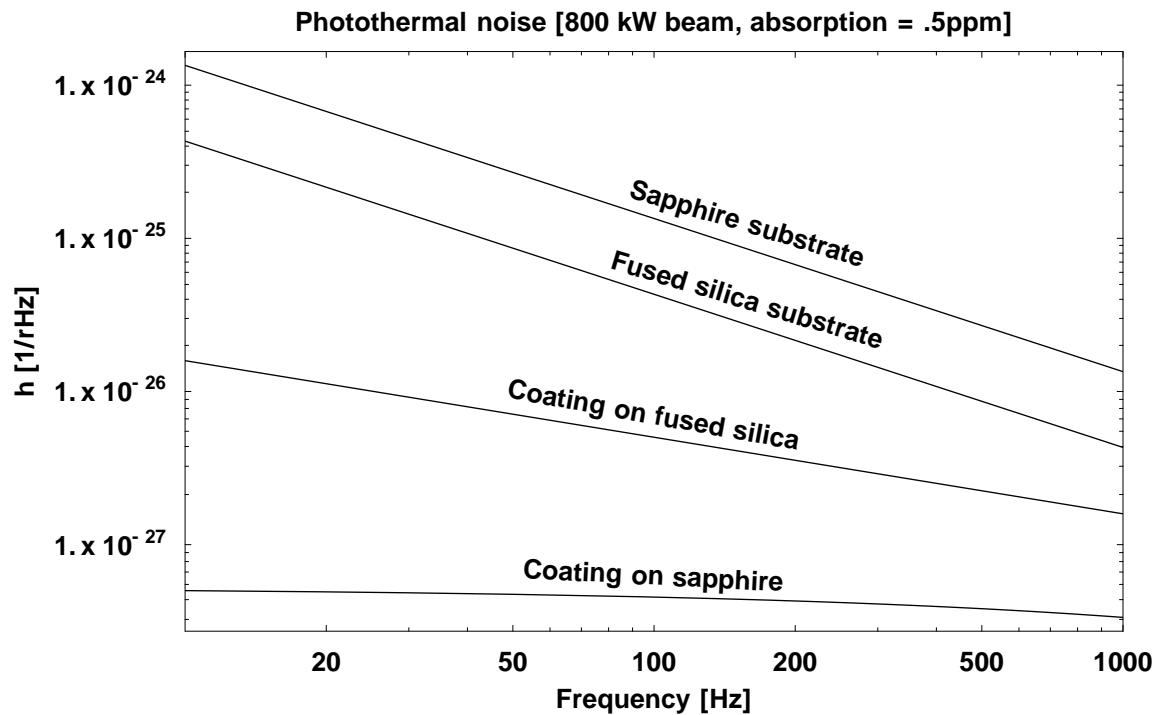
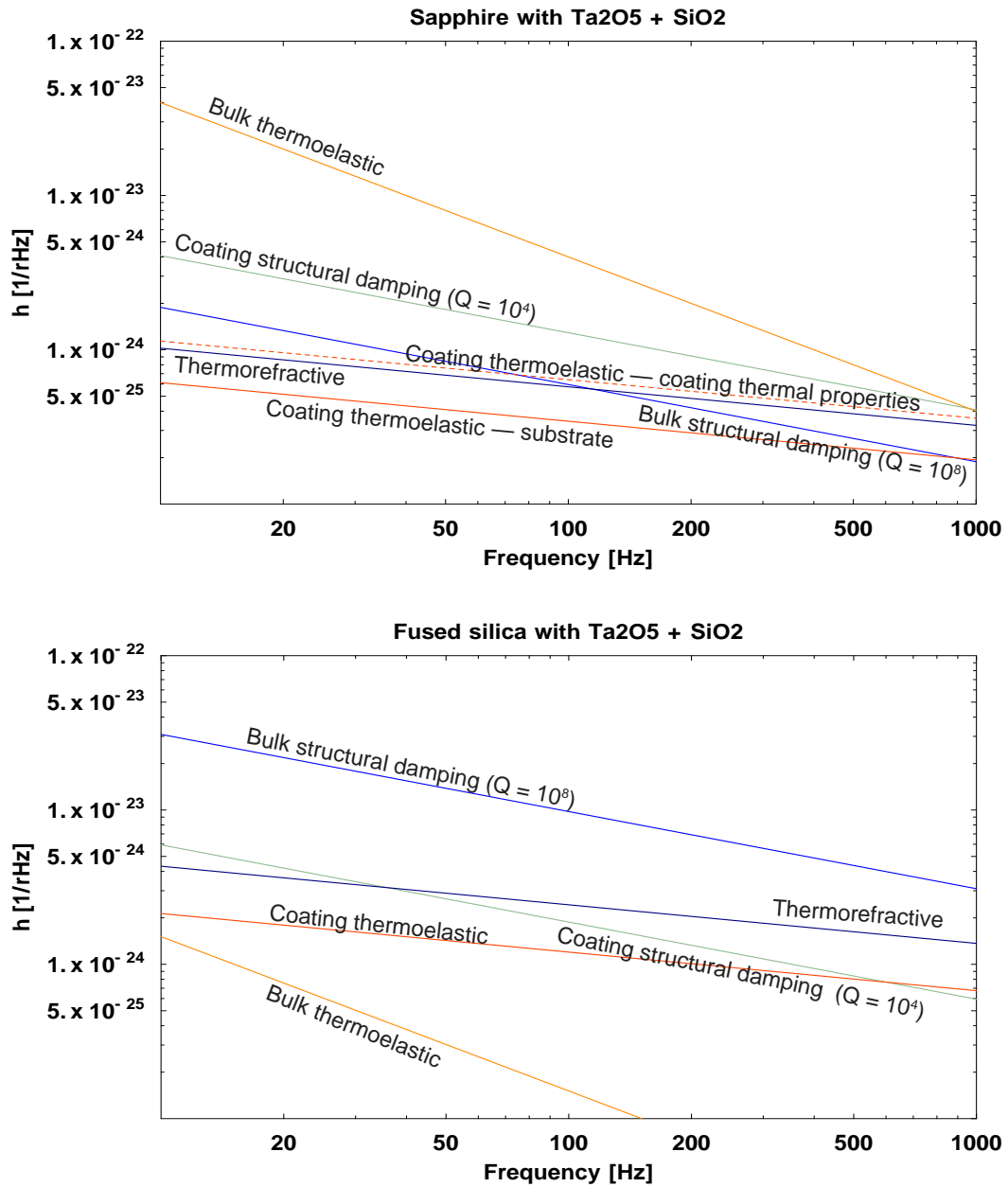


Figure 2.3: Thermal strain noise for LIGO with sapphire and fused silica mirrors. Coating noises are calculated for two ETM mirrors, and bulk noises are calculated for two ITM mirrors. For sapphire mirrors, the spot size is 4.2 cm. For fused silica mirrors, ITM spot size = 2.5 cm, ETM spot size = 3.2 cm. ETM coating = 40 layers, $\alpha_{eff} = 2.4 \times 10^{-6}$.



2.5 Summary

Fig. 2.3 shows thermal noise estimates for LIGO. The dominant thermal noise source is predicted to be coating thermoelastic noise given by BV03 (Eq. 2.20), but the theory for this is based on the assumption that the substrate and the coating are thermally coupled. On a sapphire substrate, the coating's low thermal diffusivity may cause it to be essentially decoupled from the substrate. To predict the noise in this case, Eq. 2.20 is plotted using the coating's thermal properties instead of the substrate's. The lower coating thermal expansion coefficients from Table 2.1 are used for this estimate.

Table 2.1: Coating material properties are highly dependent on the manufacturing process. Representative values from the literature are summarized here.

Material	$\alpha \times 10^{-6}/\text{K}$	κ W/m-K	E GPa	Sources
TiO ₂	50	.25 to 7		[56, 81, 126]
Ta ₂ O ₅	3.6 to -44	.2		[66, 118, 126]
SiO ₂	.5 to 4.4	1.1 to 1.7	40 to 77	[68, 89, 81, 122]
Al ₂ O ₃		1.2 to 1.5		[81]

Table 2.2: Summary of noise effects

Source	Symbol	Large-spot length spectral density	Page
Bulk structural damping	$S_{SD}^{bulk}(f)$	$\frac{4k_B T}{(2\pi)^{3/2} f} \frac{\phi(f)(1-\sigma^2)}{E_0 r_0}$	10
Coating structural damping	$S_{SD}^{layer}(f)$	$\frac{2}{\pi^2} \frac{k_B T d}{E_0 r_0^2 f} \left(\frac{E_{coating}}{E_{bulk}} \phi_{\parallel} + \frac{E_{bulk}}{E_{coating}} \phi_{\perp} \right)$	11
Bulk thermoelastic	$S_{\alpha,T}^{bulk}(f)$	$\frac{8}{\sqrt{2\pi}} \frac{\alpha^2(1+\sigma)^2 \kappa k_B T^2}{(\rho C_V)^2 r_0^3 (2\pi f)^2}$	12
Coating thermoelastic (BV03)	$S_{\alpha,T}^{layer}(f)$	$\frac{4\sqrt{2}}{\pi} \frac{\alpha_{eff}^2 (1+\sigma)^2 d^2 k_B T^2}{r_0^2 \sqrt{\kappa \rho C_V} 2\pi f}$	13
Coating thermorefractive	$S_{\beta,T}^{layer}(f)$	$\beta_{eff}^2 \lambda^2 \frac{\sqrt{2} k_B T^2}{\pi r_0^2 \sqrt{2\pi \rho C_v \kappa} f}$	15
Coating photorefractive	$S_{\beta,P}^{layer}(f)$	$\frac{\beta^2 \lambda^2 S_{abs}(\omega)}{4\pi^3 r_0^4 \rho C_v \kappa f}$	23
Bulk photothermal	$S_{\alpha,P}^{bulk}(f)$	$\frac{\alpha^2(1+\sigma)^2}{2\pi^2} \frac{S_{abs}}{(\rho C_V \pi r_0^2)^2 f^2}$	16
Coating photothermal (sapphire)	$S_{\alpha,P}^{layer}(f)$	$\frac{\alpha_{layer}^2 S_{abs}(f)}{(\rho C_V 2\pi^2 r_0^2 f)^2} \left(1 - e^{-d\sqrt{i2\pi f/a^2}} \right)^4$	18

Table 2.3: Thermal properties of bulk materials. Values given are representative for bulk materials at 300K, and may differ among samples. TiO₂ data are for rutile bulk crystals, C-axis. SiO₂ data are for Corning 7980.

	α 10 ⁻⁶ /K	ρ 10 ³ kg/m ³	C_p J/kg-K	κ W/m-K	σ	r_t mm @ 100 Hz	$10 \times f_c$ Hz @ 1 mm
Al 6061 [40, 6]	23.6	2.7	897	167	.33	.33	110
Ag [85, 6]	18.9	10.5	235	429	.37	.53	280
Au [85, 6]	14.2	19.3	129	317	.42	.45	200
Cu [85, 90]	16.5	8.96	385	401	.36	.43	190
Ti [85, 6]	8.6	4.51	523	21.8	.30	.12	15
GaAs [85, 90]	5.4	5.3	330	56	.31	.23	50
Si [85, 90]	4.68	2.32	702	124	.27	.35	120
Be [85, 6]	11.3	1.85	1825	200	.03	.31	90
TiO ₂ [42]	9.19	4.26	711	13	.27	.083	6.8
Al ₂ O ₃ [39]	5	3.98	790	40	.29	.14	20
SiO ₂ [35]	.52	2.2	770	1.3	.17	.036	1.5
BK7 [96]	7.1	2.51	858	1.1	.21	.029	.8

Chapter 3

The Photothermal Effect

The purpose of the experiments described in this chapter is to measure how light intensity fluctuations in a Fabry-Perot cavity can cause length changes in the cavity. The dominant mechanism for this is believed to be the photothermal effect.

3.1 Introduction

The photothermal effect as a source of noise for LIGO was introduced by Braginsky, Gorodetsky, and Vyatchanin (BGV99) [22], who observed that shot noise fluctuations in the interferometers' laser power could drive surface fluctuations in the test masses. The way this is believed to happen is that the test masses' dielectric mirror coatings absorb a small amount of light power, converting it to heat, which diffuses through the mirror. The theory for photothermal noise in a test mass substrate (see §2.4.1) was worked out by BGV99 and Cerdonio *et al.* [32], assuming that the laser spot is much smaller than the mirror dimensions and that the absorption of light and conversion to heat takes place in a thin layer at the mirror surface.

De Rosa *et al.* [106] have observed this effect with two Fabry-Perot interferometers made from four identical fused silica mirrors, when they varied the power to one cavity and measure its length change relative to the other. Their measurements agreed well with the theory for homogenous substrates from 10 mHz to 200 Hz, but they did not address contributions from the mirror coatings.

I will discuss the design of an instrument that measures an interferometer's response to heat fluctuations at the surface of a mirror and how the response changes in the presence of a dielectric coating. This instrument is built around a cross-polarized Fabry-Perot interferometer, in which two beams of orthogonal polarization resonate simultaneously in the same cavity. One of the cavity's mirrors is a standard high-reflectivity interferometer mirror. The other, the "test" mirror, is a

specially made mirror with a medium absorption (1-3%) metal surface. One of the laser beams is intensity-modulated to alternately heat and cool the test mirror, while the other beam measures the motion of the surface of the test mirror. In order for the theories of BGV99 and Cerdonio *et al.* to apply to these measurements, it is necessary that spatial profiles of both beams overlap on the test mirror. Since these experiments are conducted with a Fabry-Perot cavity, this condition is automatically satisfied if both beams simultaneously resonate in the TEM₀₀ mode of the interferometer.

The photothermal effect is often used (particularly in the semiconductor industry) to measure thermal properties of materials [67, 9]. A common configuration is the modulated photothermal deflection experiment [83, 10], in which a “pump” laser beam, chopped into a square wave, strikes a sample at normal incidence, while a “probe” beam strikes the sample at a glancing angle. The pump beam is partially absorbed by the sample, raising a blister, which is observed by an angular deflection of the probe beam. A variation on this method uses the sample as one arm in a Michelson interferometer, with a displacement sensitivity of 4×10^{-13} m, limited by the pointing and intensity fluctuations of the probe beam [95]. While well developed, these methods are not optimal for measuring the photothermal effect in the mirrors that LIGO uses, as they work best on materials with highly absorptive surfaces. A new way to measure the photothermal response of a highly reflective sample is to use a Fabry-Perot cavity to recycle the pump beam power. This way, optical power that would otherwise be wasted can build up in the cavity until it is absorbed by the sample. Major advantages of this new technique over traditional photothermal methods are that it is more sensitive, only requires one laser, and has a large dynamic range. It can take measurements at audio frequencies above 5 Hz, with the sample displacement ranging from 4×10^{-15} m to 10^{-9} m on a tabletop.

This chapter presents measurements of the photothermal response of several mirrors, whose preparations are described in §3.2.6. The first measurement was done with a solid aluminum mirror, whose behavior is compared with the homogenous solid theory [32] from 10 Hz - 4 kHz. Since recent measurements [5, 20, 30, 56, 118, 127] suggest that the thermal expansion coefficient of thin films used by LIGO could be on the order of 2×10^{-6} /K, several times higher than for bulk silica [35], I examined BK7, fused silica, and sapphire substrates, each with mirrored and unmirrored samples. The samples were used to find whether the mirror coating has a substantial effect on the photothermal response. In order to give these samples similar reflective surfaces without strongly influencing heat flow, these samples all have a thin ($\sim 1.8 \times 10^{-7}$ m) layer of gold evaporated on them.

To summarize, the samples tested are

Solid aluminum

Gold-coated fused silica

Gold-coated fused silica with a 30-layer HR mirror ($\text{TiO}_2/\text{SiO}_2$)

Gold-coated BK7

Gold-coated BK7 with a 30-layer HR mirror ($\text{TiO}_2/\text{SiO}_2$)

Gold-coated c-axis sapphire

Gold-coated c-axis sapphire with a 30-layer HR mirror ($\text{TiO}_2/\text{SiO}_2$)

3.2 Materials and Methods

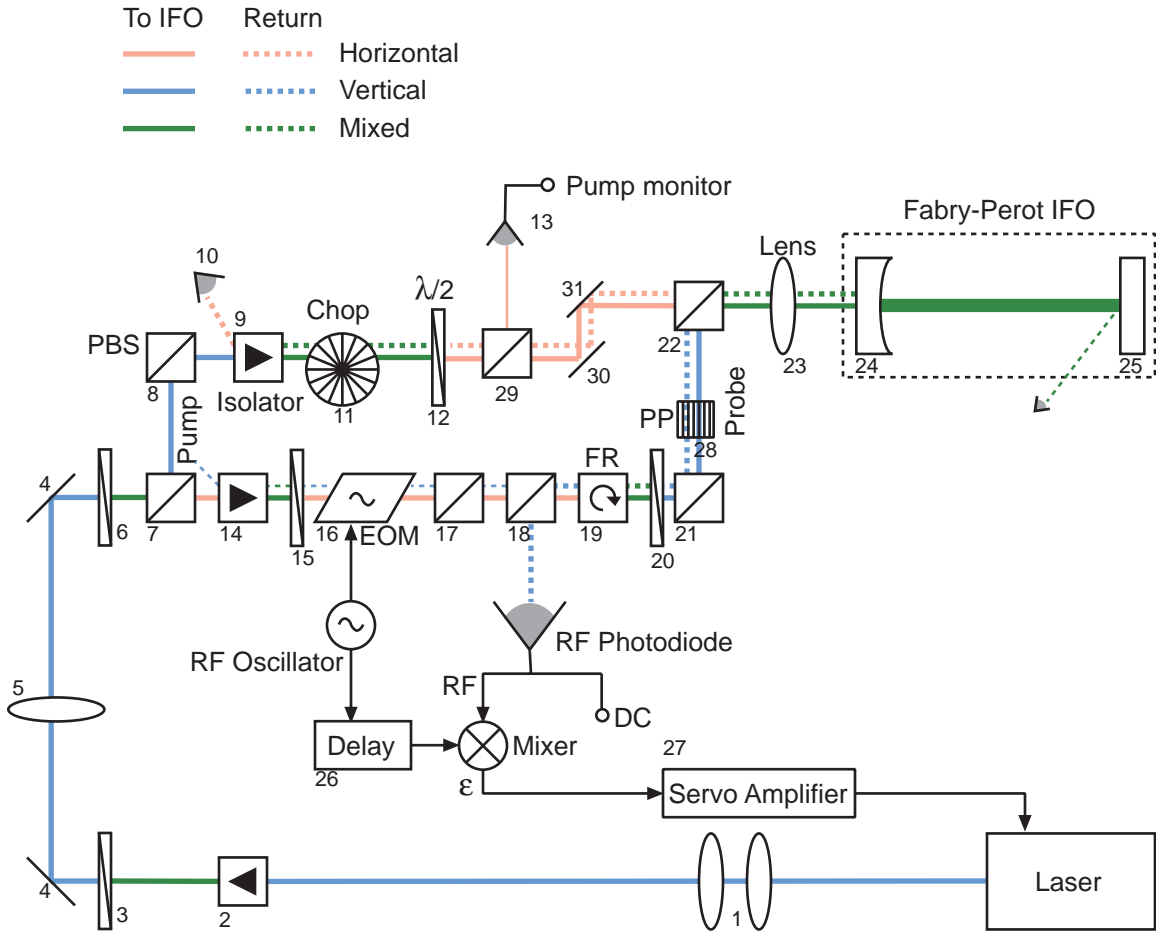
A laser beam is split into two cross-polarized beams, denoted *pump* and *probe*, then recombined and resonated together in a Fabry-Perot interferometer (IFO). The *pump* beam is used to modulate the light power that strikes the test mirror, while the *probe* beam detects length changes in the interferometer with the Pound-Drever-Hall (PDH) [43, 41] optical heterodyne technique and also locks the laser frequency to the cavity resonant frequency. The *pump* beam is periodically interrupted with a chopping wheel, converting it to a pulsed beam with a 50% duty cycle. Analyzing the length changes at the chopping frequency comprises a direct, lock-in measurement of the photothermal effect, as the PDH signal represents the average displacement of the test mirror surface, weighted by the Gaussian beam profile [82, 22, 128].

The greatest challenge in building this instrument is in reducing cross-coupling between the reflected *probe* and *pump* beams. The purpose of the highly redundant polarizing optics is to minimize the amount of *pump* light reflected back along the *probe* path. In implementing this device, I used two designs to counteract cross-coupling: a preliminary layout sufficient for measuring the photothermal response in aluminum, and a more complicated layout with better mode matching and more polarizing optics to reduce cross-coupling noise for the other samples.

3.2.0.1 Aluminum measurements

To construct the instrument (Fig. 3.1), I divide the beam from a laser (x3.2.5) into the *pump* and *probe* beams with a polarizing beamsplitter (PBS) (7). A half-wave plate (6) determines the power

Figure 3.1: Experiment layout for aluminum. Shaded lines represent laser beams, and solid black lines represent wires.



distribution. The *pump* power is chosen so that the cavity length changes are above the background noise (see §3.2.5.4) and within the linear range of the detector (see §3.2.7.1). The *probe* power is chosen to take full advantage of the dynamic range of the photodiode. The *pump* and *probe* powers vary for the different substrate measurements. The chopper (11) is in the *pump* path only. The *probe* beam travels through an electro-optical modulator (EOM) (16), which adds radio frequency (RF) sidebands, powered by a RF Oscillator (see §3.2.5).

The beams are recombined with a PBS (22), are injected into the IFO, and are partially reflected. The reflected *pump* beam returns along its path and is diverted to a photodiode (10) by a Faraday isolator¹ (9). The reflected *probe* beam, including the RF sidebands, returns along its path, but is

¹A Faraday rotator [48] rotates the polarization of a beam by 45° in a direction determined by a static magnetic field. A Faraday isolator is a Faraday rotator with linear polarizers at its input and output, so as to allow light to pass through it

diverted by a Faraday rotator (19) and a PBS (18) to the RF photodiode (RFPD). The output of the RFPD is demodulated according to the PDH method, giving the signal that measures changes in the cavity length. The PDH signal is also used with a feedback servo (27) (see §3.2.4) to keep the laser resonant with the IFO.

For the aluminum measurement, the interferometer finesse² is only 37, so mode matching and alignment requirements are not very strenuous. Lenses (1, 5, 23) and steering optics on kinematic mounts (4, 6, 11) focus and align the beams for injection into the interferometer.

Faraday isolators (2, 9, 14) prevent reflected beams from feeding back to the laser. Without the isolators in the *pump* and *probe* beams (9,14), spurious reflections in the first PBS (7) can cause a fraction of the *pump* light reflected from the cavity to travel through the EOM, reflect from the cavity, and finally reach the RF photodiode, creating cross-coupling noise. These and extra PBSs (8, 21, 17) and a plane polarizer (PP) (28) reduce the amount of *pump* light that reaches the RFPD. Half-wave plates (3, 6, 12, 15, 20) rotate beam polarizations to compensate for rotations by Faraday isolators (2, 9, 14) and rotators (19), misalignments between PBSs, and to place the beam in horizontal or vertical polarizations before reflection or transmission through any optics.

The IFO is made from two mirrors held 31.8 cm apart by an aluminum spacer block. The input mirror (24) is a concave fused silica substrate with a low absorption dielectric mirror coating, a reflectivity of 95%, and a radius of curvature of 50 cm. The “test” mirror (25) is mounted at the other end of the interferometer cavity (see §3.2.5.5). The test mirror has an absorptivity of around 6%, while the input mirror’s absorptivity is much less. Since the photothermal effect scales linearly with the amount of power absorbed, and depends on absorption, IFO length changes due to the photothermal effect will be dominated by the test mirror. The absorption of the test mirror is determined by fitting its measured photothermal response to Eq. 2.26.

A drawback with this configuration is that the beam does not couple well into the cavity. Since cross-coupling noise depends on the amount of power reflected from the cavity, I chose to improve the mode matching, which imposed constraints (see §3.2.1) that forced changes to the optics layout.

3.2.0.2 BK7, Fused Silica, Sapphire

In this version of the instrument, the beam makes several changes between horizontal (H), vertical (V), and mixed (M) polarizations as it travels around the optics table. H-polarized light passes

in only one direction.

²Finesse is a measure of the optical gain of a cavity. See §5.3.

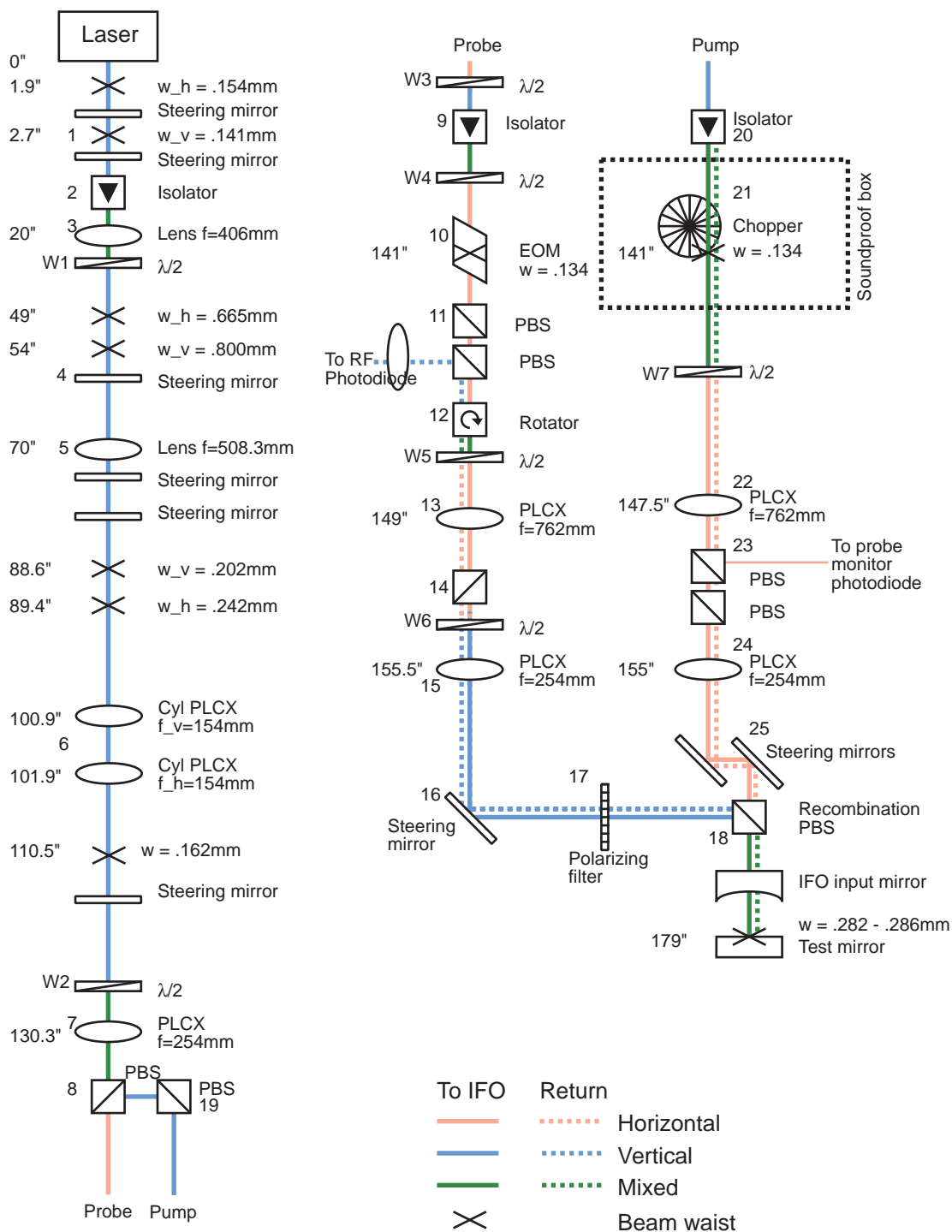


Figure 3.2: Linearized view of the experiment layout for BK7, fused silica, and sapphire. Shaded lines represent laser beams, and solid black lines represent wires. Black x's represent beam waists. Waist radii are measured in $1/e$ of field amplitude, in accordance with the formalism of Kogelnik and Li [77].

directly through polarizing beamsplitter (PBS) cubes, while V-polarized light is reflected. Mixed polarization occurs after Faraday optics or when H- and V-polarized beams are combined. To make a circular beam spot that couples well to the cavity requires a long optical path (see §3.2.1). Fig. 3.2 shows the unwound optical layout, with the beam waists³ marked. Details of the mode-matching procedure are given in §3.2.1.

Starting at the laser, the elliptical, V polarized beam travels through a short periscope (1) and through a Faraday isolator (2). The periscope is used to find a “sweet spot” with minimum distortion by the isolator. Now with M polarization, a lens (3) refocuses the beam to form large, elliptical waists at around 50”. A half-wave plate rotates the beam’s polarization to restore vertical polarization before a 90° turn at a steering mirror (4). These mirrors (New Focus 5014 or CVI Y1-1025-UNP-FG) are birefringent, and can convert a beam with linear M polarization into one with partial circular polarization⁴, so it is important to put the light into either H or V polarization with a half-wave plate (W1) before changing its direction.

Another lens (5) focuses the beam to form a waist as the beam reaches the end of the table and returns back. Two cylindrical lenses (6), oriented horizontally and vertically, focus the beam to a single circular waist at 110.5” before the beam takes another 90° turn. A half-wave (W2) plate selects the power distribution between the *probe* and *pump* beams before the beam passes through another mode-matching lens (7). The beam is split into *probe* and *pump* arms by a polarizing beamsplitter (8).

In the *probe* path, a half-wave plate restores vertical polarization for the light to pass through another isolator (9). Another half-wave plate rotates the beam to horizontal polarization for the electro-optic modulator (EOM) (10), which is also birefringent. The EOM is positioned about a tight beam waist, to minimize clipping at its narrow apertures. To make sure the beam is purely H-polarized, it passes through two more PBSs (11). Each beamsplitter has an extinction ratio of 1000 : 1 [36], and with good alignment, their collective extinction ratio⁵ is improved to about 10⁵ : 1.

After this polarization filter, the *probe* beam goes through a Faraday rotator, which is just an isolator without its polarizing filters. A half-wave plate brings the beam back to H polarization

³Laser beams can be focused to a minimum spot size, called a beam waist. They expand symmetrically on both sides of the beam waists with a hyperbolic profile [77].

⁴Determined by reflecting a $\frac{H+V}{\sqrt{2}}$ beam off a steering mirror at 45°, and measuring the power transmitted and reflected by the second of two polarizing beamsplitter cubes.

⁵Determined by measuring the reflected power when V-polarized light (which should not be transmitted) is shone through a pair of beamsplitters.

so that it will pass straight through another PBS (14). Then, another half-wave plate rotates the beam to V polarization so that it will reflect at the recombination PBS (18). A compound mode-matching telescope (13, 15) images the final beam waist at the surface of the test mirror. A linear glass polarizer (17) on a precision rotary mount is critical for removing H-polarized light from the reflected beam. The steering mirror (16) and final PBS form the steering periscope for the *probe* beam.

Upon reflection from the cavity, the *probe* beam returns along its path until the Faraday rotator (12). There, it is shifted to V polarization, and is bent out of the main beam path by the next beamsplitter, where a cat's eye lens⁶ focuses it onto the RFPD.

From the start of the *pump* path at (18), a PBS (19) takes the beam through a 90° turn into a Faraday isolator (20). The chopper wheel (see §3.2.5.4) intersects the beam at a small waist to help reduce systematic phase noise (see §3.2.7.6). The beam is then rotated to H polarization, and passes through a mode-matching telescope (22, 24) and polarization filter (23) before recombining with the *probe* beam at a PBS (18). A neutral-density filter may be placed before the alignment periscope (25) to attenuate the *pump* beam. Upon reflection from the cavity, the *pump* beam returns along its path until it is arrested by a beam dump at the Faraday isolator (20).

With the polarizing optics (see §3.2.2) set correctly, it is possible to reduce the power from the *pump* beam reaching the RFPD to 10^{-5} of that impinging upon the cavity. This is measured continuously as part of the data acquisition process to characterize the cross-coupling noise.

3.2.1 Mode matching

The laser spot size ($1/e$ of field amplitude) at the test mirror is 0.28 mm, determined by the length of the cavity and the curvature of the input mirror. Spot sizes used for mode matching calculations refer to the radius w at $1/e$ of the central field amplitude, so that $w = \sqrt{2}r_0$, where r_0 is the spot size as used in Chapter 2 and in much of the thermal noise literature. The TEM₀₀ resonant axis of the IFO is determined by the line normal to the surface of the test mirror that passes through the center of curvature of the input mirror; with both *pump* and *probe* beams optimally aligned to the cavity, they are collinear in the cavity and the *pump* beam heats the same spot that the *probe* beam senses.

The mode matching was calculated with a spreadsheet⁷ [103] using the formalism of Kogelnik

⁶The lens's focal point is at the RFPD.

⁷Included with the online version of this thesis, available at <http://library.caltech.edu/etd/>

and Li [77]. The beam waists indicated on Fig. 3.2 reflect measurements made with a Photon, Inc. dual-axis beam scanner (www.photon-inc.com).

The purpose of the lenses in this instrument is to convert the elliptical beam emanating from the laser into a circular spot matched to the IFO, 179" from the front of the laser enclosure. The Faraday isolator (2) immediately after the laser distorts the beam, so the initial beam waists are not useful for the mode matching calculations. Therefore, the first lens (3) was chosen to produce well-defined Gaussian beam waists at around 50" from the laser, which were taken as the starting point in the beam propagation equations. The next lens (5) was chosen to produce a nearly circular beam, with horizontal and vertical waists displaced by less than an inch (at 89"). This is necessary to allow two cylindrical lenses (6) to image a single circular waist at 110.5". The mounting hardware I used required the cylindrical lenses to be at least an inch apart, so an iterative optimization procedure was used to position the lens (5) so that a solution would be possible. After this circular waist, the beam propagates until another lens (7), whose purpose is to image a waist at the chopper wheel and the EOM.

Having a beam waist at the chopper helps the *pump* beam's amplitude modulation have a duty cycle near 50%, and having a beam waist at the EOM reduces clipping at the EOM's narrow apertures. Each of the arms have a mode matching telescope (13 and 15 in *probe*, 22 and 24 in *pump*) to focus the beam to a waist at the test mirror. The positions of these mirrors are initially determined by calculations with the spreadsheet, then adjusted on the table to minimize the interferometer's reflectivity on resonance.

A critical constraint is that there be 30" to accommodate optics and mounting hardware between the lens (7) and the input mirror of the cavity, with minimal optics between the last lenses (15,24) and the cavity.

3.2.2 Polarization optics

Cross-coupling noise in this experiment is like any other scattered light phenomenon [102]: a stray beam at the carrier frequency but with a random phase beats against the sidebands to make a spurious PDH signal. The technique for measuring the cross-coupling is simple: with the *probe* beam blocked immediately after the first PBS, measure the amount of light that reaches the RFPD.

I have developed the following procedure for optimizing the polarizing optics:

1. Turn off all the room lights except for one. This will make it easier to use IR viewer cards.

2. Place a PBS immediately after the first waveplate (W1), and rotate W1 to minimize the light transmitted by the PBS. Remove the PBS.
3. Set W2 so that the *probe* beam has twice as much power as the *pump* beam.
4. Replace W4 with a power meter. Rotate W3 to maximize the power transmitted by the isolator (9).
5. Replace the PBSs (11) with a beam scanner, and adjust the tip/tilt of the EOM to minimize beam distortion.
6. Restore W4 and PBSs (11) and minimize the power reflected to the side by the PBSs.
7. Remove W5 and use the beam scanner at PBS (14) to minimize beam distortion from the Faraday rotator (12).
8. Restore W5 and rotate it to minimize the power reflected to the side by the PBS (14).
9. Block the *probe* beam at W3 and restore the *pump* beam. Rotate W7 to minimize the light deflected by the PBS (23).
10. With *probe* still blocked, restore the polarizing filter (17) and rotate it to minimize the light transmitted back through it.
11. Restore the *probe* beam and rotate W6 to maximize the power reaching the cavity.

3.2.3 Alignment

Since the test mirror is opaque⁸, I have developed the following procedure to align the lasers to the cavity:

1. Attach the test mirror to the end of the spacer block, with no input mirror. With a 2-mirror horizontal periscope, manipulate the *probe* beam so that it passes through the center of the spacer input aperture and reflects back on itself.
2. Attach the input mirror to the other end. With an IR-sensitive video camera, look through the top of the spacer for a constellation of spots on the end mirror. Scan the beam with the periscope until one appears, and then minimize the scatter of the cluster. The beam should still pass through a spot near the center of the input mirror.

⁸The gold-coated blank substrates transmit a few microwatts of power when the laser is resonant with the cavity.

3. Break a microscope slide cover slip in half. Shine a red laser pointer at it to make sure that it doesn't form an etalon. If it does, you will only be able to see a TEM_{01} mode in the IFO.
4. Turn off the room lights so they don't saturate your cameras.
5. Mount the cover slip inside the cavity at a 45° angle to the horizontal, so that it deflects light upwards into your video camera.
6. Set up a function generator to drive the laser PZT input with a 10Vpp sine wave at 13 Hz (or another frequency relatively prime to 30Hz). Watching the video monitor, manipulate the periscope to make the beam spot symmetric.
7. Setup up photodiodes to monitor the power returned from the cavity and the power inside the cavity. Pointing a photodiode at the test mirror works well. Set up an oscilloscope to trigger on the PZT input and view the photodiode
8. Turn the laser temperature dial until a round TEM_{00} spot is visible (this occurs at a slightly higher laser temperature than the TEM_{01} mode).
9. Without changing its angle, translate the beam horizontally and vertically to maximize the power inside the cavity. You'll need to put the clear cover on top of the cavity to keep the cover slip from blowing around.
10. Remove the cover slip, and again maximize the power inside. This should also minimize the reflected power on resonance. If the input and test mirrors have the same reflectivity, you should be able to reach at least 90% visibility in the carrier. If the test mirror is an "unmirrored" sample, the cavity will transmit a few μW , which a CCD can detect if you turn off the room lights.
11. Place a frequency-doubling viewer disk in front of the cavity, and align the *pump* beam to the *probe*. It helps to set the chopper at a few Hz.
12. Position a photodiode at the *pump* isolator's beam dump (20) to measure the *pump* visibility. Manipulate the *pump* alignment to maximize its throughput. You shouldn't need to use the cover slip for this.

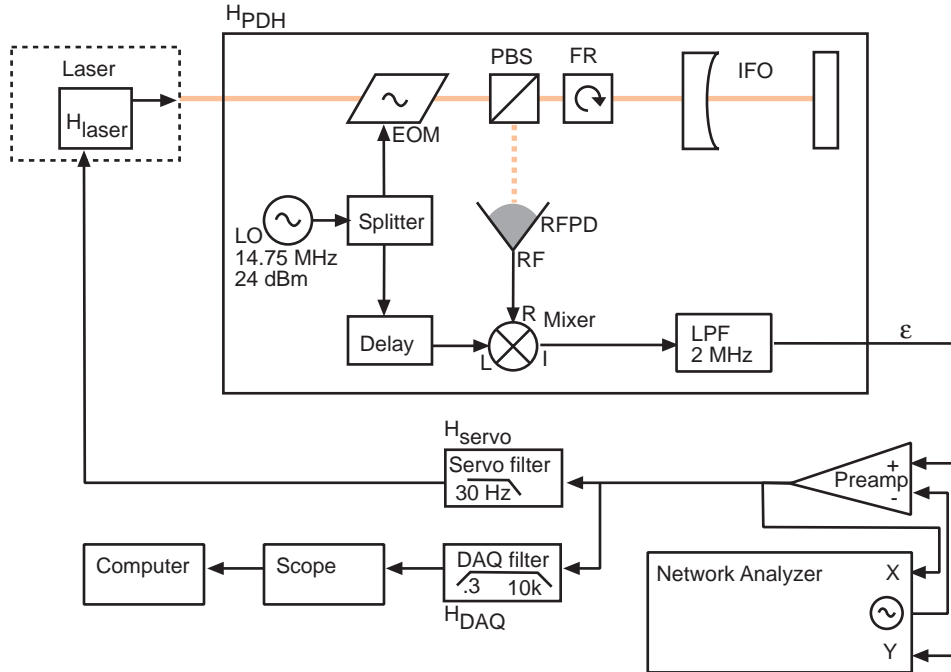


Figure 3.3: Length sensing and control layout, with streamlined optics. Solid lines represent laser beams travelling to the interferometer, and dashed lines represent beams travelling away from the interferometer.

3.2.4 Length sensing, control, and calibration

A control servo locks the laser to the cavity, following the method in Day [41] (Fig. 3.3). The PDH voltage (ε) represents the difference between the laser frequency and the cavity resonance frequency. The factor converting this voltage to units of length is measured in the calibration process.

To detect the length changes, a local oscillator (LO) produces a 10Vpp, 14.75 MHz sine wave. This signal is split, and fed into a tuned resonant electro-optic modulator (EOM) and, via delay cables, to a mixer. The EOM phase-modulates the beam, adding symmetric sidebands, each with 3% of the total beam power. The mixer uses the LO signal to demodulate the RFPD output, the result of which is fed into an in-line low-pass filter (LPF) to remove high frequency components. The output of the LPF forms the PDH signal.

The PDH signal is buffered with a unity-gain differential preamplifier, and fed back to the laser via a filter, H_{servo} . The servo filter is changed between measurements, but is generally a single-pole low-pass filter with gain chosen so that the overall unity gain frequency is below 200 Hz. For data acquisition, the preamp output is subjected to a filter (H_{DAQ}) to reduce DC drift and antialiasing. Data are measured with a Tektronix 3014 digital oscilloscope and copied to a portable computer

(see §3.2.7).

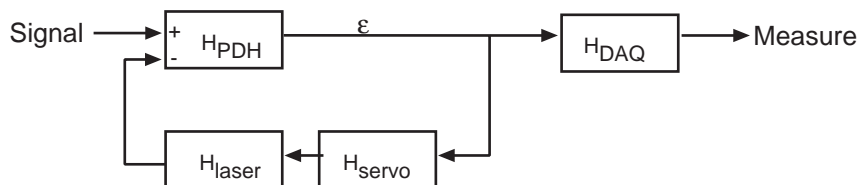


Figure 3.4: Feedback servo block diagram.

The process for determining the PDH response is based on comparing the measured open loop transfer function (OLTF) of the servo to known parameters. First, the OLTF is measured in situ with a network analyzer. With a swept sine signal injected into the preamp, the complex transfer function is

$$OLTF = -\left\langle \frac{Y}{X} \right\rangle = H_{laser} H_{PDH} H_{servo} \quad (3.1)$$

where RF and optical components are treated as a lumped parameter, H_{PDH} . As H_{servo} is known, and H_{laser} is measured independently, measuring the $OLTF$ determines H_{PDH} (see Fig. 3.5). To recover the signal corresponding to the cavity's length changes, we observe (see Fig. 3.4)

$$\begin{aligned} \varepsilon &= H_{PDH}(Signal - H_{laser} \cdot H_{servo} \cdot \varepsilon) \\ Signal &= \varepsilon \left(\frac{1}{H_{PDH}} + H_{laser} \cdot H_{servo} \right) \\ Signal &= \frac{Measure}{H_{DAQ}} \left(\frac{1}{H_{PDH}} + H_{laser} \cdot H_{servo} \right) \end{aligned} \quad (3.2)$$

Both the magnitude and phase of the collected data need to be compensated by this function. With the laser locked and the calibration known, the background noise spectrum is obtained by multiplying the PDH signal by the factor in Eq. 3.2. The dominant source of background noise seems to be acoustic. Therefore, when gathering data, it's important not to talk, listen to the radio, or move around. The cleanroom's laminar flow fans are not the greatest source of noise, and they are necessary to regulate the spacer block's temperature over long timescales. Fig. 3.6 shows a noise curve obtained under ideal operating conditions (after everyone else the building has gone home).

Figure 3.5: Measured open-loop transfer function for the mirrored sapphire measurement, fit with a model for *OLTF*. The data are compensated for the effects of the servo up to 4 kHz. The *OLTF* magnitude at DC is 7.5, the electronic gain is 1, and the DC H_{laser} gain is 6 MHz/V. This sets $H_{PDH} = 1.25V/MHz$. The DC calibration factor for the instrument is therefore $\frac{\lambda L}{c H_{PDH}} = 8.7 \times 10^{-10}$ m/V. With a finesse of 80, the line width is 1.25×10^{-8} m.

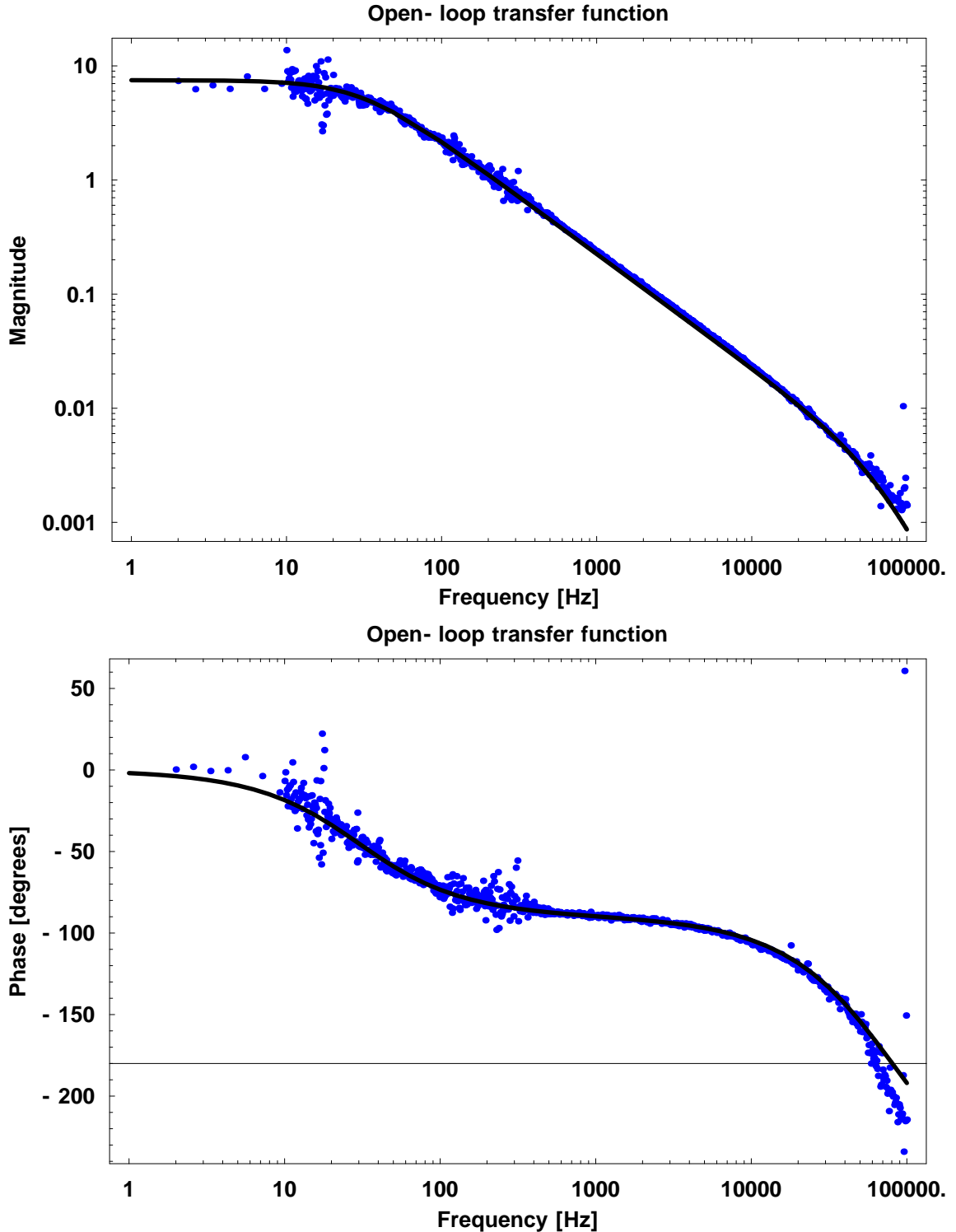
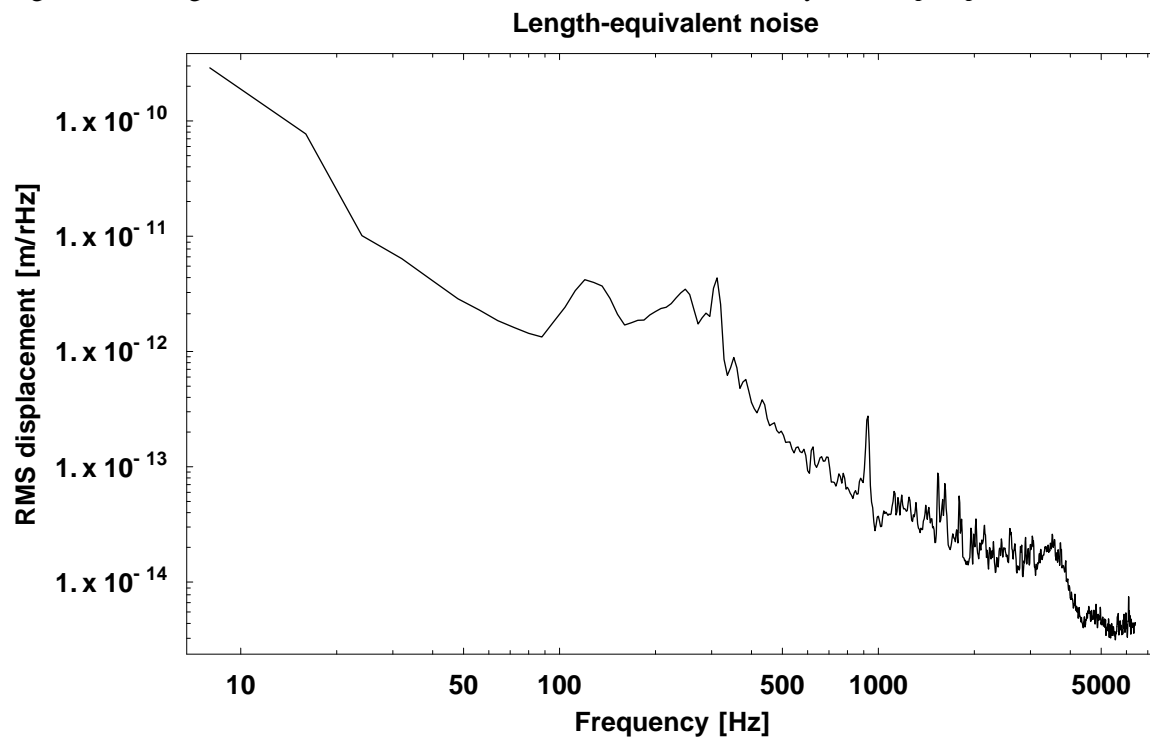


Figure 3.6: Length noise, measured with the laser locked to the cavity and the *pump* beam blocked.



3.2.5 Components

Most of the optics (lenses, mirrors, beam splitters, and wave plates) are stock components purchased from CVI Laser Corp. Part numbers are listed in Table 3.1, and detailed descriptions of the parts follow.

3.2.5.1 Mounting hardware

All the parts used in this experiment lie on a single optical table. Some of them require special mounting hardware.

- Beam splitters are on 3-axis tilt stages, bolted to a steel pedestal clamped to the optical table. The stress from clamping them down tends to induce birefringence, so double-stick tape holds them in place.
- Most of the steering mirrors are held in standard mirror mounts. Those used for alignment to the cavity (16, 25) are held by precision mounts (Lee's Mount replicas). Mirror mounts
- Lenses are mounted in standard 1" \varnothing lens holders, bolted to 1" \varnothing steel pedestals clamped to the table. The pedestals are 2" high with 1/8" stainless steel washers to position the center of the lens 3" above the table surface.
- Non-critical wave plates (W1, W2, W3, W4) are set in standard rotation stages, while the others are set in precision rotation stages with fine-tuning knobs. Rotation stages are bolted to 1" \varnothing steel pedestals, clamped to the table.
- The EOMs and Faraday components are mounted to 4-axis tip/tilt stages. The EOM's mounting hole mates conveniently with these. The Faraday parts are attached to the stages with 5-minute epoxy. The elevation of the tip/tilt stage is set by setting it on a large block of metal of appropriate thickness, while two long 1/4"-20 bolts anchor the stage directly to the table.
- The polarizing filter comes in a custom mounting ring, which is epoxied to a rotation stage.

3.2.5.2 Photodiode

The length sensing and control system is based on a LIGO standard RF photodiode with DC gain of 40V/W. A neutral density filter in front of the RFPD attenuates the light power so that the PDH

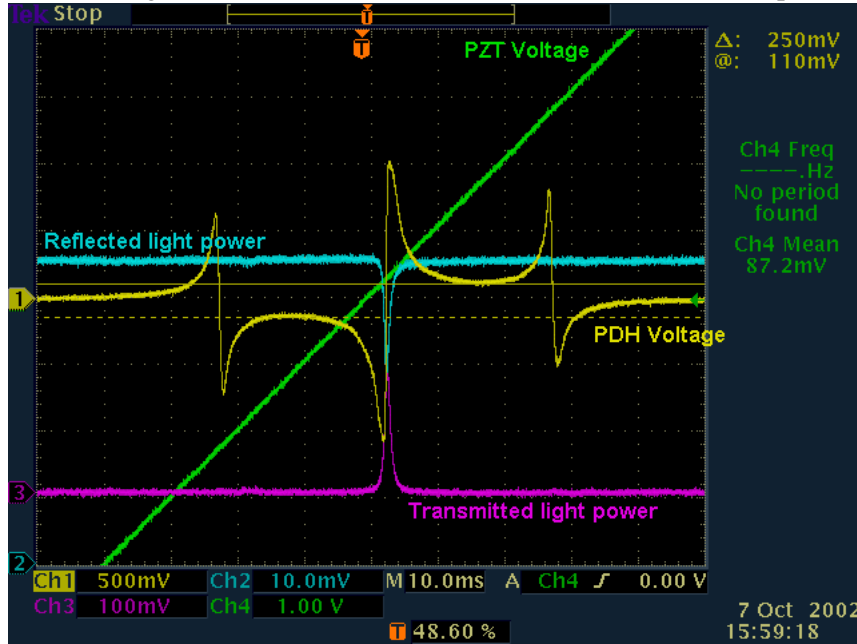
Table 3.1: Optical and electronic components and hardware

Identifier	Manufacturer	Part number
Interferometer input mirror	CVI	PR1-1064-95-1025
Sample: Al	Janos and CVI	see §3.2.6
Samples: BK7, Al ₂ O ₃ , SiO ₂	CVI	see §3.2.6
Steering mirrors	CVI	Y1-1064-1025-UNP
Standard mirror mounts	Thorlabs	KM1 or KM1HC
Precision mirror mounts	CVI	PLQ-10
Standard rotation stage	Thorlabs	RSP1
Precision rotation stage	CVI	1180
Polarizing beamsplitter	CVI	PBS-1064-100
Beamsplitter stage	New Focus	9411
RF photodiode	LIGO	T980068[86], D980454[112]
Faraday rotator and isolators	Electro-Optic Technologies	1064 μ isolator, 4mm aperture
Electro-optic modulator	New Focus	4003
Tip/tilt stage	New Focus	9071
Pedestals	CVI	75-xx
Pedestal clamps	CVI	71
RF Splitter	Mini-Circuits	ZFSC-2-1W
RF Mixer	Mini-Circuits	ZAY-3
LPF (Low-Pass Filter)	Mini-Circuits	BLP-1.9
Preamplifier	Stanford Research	SR560
Servo filter	Stanford Research	SR560
DAQ filter	Stanford Research	SR560
Network Analyzer	Stanford Research	SR785
Local RF oscillator	Stanford Research	DS345
Delay	EG & G	BNC cable box
Data capture	Tektronix	TDS3014

signal stays within its linear range of $2 V_{pp}$. The photodiode's DC response saturates at 100 mW, but its tuned RF amplifier saturates if its output amplitude is more than a few volts.

3.2.5.3 Laser

Figure 3.7: Laser PZT Calibration. The sidebands are separated by 14.75 MHz.



The laser is a 400 mW, 1064 nm, diode-pumped Nd:YAG non-planar ring oscillator (LightWave Electronics Model 126, <http://www.lwecorp.com/>), rigidly mounted to the optical table at a 3" beam height. The laser's power supply allows for controlling the laser frequency by adjusting the temperature and by mechanically stressing the crystal with a PZT. Slow changes over several GHz can be affected with temperature, while fast changes over a few MHz require the PZT.

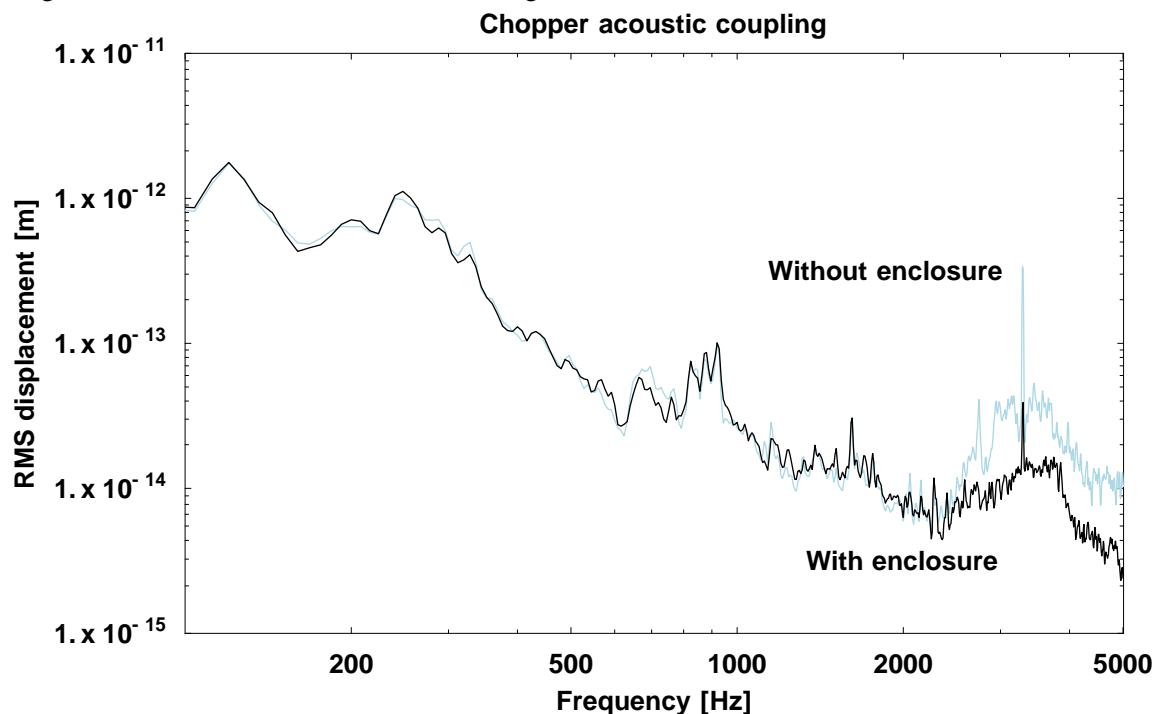
The DC value of the transfer function of the laser PZT, H_{PZT} , is found by measuring the PDH signal for a high-finesse (500) cavity while applying a slow (10 Hz) voltage ramp to the PZT (Fig. 3.7). The beam resonates in the IFO at three frequencies corresponding to the carrier and two sidebands, each 14.75 MHz away from the carrier frequency. The calibration factor is simply $\frac{2 \times 14.75 \text{ MHz}}{\Delta V}$.

The PZT also has a high frequency pole, which is determined from the servo transfer function (see §3.2.4). In 2000, the H_{PZT} was measured to be 6.3 (MHz/V) with a pole at 55kHz. By 2003, the DC gain had degraded to 6.0 (MHz/V). For all the data reported here, the DC PZT gain is 6 MHz/V. The PZT appears to have a single pole at 55 kHz for the Aluminum mirror experiments,

which were done in mid-2002. By 2003, when the other materials were measured, the PZT pole decreased to around 32 kHz, possibly from failure of the bond between the PZT and the laser crystal.

3.2.5.4 Chopper

Figure 3.8: Effectiveness of the acoustic isolation box around the chopper wheel. Light blue: rms length noise without the box. Black: rms length noise with the box.



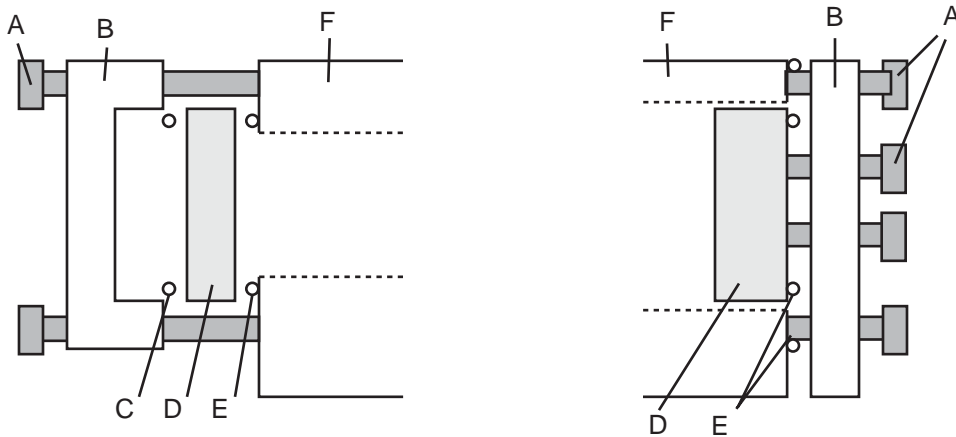
The intensity modulation of the *pump* beam is provided by an SR540 chopper wheel from Stanford Research Systems (www.thinksrs.com). The chopper works with two wheels, for low (400 Hz and below) and high (400 - 4000 Hz) frequencies. The chopper wheel rests on a 2-layer stack of steel and rubber, with resonant frequencies of a few Hz. The stack is enclosed in a box made from 1/8" aluminum sheet metal and lined with closed-cell foam. The best foam is that from the beam scanner's shipping carton. This attenuated the sound by 20 dB at high frequencies. These measures are sufficient to reduce the acoustic coupling of the chopper wheel to the cavity to less than 2×10^{-13} m/rHz at its maximum at 3.9 kHz, which is comparable to the background noise level. Fig. 3.8 compares the rms length-equivalent noise of the interferometer. These data are taken with the *pump* beam blocked.

The manufacturer specifies 0.2° rms phase jitter on the slow wheel and 0.5° rms phase jitter on

the fast wheel, but its long-term phase stability is not so reliable. Therefore, to compute a system's response to the chopper, it's better to add together many short duration samples than to integrate over a long time.

3.2.5.5 Cavity

Figure 3.9: Exploded view of interferometer assembly scheme. Left: input end. Right: "test" end (Aluminum mounting scheme shown). A: bolts, B: clamp, C: O-ring, D: mirrors, E: Indium wire, F: spacer



The interferometer cavity is an Al-6061 spacer block with mirrors attached to the ends (Fig. 3.9). For light to pass through it, the spacer block has a groove cut down the center and holes drilled through the ends. The block is rigidly bolted to a flat aluminum plate, which is clamped to the optical table.

At the front end, the input mirror ($R=95\%$, 50cm radius of curvature) is clamped to the face of the spacer block. The mirror clamp is a block of aluminum with a .75" clearance hole in the center, counter-bored to 1.010"Ø to hold a mirror. A viton O-ring on the back surface and an indium O-ring on the front surface of this mirror hold the mirror snug. At the other end, the mounting scheme varies. For the aluminum mirror (shown), the back of the mirror is bolted to a plate, which is bolted to the cavity. For the other mirrors, an aluminum plate with a hole through the center is affixed to the cavity, and the test mirror is anchored against the plate in the same manner as the input mirror. The mode matching is chosen so that the laser spot radius varies by only 2% for the range of cavity lengths explored in this scheme.

As the spacer block is very sensitive to temperature changes, it has to be shielded from light scattered by the test mirror. The interior surfaces of the cavity are lined with layers of nonconductive

plastic and aluminum foil, so that light scattered by the IFO mirrors will not be absorbed by the sides of the block. The top of the channel is covered with a piece of transparent acrylic to reduce acoustic noise. The laboratory environment is not thermally regulated, so the cavity tends to shrink after sundown – a temperature change of 0.1K is sufficient to sweep the interferometer through one free spectral range! A layer of black foam on the sides and top of the cavity helps minimize conductive heat transport and slow down its thermal drift. Compensation for thermal drift can also be provided by a heat source, such as an incandescent lamp or a finger on the base of the spacer block.

Near resonance, the IFO input mirror is slightly birefringent, and partially circularizes the beams. Therefore, cross-coupling noise varies somewhat, and is continuously monitored while acquiring data.

3.2.6 Sample preparation

For reasons of expediency and cost, the samples I used varied in their preparations. The BK7, fused silica, and sapphire samples are modifications of standard mirrors and windows purchased from CVI Laser Corp. Aluminum mirrors are sold by several companies, including Polished Metals Ltd. (800-526-7051), Optimum Manufacturing Corp. (800-858-2249), Surface Finishes Co. Inc. (630-543-6682), Opticon (978-663-6105), Optical Filter Corp. (603-357-7662), and Janos Technologies Inc. (802-365-7714).

The gold coatings applied at Caltech were all made at the same time. They were formed by thermal evaporation of gold (.9999) under vacuum. The thickness of the coating was measured to be 180 nm by a crystal rate monitor. A “protected gold” mirror is a proprietary process done by CVI. It starts with a coating of gold, approximately 200nm thick. On top of the gold layer is a thin dielectric layer, to protect the gold from rubbing away. Fig. 3.10 shows a side view of the mirror, and Fig. 3.11 shows a comparison of the length scales.

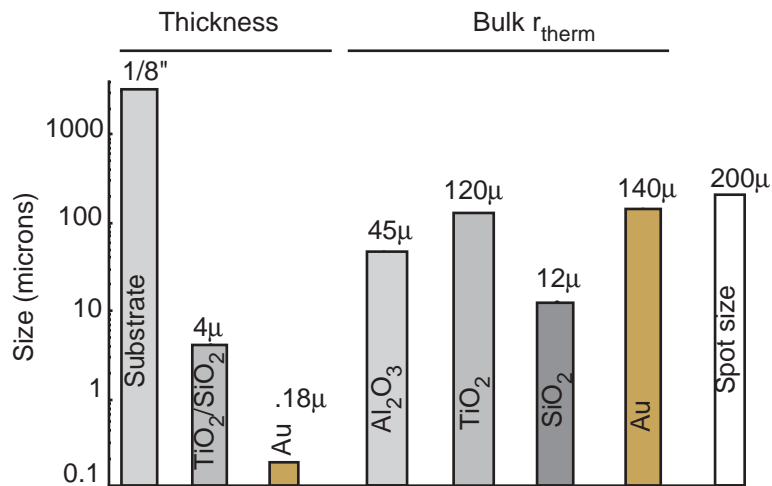
The thermal conductivity of the Au should not strongly affect the heat flow, as the gold layer conducts much less heat than the substrate or the coating. The radial thermal resistance of a thin disk scales with $1/2\pi\kappa t$, where t is the thickness of the disk. The longitudinal (normal to the mirror surface) thermal resistance scales with t/κ in this direction, the gold coating has much less resistance to heat flow than the layers below it. A summary of thermal impedances is listed in Table 3.2.

All these mirrors scatter a considerable amount of the light that strikes them. The scattered light

Figure 3.10: Side view (not to scale) of sapphire samples. The dielectric stack is the same on the BK7 sample and similar (same number of layers) on the fused silica sample [34]. The gold layers on the other samples have similar opacity, and are likely to have a similar thickness.

	Layer	Thickness	r_t (100 Hz)	r_t (1000 Hz)
No stack	Au	$1.8 \cdot 10^{-7} \text{m}$	$4.5 \cdot 10^{-4} \text{m}$	$1.4 \cdot 10^{-4} \text{m}$
	Al_2O_3	$3.2 \cdot 10^{-3} \text{m}$	$1.4 \cdot 10^{-4} \text{m}$	$.44 \cdot 10^{-4} \text{m}$
Dielectric stack	Au	$1.8 \cdot 10^{-7} \text{m}$	$4.5 \cdot 10^{-4} \text{m}$	$1.4 \cdot 10^{-4} \text{m}$
	$(\text{SiO}_2/\text{TiO}_2)^{15}$	$4 \cdot 10^{-6} \text{m}$	$.4 \cdot 10^{-4} \text{m}$	$.1 \cdot 10^{-4} \text{m}$
			$3 \cdot 10^{-4} \text{m}$	$1 \cdot 10^{-4} \text{m}$
	Al_2O_3	$3.2 \cdot 10^{-3} \text{m}$	$1.4 \cdot 10^{-4} \text{m}$	$.4 \cdot 10^{-4} \text{m}$

Figure 3.11: Relative thickness and thermal diffusion length scales at 1000 Hz for the coating layers and substrate. The substrate thickness shown is for sapphire—the other materials had thicker substrates.



intensity is strongest along the direction of the incident beam, so it's rather difficult to measure it. Instead, I estimate the mirrors' reflectivities from their low-frequency response to the photothermal effect.

Table 3.2: The gold layer has less longitudinal thermal resistance than any other layer, and its transverse conductivity is less than that of the TiO₂ layers. For the thin films, t is taken as the lesser of the layer thickness and r_t at 3000 Hz.

Value	Au film	TiO ₂ film	SiO ₂ film	SiO ₂ substrate	Al ₂ O ₃ substrate
r_t (m) at 3 kHz	8.2×10^{-5}	1.5×10^{-5}	7.1×10^{-6}	7×10^{-6}	2.6×10^{-5}
κ (W/m-K)	317	300	1.4	1.4	40
t (m)	1.8×10^{-7}	1.4×10^{-6}	2.5×10^{-6}	7×10^{-6}	2.6×10^{-5}
$1/2\pi\kappa t$ (K/W) (transverse resistance)	2800	370	4.5×10^5	1.7×10^5	28
$2\pi\kappa t$ (W/K) (transverse conductance)	.00036	.0027	.00002	.00006	.036
t/κ (K m ² /W) (longitudinal resistance)	5.6×10^{-10}	4.6×10^{-9}	3.7×10^{-6}	5×10^{-6}	6.5×10^{-7}

3.2.6.1 Aluminum

The aluminum mirror is a 1" ϕ \times 3/8" block of aluminum, diamond turned on the front surface by Janos Technologies Inc. (www.janostech.com). We do not know exactly what alloy of aluminum was used. The diamond-cutting process leaves the surface reflective, but with visible grooves. Further polishing by CVI Laser Corp. (www.cvilaser.com) attains a uniformly reflective surface of acceptable quality, but with noticeable pits. Care must be taken to protect the reflective surface, which scratches readily from fingers and dust.

The normal-incidence reflectivity of this mirror is 89%. The absorption is around 5%, determined by fitting the DC scale of the photothermal response of the mirror to theory. The balance between absorbed and reflected light is difficult to measure, as the mirror scatters quite a bit of light, most of it along the direction of the incident beam. The back surface is anodized, and presents three #6-32 tapped mounting holes and a central hole used in the manufacturing process. The four holes on the back penetrate about halfway into the mirror.

3.2.6.2 BK7

The BK7 sample with a dielectric stack is a standard flat mirror, part #PR1-1064-99-1037 from CVI. Its substrate is BK7 glass, 1" ϕ \times 3/8" thick. Its front side has a 30-layer, 99% reflective TiO₂/SiO₂

dielectric mirror. Its back side is AR coated. A gold coating was applied to the front surface at Caltech. The normal-incidence reflectivity of this mirror is 95%.

The BK7 sample without a dielectric stack is a protected gold mirror from CVI, part #PG-PM1-1037-C, which has a wedge of a few arcminutes. Its substrate is BK7 glass, 1" \varnothing x 3/8" thick. The normal-incidence reflectivity of this mirror is 96%.

3.2.6.3 Sapphire

The sapphire sample with a dielectric stack is a standard flat mirror, part #PR1-1064-99-PW-1012-SPR from CVI. Its substrate is C-axis sapphire, 1" \varnothing x 1/8" thick. an equivalent substrate, with the same AR coating and dielectric stack as the mirrored BK7 sample. A gold coating was applied to the front surface at Caltech. The normal-incidence reflectivity of this mirror is 97%.

The sapphire sample without a dielectric stack is a C-axis sapphire window, 1" \varnothing x 1/8" thick, part #W1-PW1-1012-SPR-1064-0. It has a an AR coating on its back side, made by CVI. A gold coating was applied to the front surface at Caltech. The normal-incidence reflectivity of this mirror is 97%.

3.2.6.4 Fused silica

The fused silica sample with a dielectric stack is a standard flat mirror, part #PR1-1064-97-PW-1025-UV from CVI. Its substrate is Corning 7980 [34, 35] fused silica, 1" \varnothing x 1/4" thick. Its front side has a 30-layer, $95 \pm 1.5\%$ reflective $\text{TiO}_2/\text{SiO}_2$ dielectric mirror. Its back side is AR coated. It has a protected gold coating on top of its dielectric mirror. The normal-incidence reflectivity of this mirror is 94%.

The fused silica sample without a dielectric stack is a protected gold mirror from CVI, part #PG-PM1-1037-UV, which has a wedge of a few arcminutes. Its substrate is UV grade fused silica, 1" \varnothing x 1/4" thick. It has a protected gold coating on its front surface. The normal-incidence reflectivity of this mirror is 95%.

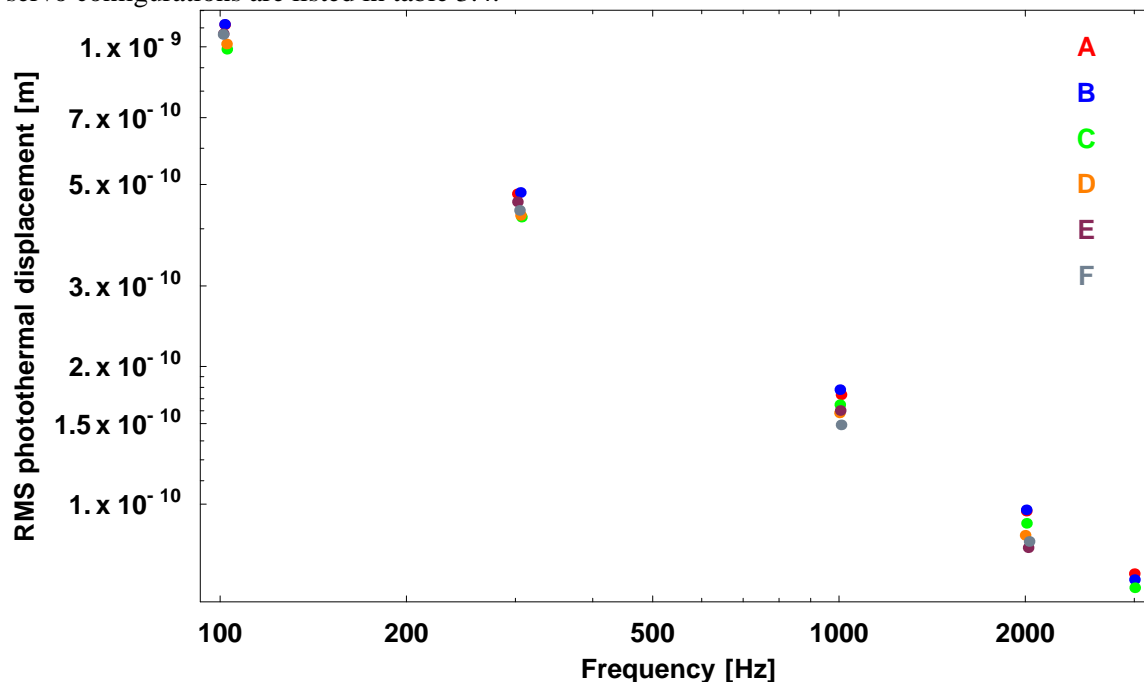
3.2.7 Experimental procedure

3.2.7.1 Configurations

To measure the photothermal effect, the interferometer needs to stay near resonance. The maximum length change Δx that will cause less than a 1% a change in the cavity power is determined by the

condition $\left| \frac{r(1-e^{-i\delta})}{1-r^2e^{-i\delta}} \right|^2 < 0.1$, where $\delta = \frac{2\Delta x}{\lambda}$. For a cavity with a finesse around 100, this is a few nm (Fig. 3.13). This sets the upper limit on the dynamic range for the signal. The practical lower limit on the observable signal is 10^{-11} meters—below this, acoustic noise from the chopper wheel is 2% of the signal magnitude and adds a few degrees of phase to the measurement.

Figure 3.12: Photothermal response of fused silica, for constant *pump* power of 186 mW_{pp}. The servo configurations are listed in table 3.4.



Meanwhile, the magnitude of the photothermal effect varies by a factor 30 between sapphire and metallic aluminum. For each material (Table 3.3), I increased the *pump* power until the rms signal amplitude was greater than 10^{-11} m at the maximum measurement frequency (4 kHz), then I set the servo gain and bandwidth so that the signal amplitude did not exceed the linear range at the minimum frequency (10 Hz). The Al mirror formed a cavity with a finesse of 37, so it had a larger linear range than the other materials.

The *probe* power is limited by the linear range of the RF photodiode (see §3.2.5.2). A neutral density filter in front of the photodiode keeps the power it detects below a mW. This is better than merely reducing the *probe* power, because it's good to have the *probe* beam at the photodiode be more powerful than the cross-coupling fraction of the *pump* beam. A derivation of how cross-coupling noise affects the PDH signal is presented in §5.2 in the appendix.

Figure 3.13: Power transmission coefficient near resonance for a symmetric R=97%, cavity using 1 micron light. To limit power fluctuations to 1%, distance fluctuations need to be less than 4 nm_{pp} .

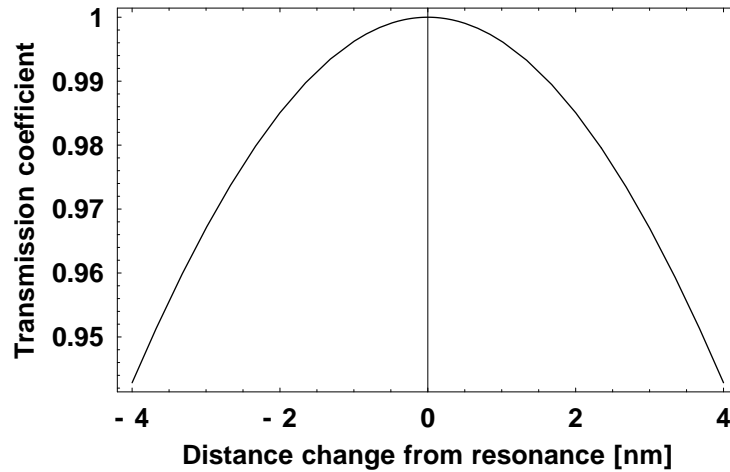


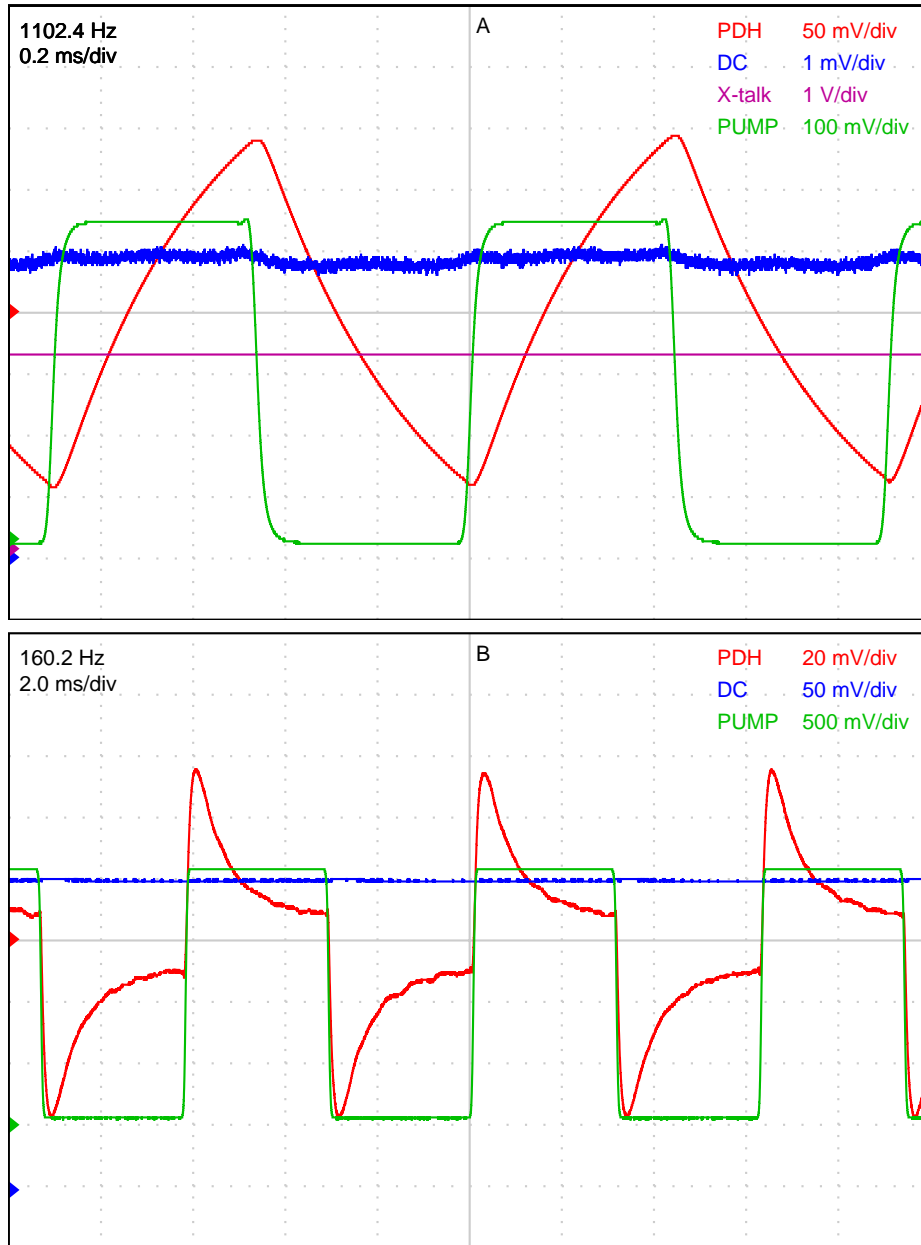
Table 3.3: Optical configurations for each measurement. † Denotes samples with dielectric stacks. Displacements are rms distances measured, above the servo unity gain frequency (UGF). The laser power for the aluminum mirror is unusually high because the cavity visibility was only 50%.

Material	Pump power	Probe power	Finesse	Servo UGF	min. displacement
Aluminum	.122 W	.256 W	37	1000 Hz	3.5×10^{-11} m
Sapphire†	.100 W	.058 W	100	140 Hz	3.5×10^{-11} m
Sapphire	.098 W	.058 W	80	240 Hz	1.9×10^{-11} m
BK7†	.020 W	.056 W	80	360 Hz	1.7×10^{-11} m
BK7	.022 W	.054 W	67	100 Hz	1.5×10^{-11} m
Fused silica†	.176 W	.066W	70	120 Hz	5.3×10^{-11} m
Fused silica	.177 W	.074 W	70	800Hz	3.9×10^{-11} m

3.2.7.2 Data acquisition

For each measurement, a Tektronix TDS3014 digital oscilloscope captures (PDH) the PDH signal, (DC) the RFPDs DC output, (X-talk) the lock-in amplifier's magnitude reading, and (PUMP) the voltage from the photodiode monitoring the chopper. The scope takes 10,000 data points per sample with 8 bits precision, averaging up to 512 samples together by triggering on the rising edge of the chopper monitor photodiode (Fig 3.14). The lock-in amplifier measures the DC port of the RFPD ($\times 50$ for the Aluminum measurement) at the frequency of the chopper's TTL output, and produces from its front panel a voltage proportional to the rms magnitude of the voltage fluctuations. At the end of a data capture, all four waveforms are copied through the serial port to a notebook computer

Figure 3.14: (A) Thermal expansion and cooling of gold-coated sapphire, with a full range of 2.5×10^{-10} m. Red: The filtered PDH signal (8.7×10^{-10} m/V). Blue: RFPD DC voltage shows a small cross-coupling. Purple: rms amplitude of the blue channel, measured with a lock-in amp. Green: chopper-monitor photodiode. (B) Data for the aluminum sample below the servo's unity gain frequency. Thermal diffusion acts quickly to expand or compress the cavity, and the servo acts slowly in the other direction.



separately with the network analyzer (see §3.2.4 for details on correcting for the servo).

3.2.7.3 Computation

Figure 3.15: Intermediate data for gold-coated sapphire. A: PDH voltage magnitude. B: Blue: PDH phase relative to scope trigger point. Red: chopper phase relative to scope trigger point. Black: blue - red.

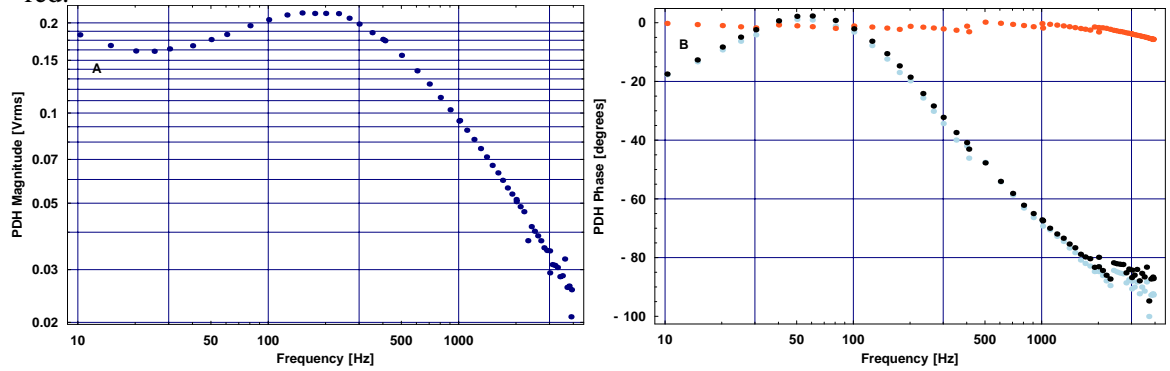
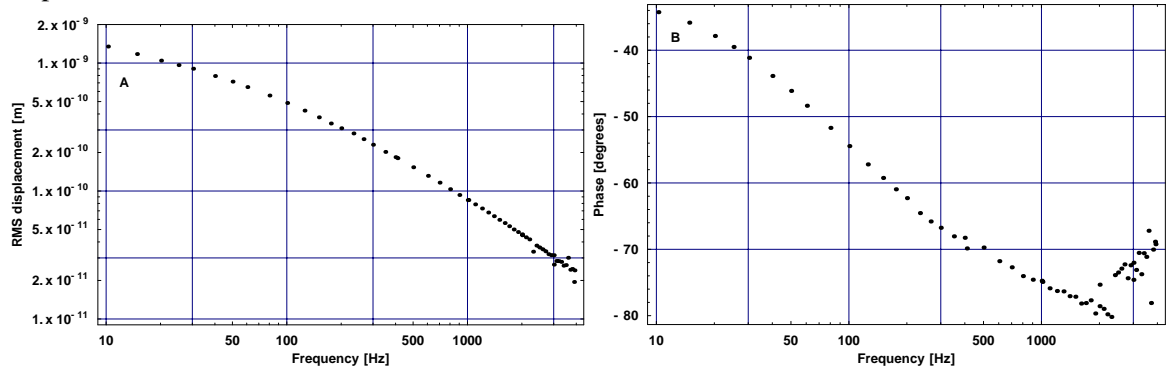


Figure 3.16: Intermediate data for gold-coated sapphire. A: Sample displacement. B: Sample phase response.



Since heat diffusion is a linear system, we can easily analyze it in the frequency domain. At several frequencies between 10 and 4000 Hz, I compute the primary Fourier component of the cavity's frequency response and compare it to the primary component of the *probe* beam's oscillating power.

Taking a time series d_n from a data file, the rms sin and cos components of the waveform at the chopper frequency f are obtained by averaging over an integral number of chopper cycles.

$$s(f) = \sqrt{2} \sum_{n=1}^m (d_n - \langle d \rangle) \sin\left(2\pi \frac{n \times \text{cycles}}{m}\right)$$

$$c(f) = \sqrt{2} \sum_{n=1}^m (d_n - \langle d \rangle) \cos(2\pi \frac{n \times \text{cycles}}{m})$$

The rms amplitude of the displacement is simply $\sqrt{s^2(f) + c^2(f)}$, and its phase relative to the oscilloscope trigger point is $\arctan(c(f)/s(f))$. The rms amplitude of the driving thermal force is $P_0 \frac{\sqrt{2}}{\pi}$, where P_0 is the peak-to-peak amplitude of the square-wave *pump* beam fluctuations.

All the measurements for a sample run are stored in a single data file. The first step in analyzing the data is to calculate the magnitude of the PDH signal (PDH) and its phase relative to the chopper wheel (PUMP) (Fig. 3.15). The chopper frequency f is measured by the scope and saved with the waveform. Next, the data are scaled by the calibration factor, and both magnitude and phase are compensated for the effects of the servo (see §3.2.4) (Fig. 3.16).

3.2.7.4 Scattering

All the test mirrors scatter light, much of which appears to travel in a cone near the reflected beam. An apparatus to measure this is shown in Fig. 3.17. The test mirror is mounted on a rotary stage, and a laser beam is aimed at the mirror. A photodiode, as near to the incident beam as possible and .32 m from the mirror, measures the reflected light power at near-normal incidence. The photodiode response is determined by comparing it to a known 350 mW beam attenuated approximately 100,000 times by neutral density filters. The detector (ThorLabs DET110, [115]) has an area of 13 mm², which subtends a solid angle of $\sim 5.8 \times 10^{-4}$ steradians, or a linear angle of .7°.

Measured data are shown in Fig. 3.18 for the gold-coated plain sapphire substrate, with the power measured by the photodiode plotted against the rotation angle of the test mirror (see Fig. 3.17). The reflection off the mirror shows an asymmetric distribution of scattered light. To estimate the total scattered power, I convert the measured power at an angle θ to a power density on an annulus of diameter $\sin \theta$. Using a linear interpolation between these points, the integrated power is calculated to be ~ 2 mW.

3.2.7.5 Power absorption

Comparing the data to models requires an estimate of the power absorbed by the test mirror, P_{abs} . This, in turn, depends on the *pump* light power, the coupling of the *pump* beam to the cavity, and the absorptivity of the sample. Of these three quantities, the latter must be inferred from the data.

Conservation of energy requires that the light power incident on the cavity be either reflected,

Figure 3.17: Measuring scattering from a test mirror. The beam, at angle 0, is $\sim 1^\circ$ wide.

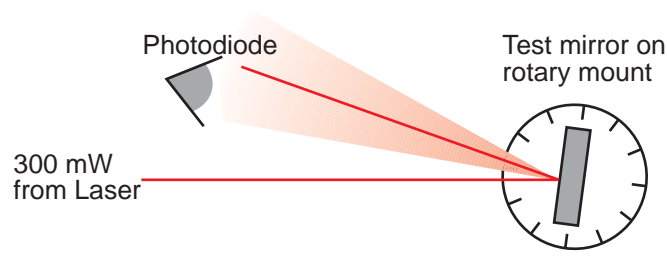
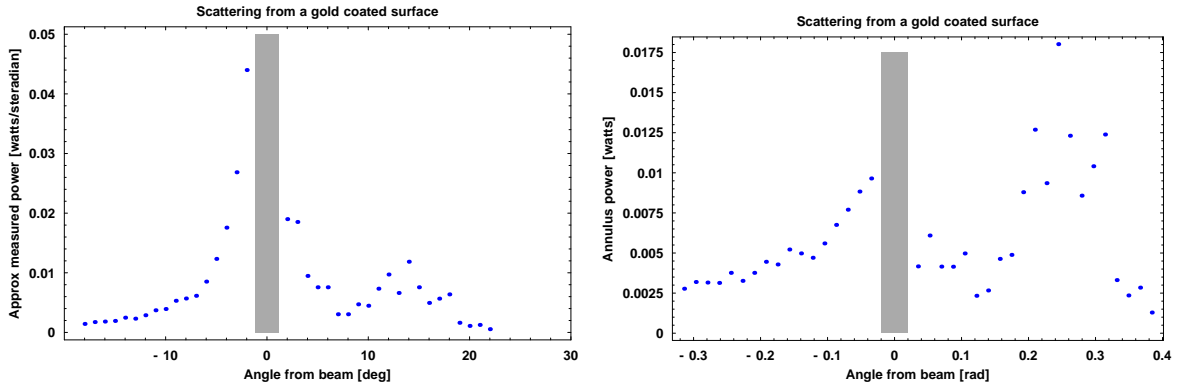


Figure 3.18: Measuring scattering from a gold-coated sapphire mirror. The gray bars show the angles near the reflected beam. Left: scattered power per steradian as a function of angle from the reflected beam center. Right: scattered power per radian for a circular annulus, as a function of angle from the reflected beam center.



scattered, or absorbed.

$$P_{reflected} + P_{abs} + P_{scattered} = P_{pump} \quad (3.3)$$

Two of these terms are known: P_{pump} is measured with a power meter, and the ratio $P_{reflected}/P_{pump}$ is found by sweeping the laser frequency slowly through resonance and measuring the power in the reflected beam. Note that $P_{reflected}$ is the reflection from the cavity, not from the sample mirror. This determines the cavity's visibility, the fraction of power that is not reflected. Neglecting losses at the cavity input mirror and from absorption by air, this can only be accounted for by absorption or scattering off the sample mirror.

$$visibility = \frac{P_{abs} + P_{scattered}}{P_{pump}} = 1 - \frac{P_{reflected}}{P_{pump}} \quad (3.4)$$

The reflectivity of the sample mirror is measured outside of the interferometer. Knowing the sample reflectivity R , where $R < 1$, the sum of the sample's absorption and scattering coefficients, A and S , is determined by $A + S = 1 - R$. Assuming the cavity's scattering and absorption occurs only at the sample mirror, we can define P_0 as the power incident on the sample.

$$P_{abs} = P_0 A \quad (3.5)$$

$$P_{scattered} = P_0 S \quad (3.6)$$

Combining this with Eq. 3.4, we get the equation

$$visibility \times P_{pump} = P_0 A + P_0 S \quad (3.7)$$

By solving for P_{abs} , we can express the power absorbed by the mirror in terms of the unknown absorptivity coefficient A and other, known quantities.

$$P_{abs} = visibility \times P_{pump} \times \frac{A}{1 - R} \quad (3.8)$$

In plotting a model against the data, A is free parameter constrained to be less than $1 - R$.

3.2.7.6 Systematic errors

As you can see in Fig. 3.14, the precise locations of the chopper transitions are somewhat ambiguous. The beam radius at the chopper is .13 mm at the chopper, and the gaps in the fast wheel are only 8 mm wide. I calculate the systematic phase error as one-half the difference between the positive and negative duty cycles of the PUMP signal. The algorithm to determine this measures the elapsed times for one full cycle between the positive-going and negative-going edges at the mean value of the waveform. This is about 4° for the fast chopper wheel and 1° for the slower one. Error bars based on the measured phase error are plotted in the Results section.

The major known systematic error in the magnitude is cross-coupling noise, which depends on the amount of *pump* light reflected from the cavity that reaches the RFPD. The RF and DC components of the PDH signal both depend on a random phase ϕ and the crosstalk factor, ζ , where

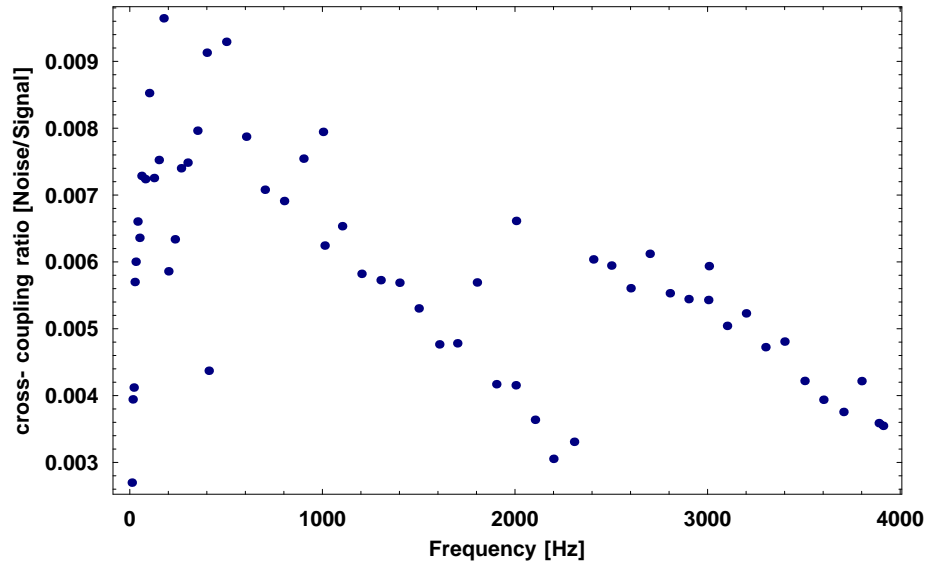
ζ^2 is the fraction of *pump* light which reaches the RFPD. The unknown phase shift ϕ reflects the path difference between the *pump* and *probe* paths, and varies with thermal expansion of the optics table and the optics mounting hardware.

$$P_{RF} \propto 2\sqrt{P_S}(\sqrt{P_C} + \zeta\sqrt{P_F} \cos \phi) \quad (3.9)$$

$$P_{DC} \propto (\zeta^2 P_F + P_C + 2\zeta\sqrt{P_F P_C} \cos \phi) \quad (3.10)$$

where P_S and P_C are the *probe* beam sideband and carrier powers, and P_F is the *pump* beam power (see §5.2). Since $P_C \gg P_F$ at the RF photodiode and $\zeta \ll 1$, the ζ^2 can be neglected, and the fractional measurement error in the PDH signal is proportional to $\zeta \cos \phi \sqrt{P_F/P_C}$, and fractional variation in the voltage measured by the RFPD is $2\zeta \cos \phi \sqrt{P_F/P_C}$. We can monitor the latter by hooking up the RFPD's DC output ($\langle V \rangle$) to a lock-in amplifier, triggered off the chopper. The lock-in amplifier measures the rms amplitude of the fundamental mode of the variations (V_{rms}), which are recorded by the oscilloscope. The cross-coupling factor (noise/signal ratio) is computed as $V_{rms}/\langle V \rangle$. This factor was measured for every data point, and is usually less than 1% (Fig. 3.19). The interferometer input mirror is slightly birefringent, so ζ varies if the cavity strays far from the center of its resonance. To combat this, operator intervention is effective at regulating the laser and cavity temperatures on sub-Hz timescales.

Figure 3.19: Cross-coupling noise ratio for gold-coated sapphire.



The calibration process depends on fitting the measured OLTF to a model of the servo, and this process can introduce error due to noise in the measured transfer functions. To estimate this uncertainty, I repeated a measurement several times with different servos, *probe* powers, sideband modulation depths, and attenuation factors at the RFPD. Labelled A-F, they are listed in table 3.4 and the data are plotted in Fig. 3.12. Runs A-D used the *probe* beam at full power (70 mW), with sideband modulation depth at its typical level (3% power in each sideband) and a 1/100 attenuator at the RFPD. Runs E-F used the *probe* beam at half power (36 mW), with sideband modulation depth at 1/10 of its typical level and only a 1/10 attenuator at the RFPD. The D, E, and F runs are missing points at 3 kHz because of errors in transferring data from the oscilloscope to the computer.

The spread in these data suggests that the imprecision of the calibration process is about 10-15%, likely due to errors in measuring the servo transfer function, which sets the overall calibration of the instrument.

Table 3.4: Six servo configurations for measuring the response of dielectric-coated fused silica, for constant *pump* power of 186 mW_{*pp*}.

Label	<i>Probe</i> power mW	Servo UGF kHz	Servo DC Gain	100Hz displacement 10^{-9}m_{rms}	2kHz displacement 10^{-11}m_{rms}
A	70	1	30	1.12	9.65
B	70	2.6	75	1.12	9.72
C	70	23.8	83	.99	9.08
D	70	5.6	15	1.01	8.55
E	36	1.8	61	1.07	8.03
F	36	.44	16	1.06	8.29

3.3 Results

The data analysis process produces a set of complex numbers corresponding to the magnitude and phase of each sample's displacement, which can be compared to the theoretical model described by Cerdonio *et al.* [32]. The frequency response this predicts for the average displacement $D(f)$ of the mirror surface is given by the equations

$$D(f) = \frac{\sqrt{2}\alpha(1+\sigma)P_{abs}}{\pi\kappa} \times \frac{1}{\pi} \int_0^\infty du \int_{-\infty}^\infty dv \left[\frac{u^2 e^{-u^2/2}}{(u^2+v^2)(u^2+v^2+if/f_c)} \right] \quad (3.11)$$

$$f_c = \frac{\kappa}{2\pi r_0^2 \rho C_p}$$

The first part of Eq. 3.11 determines the scale of the mirror displacements and depends on P_{abs} , the rms power absorbed by the mirror. The second part, under the integral signs, determines the frequency dependence of $D(f)$. In the limit of high frequencies, this approaches the Braginsky, Gorodetsky, and Vyatchanin (BGV) equation [22].

$$D_2(f) = \frac{\sqrt{2}\alpha(1+\sigma)}{\pi} \frac{P_{abs}(f)}{(\rho C_V \pi r_0^2) i f} \quad (3.12)$$

This equation has a constant phase of -90° , while the phase of Eq. 3.11 varies from zero at DC to -90° at high frequencies.

After applying the calibration and compensating for the servo, as described in §3.2.7.3, the data describe the root-mean-square (rms) amplitude of the fundamental component of the measured displacement. Meanwhile, the *pump* beam power is measured as the peak-to-peak (pp) range of a square wave. The rms amplitude of the fundamental mode of a square-wave signal can be deduced from the Fourier decomposition of a square wave H_{sq} with a peak-to-peak range of B .

$$H_{sq} = \sum_{\text{odd } n=1}^{\infty} \frac{2B}{n\pi} \sin n\omega t \quad (3.13)$$

The rms amplitude of a sine wave is $1/\sqrt{2}$ of its peak amplitude, so we obtain the following conversion formula:

$$V_{rms}^{sine} = V_{pp}^{square} \frac{\sqrt{2}}{\pi} \quad (3.14)$$

The various sample materials were tested under different conditions, with different laser powers, interferometer visibility, and coating reflectances. Fortunately, the circumstances were similar between samples with the same substrate. Table 3.5 summarizes these configurations, and the following sections discuss the results for each of the materials examined.

Table 3.5: Conditions for photothermal measurements. † Denotes samples with dielectric stacks. The A values are the absorptivities obtained from fitting the predicted substrate response to the data.

Sample	Coating type	Pump power (mW _{pp})	visibility (%)	R (%)	A (%)
Aluminum	plain	122	49	89	6.5
Sapphire†	Au	100	72	97	1.5
Sapphire	Au	98	72	97	1.5
BK7†	Au	20	86	97	
BK7	protected Au	22	87	96	2.6
Fused silica†	protected Au	176	82	94	
Fused silica	protected Au	177	91	95	

3.3.1 Aluminum

The aluminum mirror was chosen to debug the instrument because of its large thermal expansion coefficient. We expected to find its photothermal response closely following Eq. 3.11, but the frequency dependence of the data was different than predicted for Al 6061-T6⁹. The data are plotted in Fig. 3.20, along with the model, where the absorptivity was fit to the data. The dashed line in the magnitude plot is Eq. 3.11 uses the parameters for Al 6061-T6 listed in table 2.3.

This alloy of aluminum is known to change its properties with working [3], so the polishing and anodizing it received during its manufacture may have affected its thermal properties. If thermal conductivity is allowed to vary as a fit parameter, we get the solid black line in Fig. 3.20, which agrees well with both the measured magnitude and phase.

To make this fit, I replaced the factor κ/r_0^2 in f_c with $a\kappa/r_0^2$ computed Eq. 3.11 for a range of

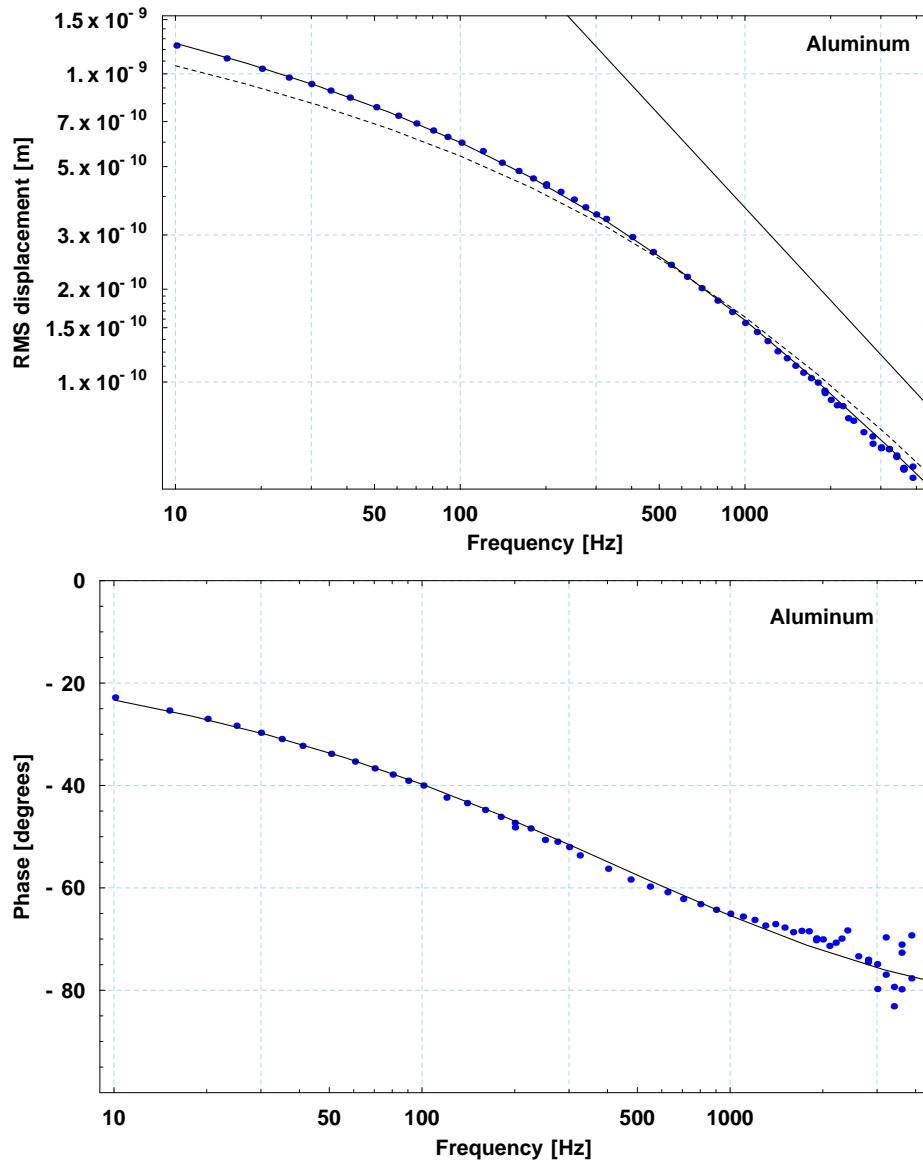
⁹Alloy number 6061, temper number 6

values of a at the each of the frequencies at which I had data points. Interpolating between these calculated values for the model gives a best fit value of a of 0.67. If this were due entirely to a change in thermal conductivity, that would be surprisingly low, but not impossible for an aluminum alloy ¹⁰. This factor could also be caused by a higher heat capacity than usual or a larger laser spot than expected.

The straight solid line in the magnitude plot of Fig. 3.20 shows the BGV equation (Eq. 3.12), which has a $1/f$ dependence.

¹⁰Alloy 5456 has a thermal conductivity around 120 W/m-K [113]. The Aluminum Association has this to say about its published tables of materials data: “The following typical properties are not guaranteed since in most cases they are averages for various sizes, product forms, and methods of manufacture and may not be exactly representative of any particular product or size. These data are intended only as a basis for comparing alloys and tempers and should not be specified as engineering requirements or used for design purposes” [113]

Figure 3.20: Photothermal displacement magnitude and phase for aluminum. The solid line fit to the data in the magnitude and phase plots shows the photothermal effect, with the ratio κ/r_0^2 fit to the data in addition to the mirror absorption. The dashed line shows the predicted response based on material parameters in table 2.3, fit only to the mirror absorption. The straight line is the BGV formula, which sets the upper frequency limit



3.3.2 Sapphire

Sapphire is a much more standard material than aluminum, and is thus better for demonstrating this instrument. There are two sapphire samples, one with and one without a 99% reflective dielectric stack, both covered with 97% reflective layers of pure gold, 180 nm thick. We expect the sample without a stack to follow the Cerdonio *et al.* formula, Eq. 3.12 without adjusting any of the material parameters.

The sample with the stack should have a response like that of the substrate, plus an additional contribution from the coating. The coating response function derived in §2.4.2.1 is repeated here.

$$D_c(f) = \frac{\alpha_{layer} \tilde{P}(\omega)}{\rho C_v \pi r_0^2 i \omega} \left(1 - e^{-d \sqrt{i \omega / a^2}}\right)^2 \quad (3.15)$$

Fig. 3.21 shows the measured displacement magnitude and phase for sapphire, with (blue) and without (orange) dielectric stacks. The solid line through the orange points is the model of the substrate, fit only to the mirror absorption, and using the material properties listed in table 2.3. The solid line through the blue points is the model of the substrate using the same parameters as the other line, plus the coating. The best fit for the mirror absorption is 1.5% for both curves, and the coating thermal expansion fit gives $\alpha_{layer} = 24 \times 10^{-6}/\text{K}$.

The “upper limit” lines show the BGV model of the photothermal effect, using the substrate and coating material properties. The former is the asymptotic limit for the substrate, the latter is the asymptotic limit for the coating itself. The “dielectric stack” line shows the magnitude of $D_c(f)$, the model for the coating response. We expect the response of the dielectric stack to converge to the “coating upper limit” line somewhere above 10 kHz, where the thermal diffusion length in the coating becomes much less than its thickness.

Both samples agree well with the Cerdonio *et al.* theory (Eq. 3.11) below 100 Hz, while the sample with a dielectric stack shows a discernable additional expansion above 500 Hz. At 1 kHz, the coating thickness is about 30% of its thermal diffusion length, and it increases the photothermal expansion by around 10% over the substrate expansion. The model for the expansion of the substrate with a coating is not in perfect agreement with data, but it comes very close to the measured magnitude response and within a few degrees of the phase. The phase response of the substrate deviates from the model when the signal strength is around 3×10^{-11} m, which may be due to

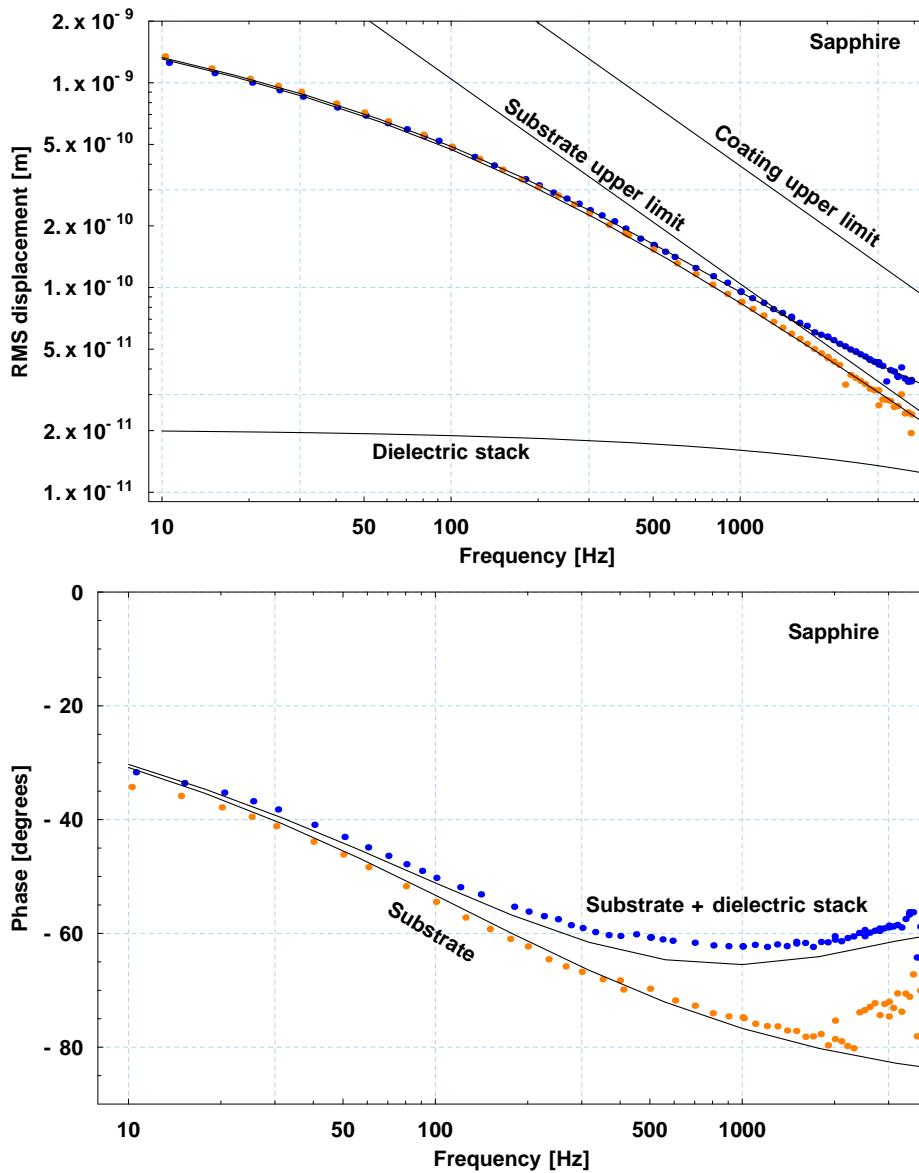
acoustic noise or mechanical resonances in the interferometer spacer hardware.

In calculating the model for the coating, the coating is assumed to be a homogenous layer, with its thermal properties averaged from its constituents, SiO₂ and TiO₂. The coating's effective thermal conductivity is 2 W/m-K, obtained from Eq. 2.3, where d_1 and d_2 are the lumped thicknesses of the coating layers. The average density is taken to be 3000 kg/m³, and heat capacity to be 700 J/kg-K. Thin TiO₂ thin films, which make up 40% of the coating thickness, have been reported to have a thermal expansion coefficient of $50 \times 10^{-6}/\text{K}$ [56], and the SiO₂ layers are believed to have a thermal expansion coefficient around $1 \times 10^{-6}/\text{K}$ [127]. Combining these as a weighted average, the expected value of α_{layer} is $20 \times 10^{-6}/\text{K}$. The expansion is clearly dominated by the TiO₂ layers, whose expansion is much greater than that of SiO₂¹¹. These expected parameters should of course be treated with a grain of salt, since we can't peel off the coatings, dissect them, and measure their layers independently.

The observed data do not rule out the possibility that stress effects enhance the thermal expansion. Notably, the data are not consistent with Eq. 2.43, or any similar theory with a displacement response proportional to $1/\sqrt{f}$.

¹¹The generally accepted value for the thermal expansion of SiO₂ is $0.5 \times 10^{-6}/\text{K}$, but higher values have been found in non-thermally grown films [5, 20, 30, 127]

Figure 3.21: Photothermal displacement magnitude and phase for sapphire, with (blue) and without (orange) dielectric stacks. The orange points are compared to a model of the substrate, fit only to the mirror absorption. The blue points are plotted against the same substrate model plus a fit to the coating (plotted separately as the “dielectric stack” line). The mirror absorption is taken to be 1.5% for both curves, and the coating thermal expansion fit gives $\alpha_{layer} = 24 \times 10^{-6}/\text{K}$. The “upper limit” lines are the BGV model, using the substrate and coating material properties.



3.3.3 BK7

The BK7 samples have the greatest photothermal response, and the sample with the 99% reflective dielectric stack expands more than the substrate. The sample with the dielectric stack was given a gold coating at Caltech at the same time as the sapphire samples, and the sample without the dielectric stack is a commercially available protected gold mirror.

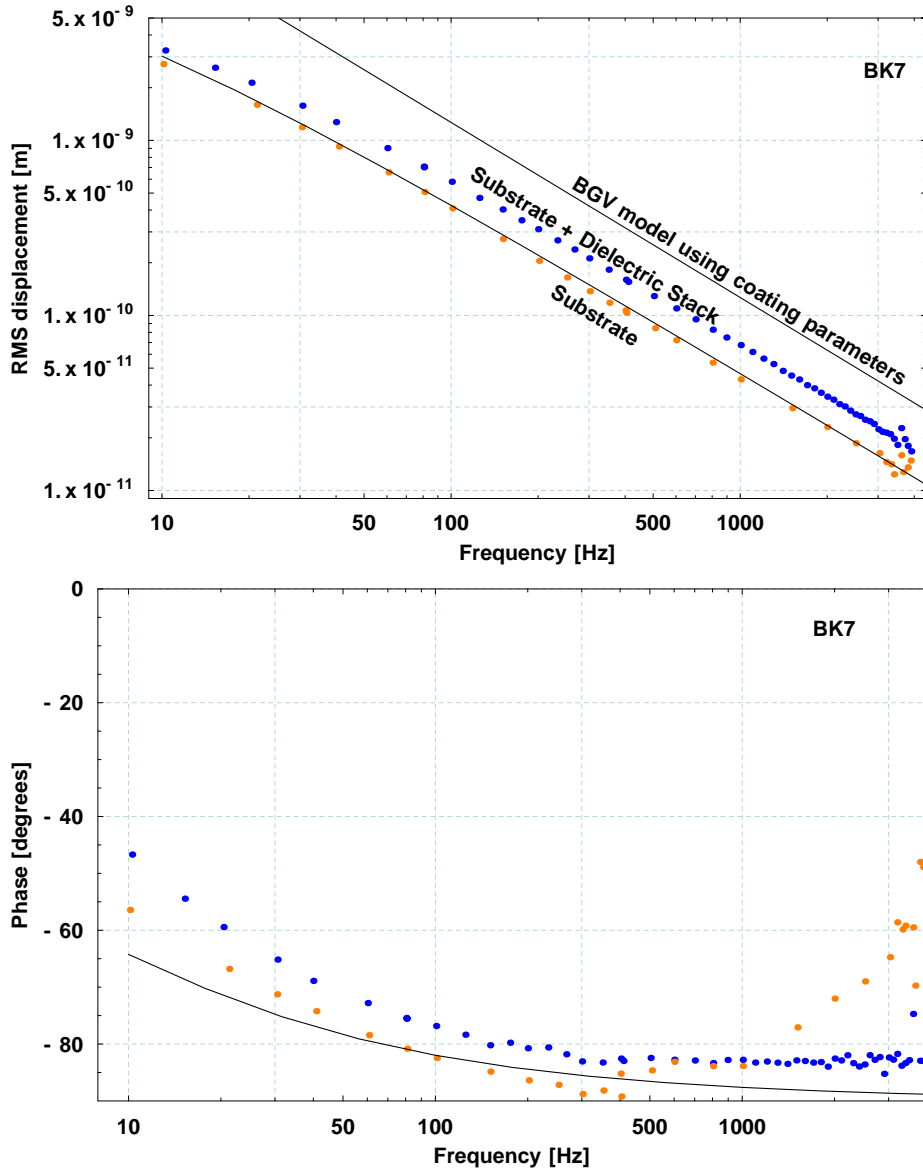
Fig. 3.22 shows the measured displacement magnitude and phase for BK7, with (blue) and without (orange) dielectric stacks. The solid line through the orange points is the model of the substrate, fit only to the mirror absorption, and using the material properties listed in table 2.3. The phase of this model is plotted against the phase data. The best fit for the mirror absorptivity is 2.6% for the sample without the dielectric stack.

The sample with the dielectric stack (blue) shows considerably more expansion than does the substrate. The upper line in the magnitude plot shows the BGV limit of the photothermal effect, using the same average coating parameters as for the sapphire plots¹². The response of this sample is inconsistent with Eq. 2.45 derived in Chapter 2, which predicted a $1/\sqrt{f}$ spectrum for the coating's contribution to thermal expansion. This theory is based on calculating the temperature profile in a homogenous media, and then computing the average fluctuation in a zone near the surface. If we evaluate the model derived for the sapphire substrate, Eq. 3.15, we get a magnitude for the coating expansion of less than 10^{-11} m, so the assumptions used to derive that model clearly do not apply to this situation.

Instead, these data could be interpreted as observations of part of a gradual transition from a low frequency range (~ 10 Hz) where the substrate dominates to a high-frequency range (> 10 kHz) where the coating response dominates.

¹²The laser power was different between the BK7 and sapphire measurements

Figure 3.22: Photothermal displacement magnitude and phase for BK7, with (blue) and without (orange) dielectric stacks. The upper solid line in the magnitude plot is the BGV model, using the coating's average thermal properties. The lower solid line is a model of the substrate's photothermal response.



3.3.4 Fused silica

Both fused silica samples have Corning 7980 [35] substrates, and were manufactured by CVI Laser. One sample has a 95% reflective dielectric stack on top of the substrate, and both are covered with commercial protected gold coatings.

Fig. 3.23 shows the measured displacement magnitude and phase for fused silica, with (blue) and without (orange) dielectric stacks. The solid line below the orange points in the magnitude and phase plots is the model of the substrate, assuming the mirror absorptivity to be 4% and using the material properties listed in table 2.3. The upper line in the magnitude plot shows the BGV limit of the photothermal effect, using the same average coating parameters as for the sapphire plots.

The data for the fused silica samples present a surprise, since their measured magnitude response is a few times greater than expected. Repeated measurements of the fused silica samples with varying *pump* and *probe* beam powers show that the signal is linear with respect to the *pump* power, and it does not scale with the *probe* power. This suggests that the extra thermal expansion is a linear effect, correlated with the power absorbed by the fused silica mirror.

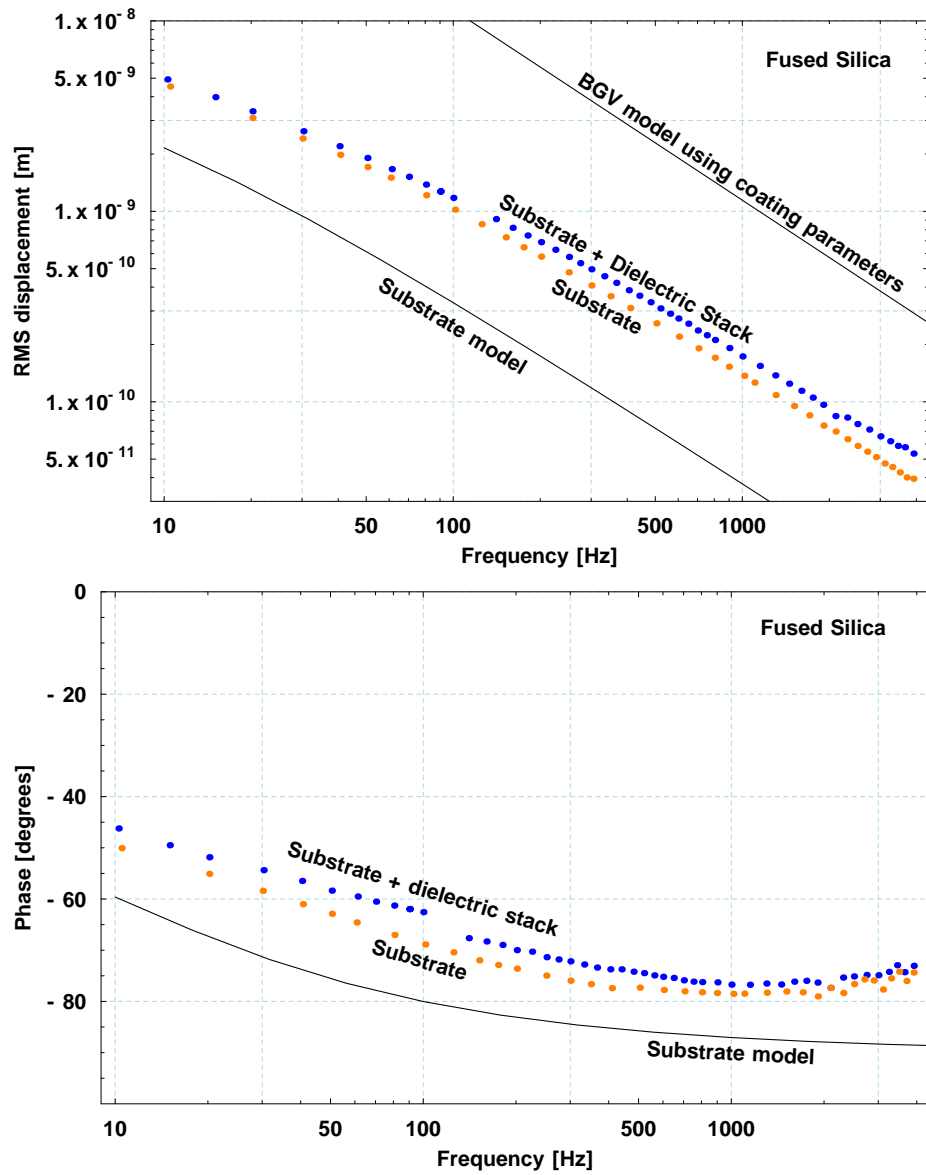
A possible cause for the unusually high readings in fused silica could be the “protected gold” layer, since light in the interferometer has to pass twice through a clear protective coating on top of the gold. If the protective coating had a large, negative dn/dT coefficient, this could account for some of the excess expansion of the samples. The optical path length change due to the protective layer is $\Delta L = 2 \times nd(\alpha + \beta)\Delta T$, where $\beta = dn/dT$. If the temperature change is 10 K, β is -10^{-5} and the layer’s optical thickness is $nd \sim 10^{-6}$ m, heating of the layer could affect the cavity’s measured length by around 2×10^{-10} m. Unfortunately, the protective coating is a trade secret [34] and measurements of its properties are not available to us, but -10^{-5} is not an unreasonable value for β for some materials [49]. A useful experiment would be to repeat these measurements on samples coated with bare gold.

It is unlikely that scattered light expanding and contracting the interferometer hardware would account for the excess signal. Expansion of the spacer block has the wrong sign, expanding the cavity when the mirror’s expansion would shorten it. The phase of the fused silica data would be different by 180° if this effect exceeded the substrate’s thermal expansion. Also, the procedures and software algorithms used to compute and analyze the fused silica data are identical to those used on the sapphire and BK7 samples.

As with the BK7 samples, the sample with the dielectric coating expands more than the one

without, and this difference increases with frequency.

Figure 3.23: Length and phase response of fused silica mirrors, with (blue) and without (orange) dielectric stacks. The model lines is based on absorbed power of 4%.



3.3.5 Summary

The purpose of this experiment is to test our understanding of the photothermal effect in dielectric-coated mirrors. A secondary goal is to set bounds on the thermal expansion coefficient of a mirror coating. While methods exist for measuring the thermal expansion of thin films [66, 118], there is very little work on entire dielectric stacks. The dielectric coating measurements by Braginsky and Samoilenko use the bending beam method [25], and depend on accurate values of the coating's Young's modulus. The method developed in this thesis allows a direct measurement of a mirror's thermal expansion as it would be detected by a Gaussian laser beam. By varying the *pump* beam power, this technique is able to measure behaviors that span more than 2 orders of magnitude in surface displacement and 3 orders of magnitude in frequency.

Being able to vary the *pump* power by an order of magnitude also helps inspire confidence that these experiments measure linear effects. The photothermal transfer functions for these materials, which has units of displacement per unit power absorbed, are plotted in Fig. 3.24. These curves are obtained by dividing the measured data described above by the rms power absorbed by the sample without a dielectric stack, as determined by fitting the model for the substrate expansion to the data. In the case of the fused silica data, a mirror absorptivity of 4% is assumed for this normalization.

Of these materials, the photothermal effect is the smallest for fused silica, even with its unexpectedly high measured response. To demonstrate the linearity of fused silica in these experiments, Fig. 3.24 shows two overlapping curves for the fused silica sample without a dielectric stack, taken during different months and with different *pump* beam powers.

In all of these materials, a dielectric stack makes a significant contribution to the photothermal response of a mirror. To visualize the coating's effect, Fig. 3.25 compares the ratio of photothermal displacement of samples with dielectric stacks to those without. This plot is obtained by generating two functions, $g_c(f)$ and $g_s(f)$, which are linear interpolations of the magnitude data for the samples with and without dielectric coatings, respectively. The ratio $r = \gamma g_c(f)/g_s(f)$ is plotted, with γ chosen to normalize r to 1 at 25 Hz.

The effect of the coating is most notable in sapphire, even though all three data sets compare samples with similar dielectric stacks. From this, I conclude that the choice of substrate material affects the coating photoelastic effect, and that further theoretical work is indicated to understand how.

Figure 3.24: Normalized response (displacement divided by *pump* beam power) of BK7, sapphire, and fused silica for a .2mm spot radius (1/e power). The fused silica data are higher than expected. The dark lines on top are the samples with dielectric stacks; the lighter lines on the bottom are the samples without dielectric stacks. Of the lower fused silica substrate data, the light dashed line was taken with *pump* power 19 mW, and the sold line with *pump* power 174 mW.

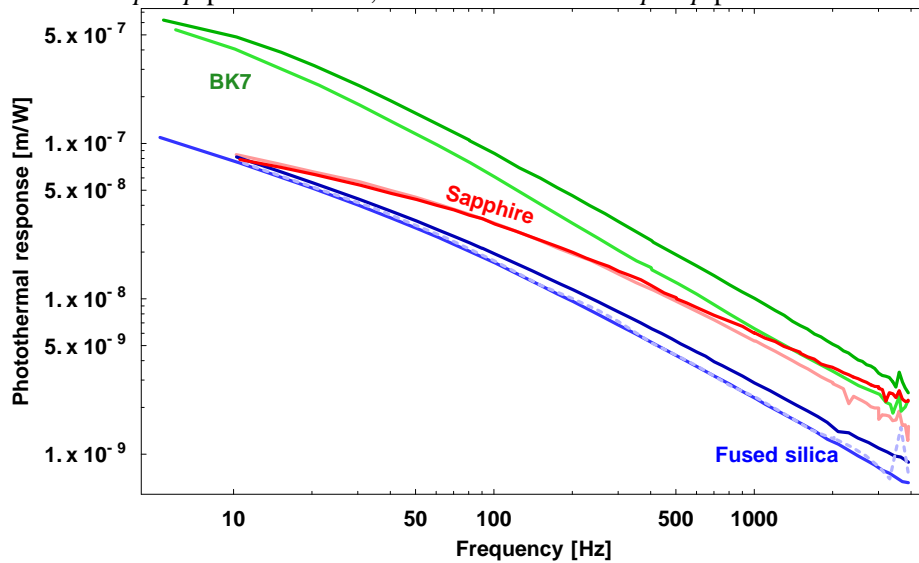
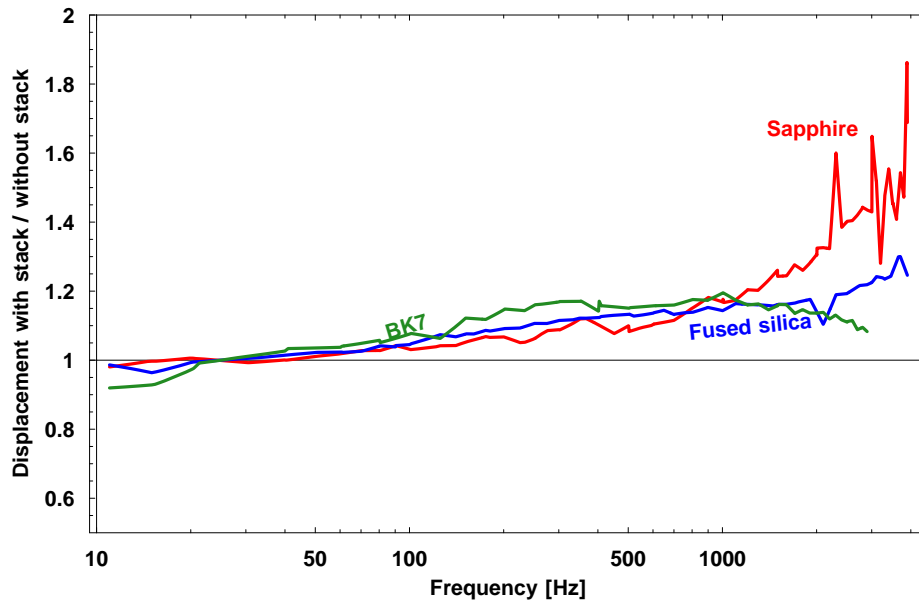


Figure 3.25: Ratio of photothermal displacement of samples with dielectric stacks to those without, normalized to 1 at 25 Hz. The ratios are based on linear interpolation between the measured data points, which are not always at the same frequencies. The data for BK7 are omitted above 3 kHz.



Chapter 4

The Thermal Noise Interferometer

4.1 Introduction

The purpose of the Thermal Noise Interferometer (TNI) project is to build a low-noise interferometer capable of determining the fundamental noise sources that would limit LIGO's sensitivity. Using materials and designs from LIGO, the TNI can be used to measure the noise in test mass mirrors, suspension systems, and control electronics. It is one of the more sensitive displacement measuring devices on Earth, with an rms length noise of 5×10^{-18} m/rHz at 1kHz.

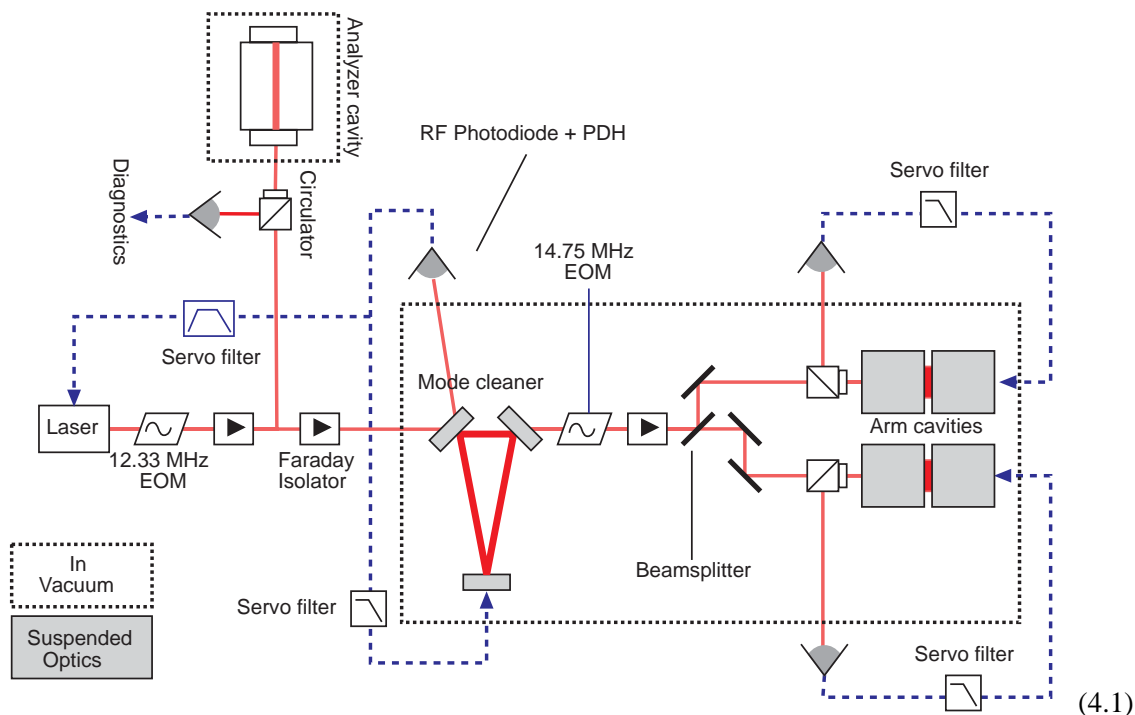
This chapter describes the steps necessary to build and operate an instrument like the TNI.

4.2 Design

The design of the TNI is modelled after that of LIGO. A schematic of the major components is shown in Fig. 4.1. The TNI has two arm cavities made from suspended, high-Q mirrors under vacuum, and data are taken as the difference between the signals from the two arms. To optimize the TNI for detecting thermal noise instead of gravitational waves, its arms are very short (8.5 mm) and the laser spot is very small (.15 mm). The arms are adjacent and parallel, so that seismic vibrations affect them equally. As in LIGO, the mirrors are supported only by a wire sling, so they move with minimal friction. A triangular, suspended cavity in the vacuum chamber provides a frequency reference for the laser and acts as a mode cleaner, without creating any spurious interferometers. Also like in LIGO, the Pound-Drever-Hall (PDH) [43, 41] method is used for sensing cavity length and laser frequency changes.

The in-vacuum optics are all mounted on a seismic isolation stack [52, 50], and the interferometer mirrors are further removed from ground noise by 1-Hz pendulum suspensions. The suspended

Figure 4.1: Conceptual design of the TNI, showing the major optics and servos.



mirrors have local damping servos to reduce the pendulum Q , but the servos roll off strongly above 20 Hz so that the mirrors are essentially free masses above 300 Hz.

Three control servos are needed to keep all the interferometers resonant simultaneously. The mode cleaner is locked to the laser at low frequencies, but the laser is locked to the mode cleaner at high frequencies. The two arm cavities are independently locked so as to not have any common-mode electronic coupling.

4.2.1 Optics

The central component of the TNI (Fig. 4.2) is the laser, a 500 mW, 1064 nm diode-pumped Nd:YAG non-planar ring oscillator (LightWave Electronics Model 126), similar to the one described in the previous chapter. The beam emanating from the laser is only slightly elliptical, so a pre-mode cleaner is not needed as with LIGO.

Immediately after the laser, a tuned electro-optic modulator (EOM) (1) (New Focus #4003) applies 12.33 MHz RF sidebands. The modulation depth is weak ($< 0.1\%$) to minimize the beat with the arm cavity sidebands. The EOM is misaligned to the beam by a few degrees, so that

reflected light does not feed back to the laser crystal. A Faraday Isolator (2) and half wave plate (3) follow the EOM to prevent back-reflections from downstream optics. A lens (4) refocuses the beam as it passes through another Faraday Isolator (6). A beamsplitter (5) diverts 10% of the beam power for measuring the laser frequency noise with an independent cavity.

In the main beam, a wave plate (7) sets the beam into vertical polarization (though horizontal may also be used) for the mode cleaner (see §4.2.2), and steering mirrors (8) maneuver the beam into position for the periscope (9). At the top end of the periscope, a mode-matching mirror (10) images the beam waist for the mode cleaner. This mirror is mounted on a steel pedestal which is clamped to the underside of an elevated platform. The steering mirror at the top of the periscope (also clamped to this platform) directs the beam through a window and into the vacuum chamber, where mirrors line it up with a periscope (11). The top mirror of this periscope and another steering mirror (12) align the beam to the mode cleaner, made from three suspended mirrors (13, 14, 15). The rejected beam from the mode cleaner is pointed (16) back through the window and onto the main table, where steering mirrors (17) lead it to the mode cleaner photodiode (18).

The beam transmitted by the mode cleaner wraps around the back of the table, passing through a mode-matching lens (19) which images a waist at the 14.75 MHz EOM (23). A $R \sim 99\%$ steering mirror (20) transmits a fraction of this beam, which is lowered by another periscope (21) and sent through a window to a TV camera (22). The TV camera shows which mode is resonant in the cavity.

After the EOM (23), the beam transmitted by the mode cleaner turns (24) toward the arm cavities and passes through another Faraday Isolator (25). The magnetic field from this isolator affects all the suspended mirrors, so they have to be aligned after the isolator position is fixed. After the isolator, a half wave plate (26) sets the beam in horizontal polarization for the arm cavities. A mode-matching lens (27) images the arm cavity beam waists, and the beam is turned (28) at a point equidistant from both cavities.

A 50% P-polarization beam splitter (29) separates the beam to the North and South arms. The alignment to the North arm (32) is controlled by adjusting the beamsplitter and a steering mirror (30), so it has to be aligned before the South arm. The transmitted beam is lowered (33) and imaged onto a camera (22) on the monitoring table outside the vacuum. Immediately before the cavity, a circulator diverts the reflected beam from the North arm around the table to a periscope (35, 36) and back to the main optics table (37), where a periscope (38) directs the beam to a RF photodiode [86, 112] (40). A large, fast cat's eye lens (39) focuses the beam onto the photodiode so that the detected light power is not affected by beam jitter.

The beam transmitted by the beam splitter (29) is aligned with a pair of steering mirrors (41) to the South arm (42). The transmitted beam is also directed out of the chamber (44, 45) through the side window to a video camera to monitor the cavity mode. The beam reflected from the cavity is diverted by a circulator (43) and steering mirrors (46, 47, 48) to the main optics table. There, as with the other arm, a periscope (49) and cat's eye lens (50) focus the beam onto the RF photodiode (51).

4.2.2 Mode cleaner

The triangular mode cleaner uses 3"Ø × 1" mirrors in LIGO-like small-optic suspensions. The input and output mirrors (13, 14) are flat, superpolished, with T=300 ppm 45° HR coatings on the front surfaces, and AR coatings on the back surfaces. They have a half-degree wedge, oriented so that the wide edge is up. This arrangement makes the pitch, yaw, and Z modes of the pendulum have resonant frequencies all around 1 Hz. The back mirror is a 3"Ø × 1" superpolished plano-concave mirror with a 5 m radius of curvature. Its front side has a T=30 ppm normal incidence HR coating, and the back side is AR coated. Polishing and coating were done by Research Electro-Optics (REO) in Boulder, CO.

A local damping system prevents the mode cleaner mirrors from swinging around at low frequencies. Magnets and fins are glued to the back of the mirror (Fig. 4.3), which fit into an Optical Sensor / Magnetic Actuator (OSEM) on the suspension cage (Fig. 4.4).

4.2.3 Arm cavity mirrors

The arm cavity suspension hardware can accommodate any 10 cm high-reflectivity mirror. The mirrors currently in use are fused silica with $T = 300$ ppm HR coatings, polished and coated by REO. The TNI lab has available sets of $T = 300$ ppm sapphire mirrors which can be used in future studies.

As with LIGO mirrors, they have magnets on aluminum dumbbell standoffs [55] attached to their side and back for local damping. To minimize the mirror's magnetic dipole moment, the orientations alternate for the magnets on the back surface [62].

Figure 4.2: Top view of optics layout. The mode cleaner can operate in either horizontal polarization for low finesse or in vertical polarization for high finesse.

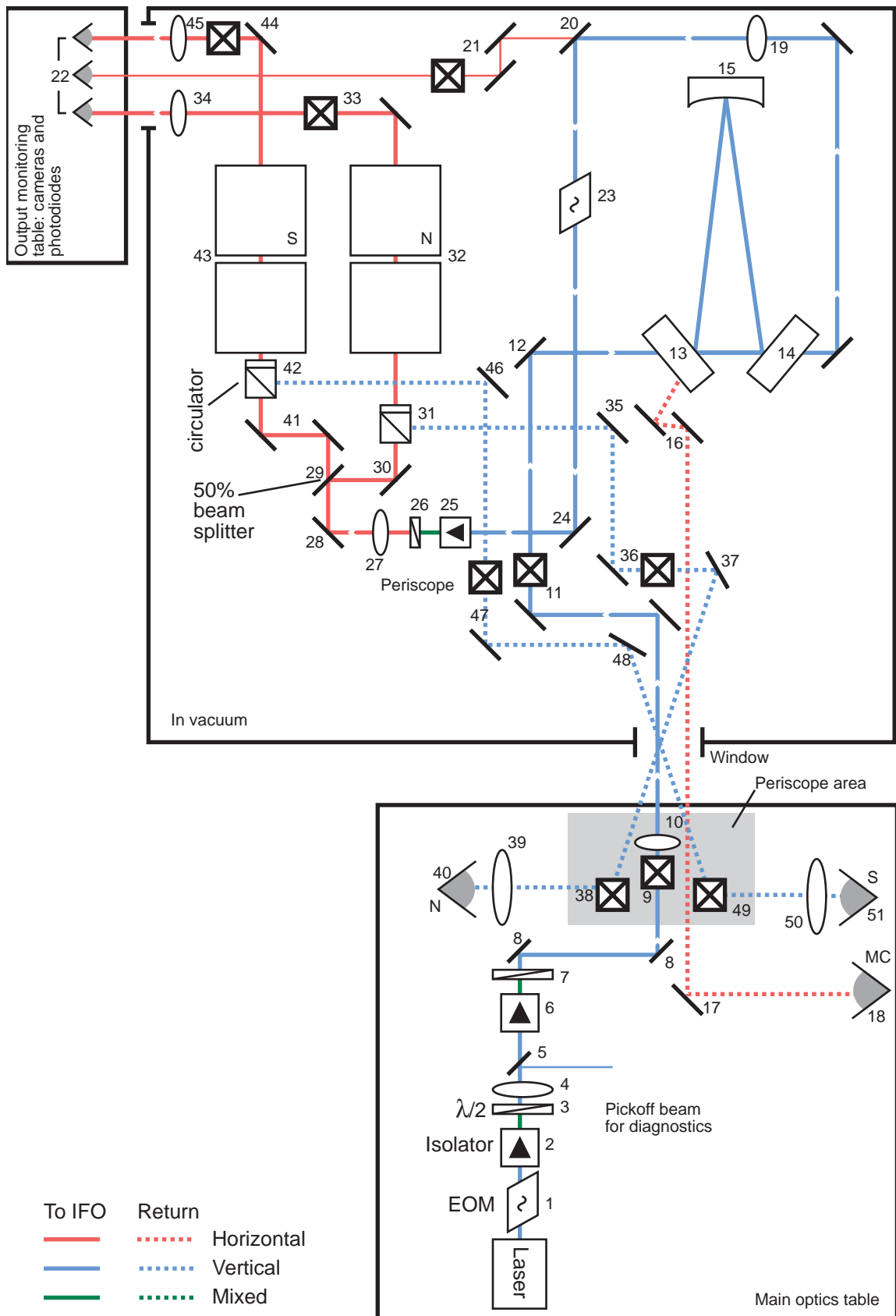


Figure 4.3: Back and side view of a mode cleaner mirror at 50% scale, adapted from [79]. The line above the side fin indicates the position of the wire standoff.

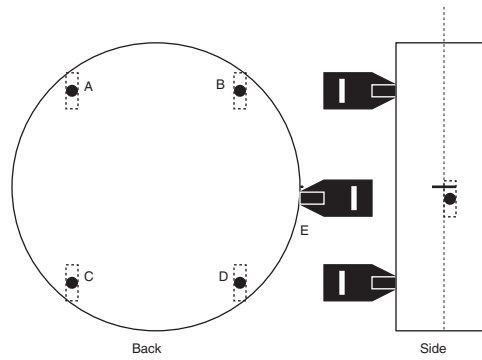
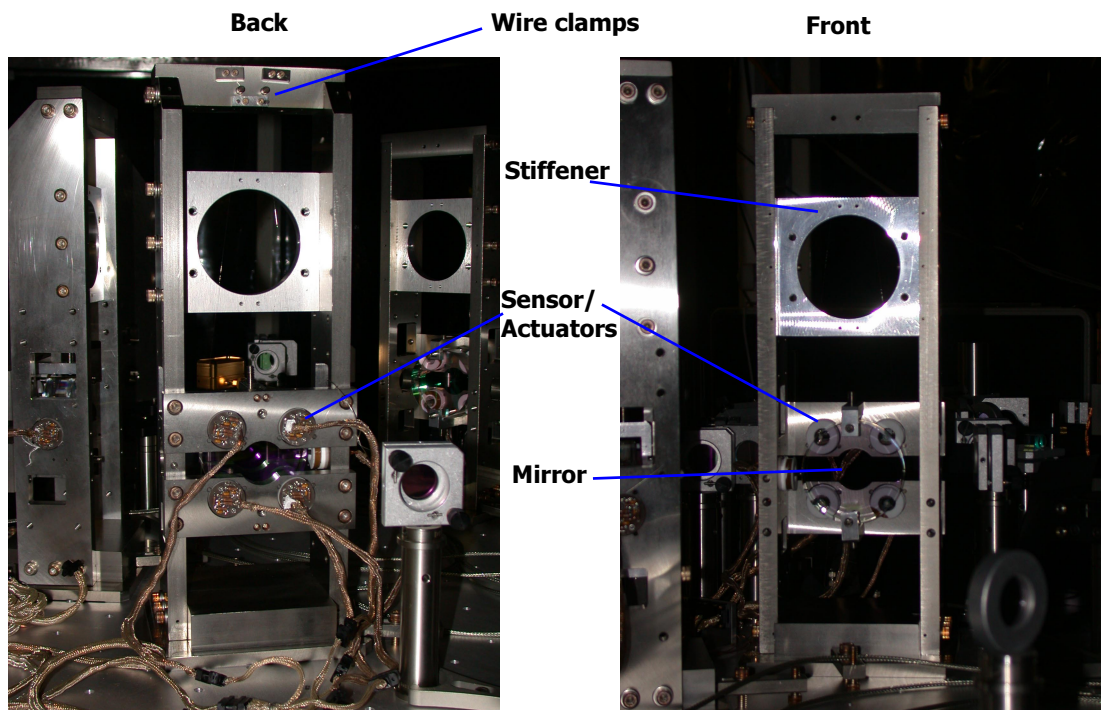


Figure 4.4: Mode cleaner suspension towers.



4.2.4 Mechanics

The mechanical structures of the TNI are designed to reduce seismic noise. A vibration isolation stack [52, 50] supports the optics table for the mode cleaner and arm cavities. On top of isolation stack, the suspended interferometers themselves are in pendulum suspensions [61]. The main optics table holding the laser simply rests on the ground.

4.2.4.1 Seismic isolation

The vibration isolation system (Fig. 4.5) is a 4-layer stack of steel and elastomer.¹

Wires are anchored to the support blocks to minimize vibration transmission. Electrical feed-throughs are on the bottom part of the chamber, while windows are on the top part. The vacuum chamber is supported by one set of legs (see Fig. 4.5), while the instrument table rests on a separate set of legs.

4.2.4.2 Suspensions

The mode cleaner mirror suspensions (Fig. 4.4) are modified LIGO Small Optic Suspensions (SOS) [61]. These consist of an arch of stainless steel¹ with two crossbeams to hold the OSEMs. The main difference between these and LIGO SOSs is that these use C-clamps with set screws for earthquake stops to lower their cost. The mirrors are supported by a loop of steel music wire clamped at the top. The SOSs are designed to have resonant frequencies outside the bandwidth of the local damping servo: for a LIGO SOS tower, the vertical resonance frequency is 16 kHz and the lowest measured internal mode is at 156 Hz [70].

The arm cavity mirror suspensions are scaled up versions of the SOS (Fig. 4.6). Each suspension cage holds two mirrors, with the suspension wires clamped to the same piece of metal.

4.3 Mode cleaner and laser servo

A feedback servo system locks the mode cleaner and laser to one another (Fig. 4.7). At low frequencies, the laser is a stable reference for the suspended mirrors of the mode cleaner. At high frequencies, the cavity has much better frequency stability than the laser.

¹This is the same stack used at the LIGO Phase Noise Interferometer [50].

¹Type 304, non-magnetic, free-machining stainless steel, with an aluminum stiffening plate. Type 303 stainless is not suitable for precision machining of large parts since magnetic steels will attract the mirror magnets, and mounting the OSEMs in a high-conductivity metal like aluminum can lead to greater eddy-current damping.

Figure 4.5: Side view of the opened vacuum chamber. The two arm cavities are on the left, and the mode cleaner is on the right. Counterweights by the mode cleaner balance the weight of the arm cavity suspensions.

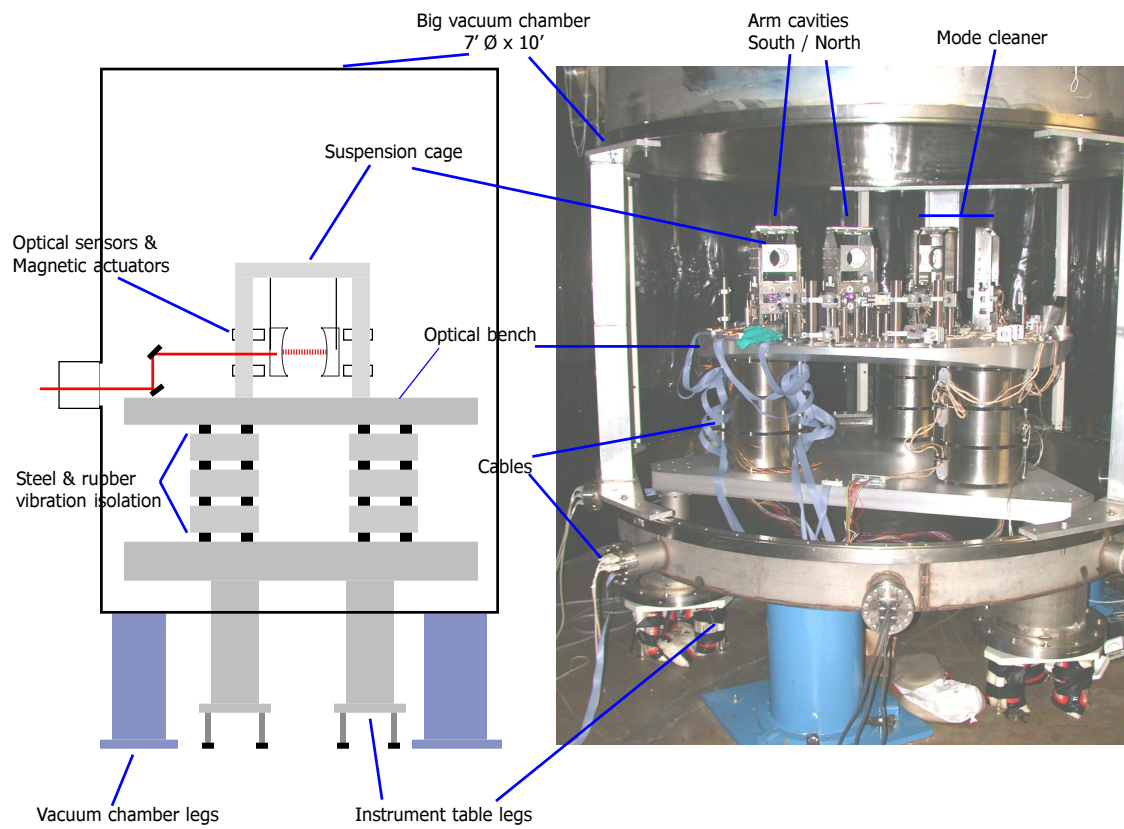


Figure 4.6: A 10 cm arm cavity output mirror. The OSEMs are visible as white rings with red bands behind and to the left of the mirror. The white bars in front of the mirror are Teflon earthquake stops.

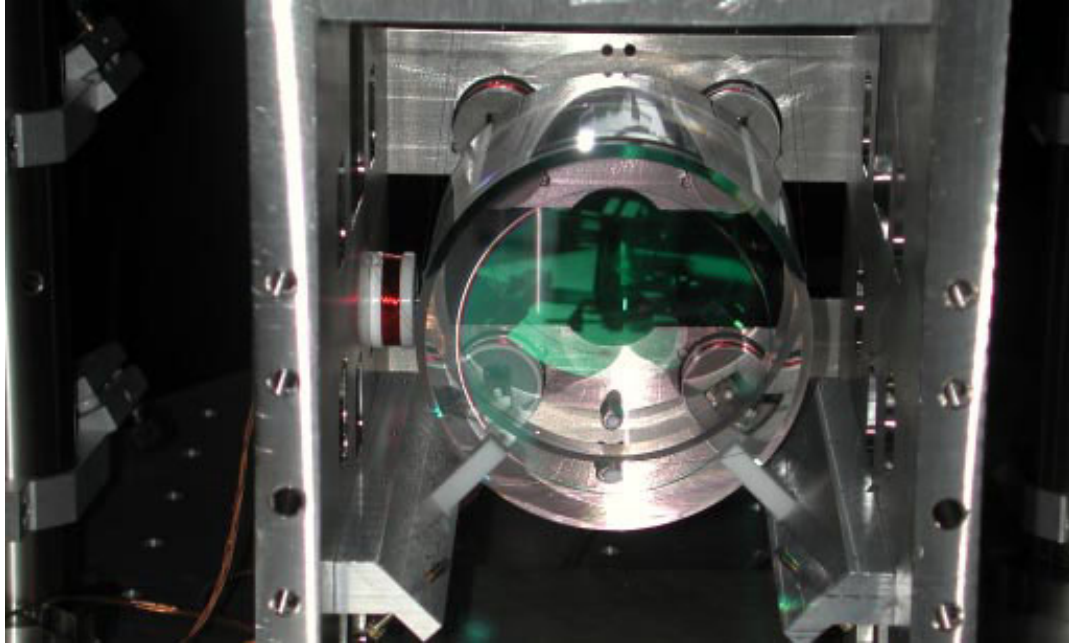
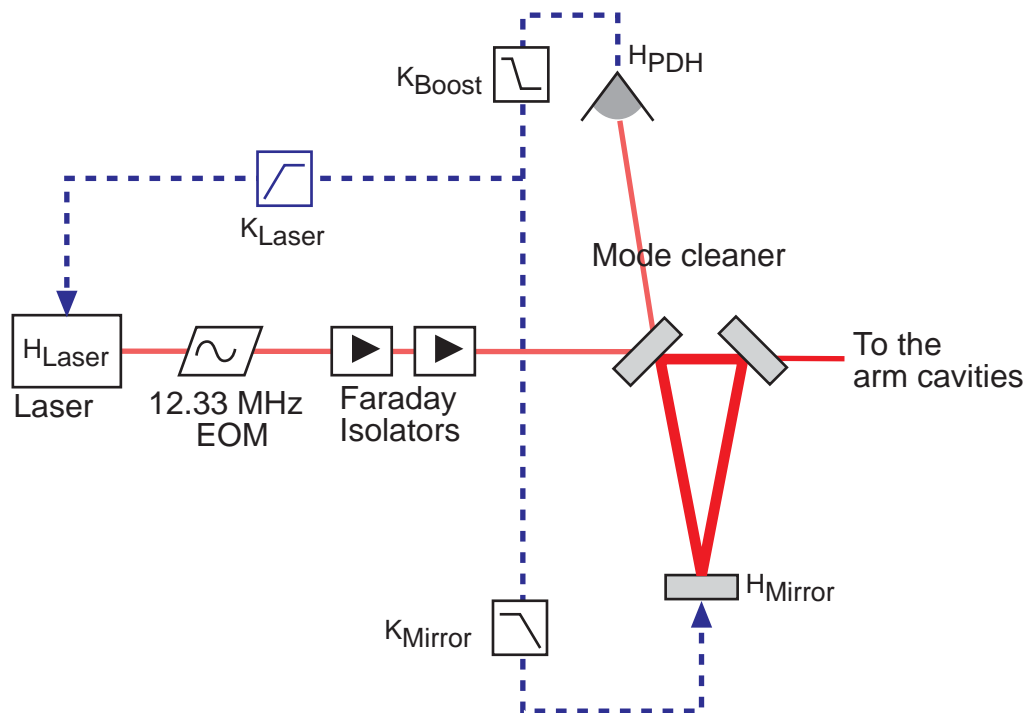


Figure 4.7: Mode cleaner servo



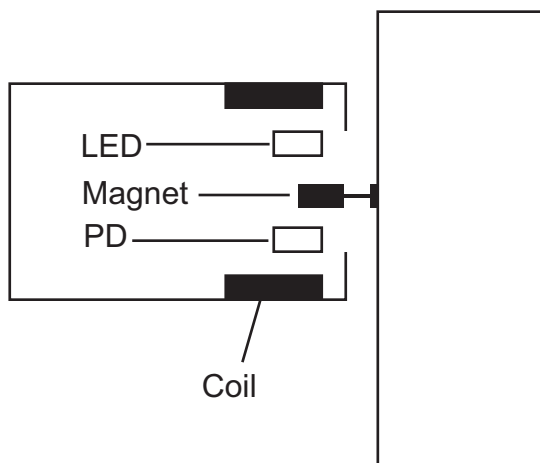
The laser PZT bandwidth is 120 kHz [75], which allows frequency noise suppression up to 90 kHz (see §4.3). If the servo gain is raised so that the unity gain frequency is higher than 90 kHz, servo oscillations occur. Schematics of the servo electronics are documented in LIGO technical notes T000077 and T010023 [18, 17].

4.4 Local damping

Each mirror's OSEMs (from the LIGO 12 m mode cleaner prototype [2]) are powered by a single OSEM controller [33] which acts by velocity damping. From the 4 sensors on the back of the mirror, the controller computes the mirror's displacement in the yaw, pitch, and Z degrees of freedom. These are differentiated to get the velocity, and a voltage proportional to the velocity is applied to the OSEM magnet coils. A 6-pole Butterworth filter at 22 Hz suppresses feedback at high frequencies. The local damping unity gain frequency can be set by adjusting the electronic gain in the OSEM controller.

The mode cleaner OSEMs have a split photodiode and an infrared LED on opposite sides of the fin. When the slit moves about the center of the photodiode, the OSEM produces a voltage proportional to the displacement (see §4.4). The OSEM controller then drives current through a coil in the OSEM, which suppresses motion relative to the suspension tower.

Figure 4.8: Optical Sensor Electro-Mechanical actuator (OSEM)



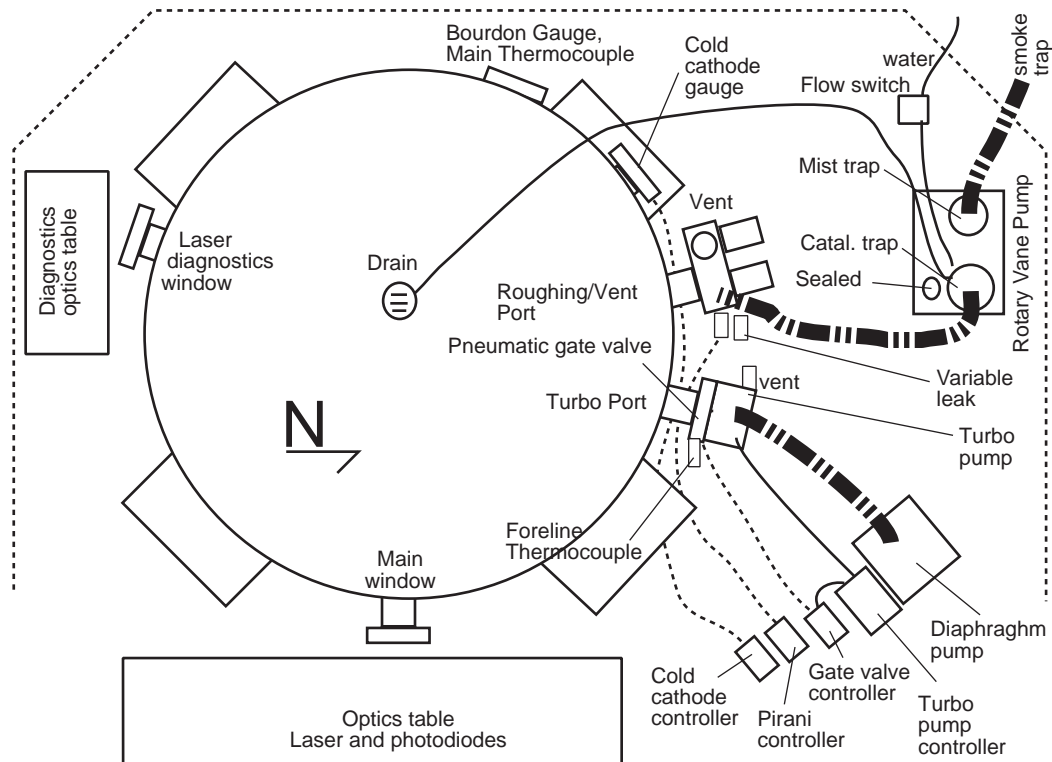
The arm cavity OSEMs (Fig. 4.8) are similar, only they have a single photodiode instead of a split photodiode. For both types, the effect of the local damping system is to reduce the pendulum

Q while preserving its high-frequency noise suppression.

4.5 Vacuum equipment

Since the interferometers are not very long in the TNI, the vacuum requirements are less stringent than for LIGO. For the TNI's 1.5 kg, 10 cm fused silica masses, gas damping in a vacuum of 10^{-6} Torr limits the Q to 10^7 (Eq. ??).

Figure 4.9: TNI vacuum equipment



The primary pump is a rotary vane roughing pump² (Fig. 4.9). The pump's exhaust valve has a two-stage filter: a commercial mist trap, and a bucket of kitty litter. The input valve has a catalytic oil trap on the foreline to break down oil migrating back into the chamber. The oil trap operates at 250° C, and uses water cooling to keep the case from becoming a safety hazard. To further prevent oil contamination, a pinhole leak at the beginning of the foreline limits the pressure the roughing pump can reach to about 150 mTorr [121].

After the roughing pump has finished its job, the foreline valve is closed and the turbo pump

²Alcatel model 2063CP

takes over. The turbo pump³ is attached to the chamber at a separate port via a pneumatic gate valve. The gate valve is interlocked to the turbo pump, and closes if the power fails or if the pump speed falls below 42krpm, which can happen if the gate valve when the pressure inside the vacuum chamber is too high. The turbo pump is backed by an oil-free diaphragm pump⁴.

The vacuum pressure can be observed by a Bourdon (bellows) gauge from atmosphere to 25 Torr, a Pirani gauge⁵ from 20 torr to 10 mTorr, and a cold-cathode gauge⁶ below that. It takes about 4 hours to pump down from atmosphere to 150 mTorr, and a day to pump down from there to 10^{-4} Torr. It takes several days after that to reach the lower limit of about 10^{-7} Torr. Fortunately, the instrument locks in air so long as the chamber is closed.

4.6 Results and summary

At the end of 2001, with only one arm cavity running, the TNI reached the 10^{-18} m/rHz noise level. After a year of upgrades and improvements, both arms run reliably and robustly, with matched sensitivities of $\sim 5 \times 10^{-18}$ m/rHz at 1 kHz. At this level, the noise is dominated by seismic noise at low frequencies and laser frequency noise at high frequency.

Estimates of the detector sensitivity are plotted in Fig. 4.10 and 4.11 [16], along with plausible levels of thermal noise. These data are taken with a Stanford Research 780 network analyzer measuring the power spectrum of the arm cavities' PDH signals. The raw data are then scaled by the inverse of the open-loop transfer function by the method described in the previous chapter.

Pendulum thermal noise is estimated from the wire loss angle 3×10^{-4} [53] and the pendulum dilution factor 1×10^{-2} [111]. The coating structural damping noise estimate is based on the mirror loss angle $\phi_{\perp} = 10^4$ measured by Harry *et al.* on similar coatings [60]. The substrate structural damping noise estimate is based on the highest bulk Q measured *in situ*, 3×10^6 .

³Varian model V300 HT

⁴Gremenberger Antriebstechnik GmbH, model VDEO530

⁵Kurt J Lesker Co, model 902016

⁶MKS Instruments, Coulter CO, model 421

Figure 4.10: North arm cavity sensitivity. [16]

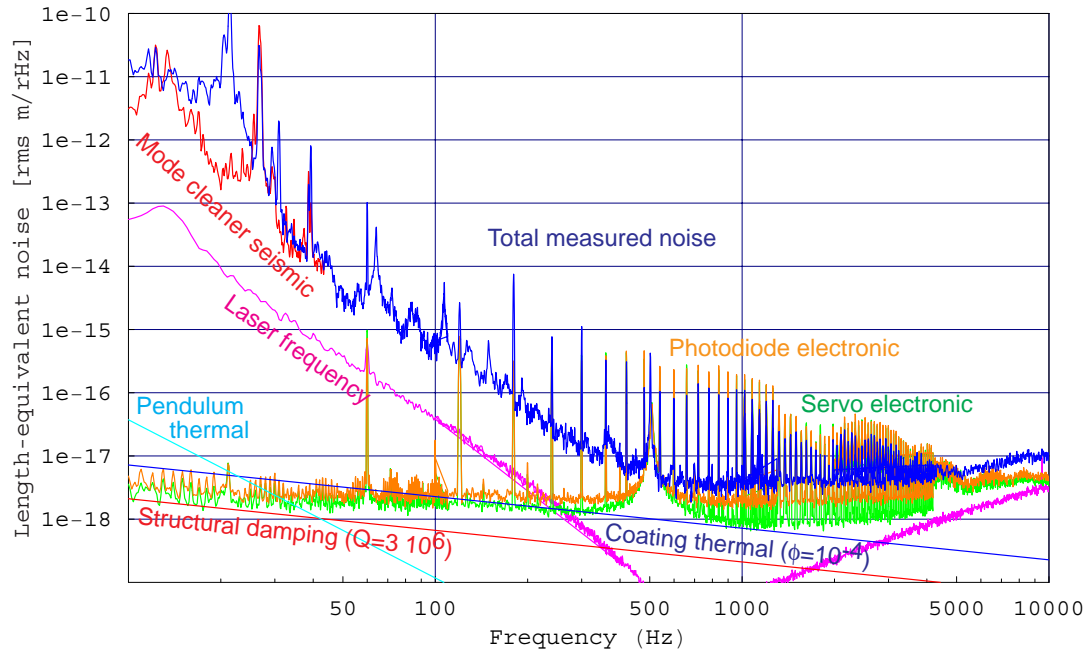
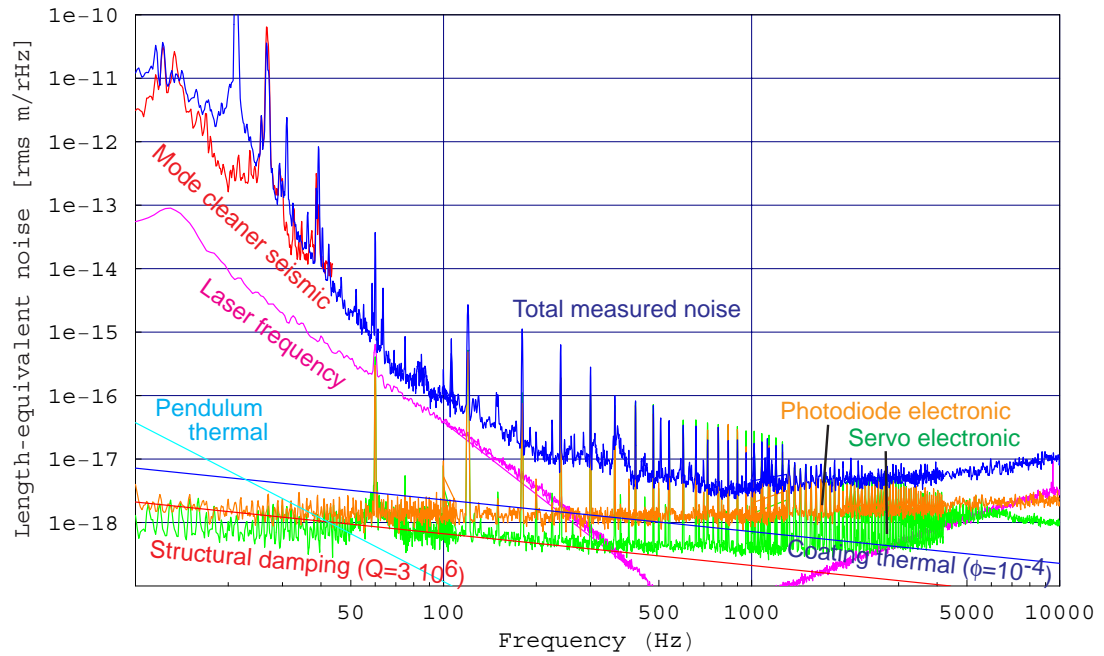


Figure 4.11: South arm cavity sensitivity. [16]



Chapter 5

Summary

The LIGO community has been studying thermal noise in interferometers since the beginning of the project, and will likely continue to do so in the near future. Every year, new, previously unexpected types of thermal noise are being discovered, and experiments are only starting to catch up with theory. Structural damping noise was given the generic name “thermal noise” when it was the only expected noise source in the mirrors. Since then, the catalog has grown to include those described Chapter 2, as well as many other noise sources that aren’t intrinsic to the mirrors.

The first success at measuring thermal noise was in 1994, when the old LIGO 40 m prototype interferometer measured a noise floor consistent with structural damping at the 10^{-18} m/rHz level [55]. Recently, Harry *et al.* [60] have put a handle on coating structural damping, and Kenji Numata [94] has measured thermoelastic noise and structural damping at the 10^{-18} m/rHz level at high frequencies (≥ 1 kHz) in high-noise substrates. But we have very little data on the interactions between the mirror coatings and the substrate, which has been predicted by some to be the greatest limit to improving LIGO’s sensitivity [26, 108].

Using the photothermal data from Chapter 3, we can provide a hint that something interesting happens between the mirror coating and the substrate. The data from sapphire are consistent with the model for the photothermal effect derived in Chapter 2, which assumes that the dielectric coating on the mirror is a low-conductivity glass. Relevant to LIGO I mirrors, the photothermal data for BK7 and fused silica both suggest that the coating makes a significant contribution to a mirror’s thermal expansion, and that it increases at higher frequencies. The implication that the coating is not necessarily a slave to the substrate’s temperature suggests that models for coating thermoelastic noise need to account for fluctuations originating in the coating as well as in the substrate.

There are two aspects to photothermal noise: thermal expansion and index of refraction. Are test mass surface fluctuations due to these correlated? If so, then coatings could be designed in

which a negative dn/dT cancels thermal expansion, thus completely removing coating thermoelastic noise as a problem for LIGO. Pursuing this will require more experiments to understand coating properties, as well as direct measurements of coating thermoelastic noise.

Further development on the photothermal experiment should focus on evaluating more coatings, particularly Ta_2O_5/SiO_2 dielectric stacks like those used in LIGO, and on extending the measurements to higher frequencies to observe the high frequency behavior of the coating. It would be especially interesting to observe the photothermal response above 10 kHz, where the thermal diffusion length is less than the coating thickness.

Appendix

5.1 Coating photothermal effect in low-conductivity substrates

Assuming that the coating has the same thermal diffusivity as the substrate, we can calculate the coating's photothermal response by starting with the heat diffusion equation for half-space. The coating's thermal expansion is then determined by finding the average temperature of the mirror in a layer near the surface. I ignore the equation of elasticity, which is used on similar problems in [22, 23, 32], and which I expect to introduce corrections of order unity.

$$\begin{aligned} \left(\frac{\partial}{\partial t} - \frac{\kappa}{\rho C_v} \nabla^2\right) u(\vec{r}, t) &= \frac{2P_0(f)\delta(z)e^{-(x^2+y^2)/r_0^2}}{\rho C_v \pi r_0^2} = F(\vec{r}, t) \\ u(\vec{r}, t)|_{z \rightarrow \infty} &= 0 \\ 0 \leq z &\leq \infty \end{aligned} \quad (5.1)$$

It is convenient to solve the Fourier transform of this equation. Letting $a^2 = \frac{\kappa}{\rho C_v}$,

$$u(\vec{r}, \omega) = \frac{1}{2\pi^3} \int_{-\infty}^{\infty} d\vec{k} \frac{F(\vec{k}, \omega)}{a^2 k^2 + i\omega} \quad (5.2)$$

To select for temperature fluctuations near the surface, I follow the method of BGV [23] and use a weighting factor $e^{-z/l}/l$ to average over the zone near the surface. As measured by an interferometer, the response of the coating is given by the weighted average of $u(\vec{r}, \omega)$ over a Gaussian beam spot with radius r_0 . (The equations for integrating thermal expansion over the full thickness of the substrate are covered in [32].)

$$\bar{u}(\omega) = \frac{2P_0(\omega)}{\rho C(2\pi)^3} \int_{\vec{k}, x, y=-\infty}^{\infty} \int_{z=0}^{\infty} d\vec{k} dx dy dz \frac{e^{-z/l}}{l} \frac{e^{-(x^2+y^2)/r_0^2}}{\pi r_0^2} \frac{e^{-(k_x^2+k_y^2)r_0^2/4}}{a^2 k^2 + i\omega} e^{-i\vec{k}\cdot\vec{r}}$$

Evaluating the x, y, z integrals first gives

$$\bar{u}(\omega) = \frac{2P_0(\omega)}{\rho C(2\pi)^3} \int_{-\infty}^{\infty} d\vec{k} \frac{1}{1 - ik_z l} \frac{e^{-(k_x^2+k_y^2)r_0^2/2}}{a^2 k^2 + i\omega} \quad (5.3)$$

Integrating next in k_z gives

$$\bar{u}(\omega) = \frac{P_0(\omega)}{\rho C(2\pi)^2} \int \int_{-\infty}^{\infty} dk_x dk_y \frac{e^{-(k_x^2+k_y^2)r_0^2/2}}{a\sqrt{a^2(k_x^2+k_y^2) + i\omega} - il(a^2(k_x^2+k_y^2) + i\omega)}$$

To evaluate this, take l to be the thermal diffusion length $r_t = \sqrt{\kappa/\rho C\omega} = a/\sqrt{\omega}$. This is difficult to compute at low frequencies, but at high frequencies, where $\omega \gg a^2/r_0^2$, we may ignore the terms in the denominator not proportional to $\sqrt{\omega}$. Noting that the dominant contribution to the integral comes when $k \approx 1/r_0$, we can approximate the displacement due to coating thermal expansion.

$$\begin{aligned} \bar{u}(\omega) &\approx \frac{P_0(\omega)}{\rho C(2\pi)^2} \int \int_{-\infty}^{\infty} dk_x dk_y \frac{e^{-(k_x^2+k_y^2)r_0^2/2}}{a\sqrt{a^2/r_0^2 + i\omega} + a\sqrt{\omega}} \\ \bar{z}(\omega) &= \alpha d \bar{u}(\omega) \approx \frac{\alpha d P_0(\omega)}{\pi r_0^2 \sqrt{\rho C_v \kappa \omega} (1+i)} \end{aligned} \quad (5.4)$$

Square this and replace $P(\omega)$ with the shot noise spectral density (see §2.4.1).

$$S_{\alpha, P}^{layer*}(f) \approx \frac{\alpha_{layer}^2 d^2 S_{abs}(f)}{4\pi^3 r_0^4 \rho C_v \kappa f} \quad (5.5)$$

where d is the thickness and α is the thermal expansion coefficient of the coating.

5.2 Cross-coupling noise

To derive equations 3.9 and 3.10, I assume weak modulation depth at the EOM, so that only the carrier and first-order sidebands of the *probe* beams are significant. Following the formalism of Day [41], the light falling on the cavity on resonance is

$$\begin{aligned} P_0 &= |E_r + E_u|^2 \\ E_r &= \sqrt{P_C} e^{i\varpi t} + i\sqrt{P_S} \sin(\Omega t) e^{i\varpi t} \end{aligned} \quad (5.6)$$

$$E_u = \sqrt{P_F} e^{i\varpi t} e^{i\phi} \quad (5.7)$$

where ϖ is the light frequency, Ω is the sideband modulation frequency, and ϕ is a random phase shift, not necessarily stationary in time.

The *probe* beam field can be expanded as

$$E_r = \sqrt{P_C} e^{i\varpi t} + i\sqrt{P_S/2} (e^{i(\varpi+\Omega)t} - e^{i(\varpi-\Omega)t}) \quad (5.8)$$

The amplitude reflection coefficient depends on the input (r_1) and test (r_2) mirror amplitude reflectivities and input mirror losses (L_1). Lower-case letters indicate field coefficients, while capital letters apply to power.

$$A(\varpi) = \frac{r_2(1 - L_1)e^{i\varpi/FSR} - r_1}{1 - r_1 r_2 e^{i\varpi/FSR}} \quad (5.9)$$

The quantity ϖ/FSR may be replaced by $4\pi\Delta L/\lambda$ to convert frequency shifts to length changes. The field reflected from the cavity is

$$\begin{aligned} E_{refl} &= |\sqrt{P_F} e^{i\varpi t} e^{i\phi} A(\varpi) + \sqrt{P_C} e^{i\varpi t} A(\varpi) + \\ &\quad \sqrt{P_S} e^{i(\varpi+\Omega)t} A(\varpi + \Omega) - \sqrt{P_S} e^{i(\varpi-\Omega)t} A(\varpi - \Omega) \end{aligned} \quad (5.10)$$

The polarizing optics split the *pump* and *probe* beams on their return paths, and direct the *probe*

beam, and a small amount of the *pump* beam, toward the RFPD. Between the IFO and the photodiode, the light power is attenuated overall by various filters and transmissive optics, so that the field that we measure at the RFPD is proportional to

$$E_{PD} \propto \zeta \sqrt{P_F} e^{i\varpi t} e^{i\phi} A(\varpi) + \sqrt{P_C} e^{i\varpi t} A(\varpi) + \sqrt{P_S} \left[e^{i(\varpi+\Omega)t} A(\varpi + \Omega) - e^{i(\varpi-\Omega)t} A(\varpi - \Omega) \right] \quad (5.11)$$

If the demodulation phase at the mixer is chosen to maximize the zero-crossing slope of the PDH signal, then the maximum amount of systematic error due to polarization crosstalk will occur when $\phi \rightarrow 0$ or π . Consider all four fields as phasors. The sum of the carrier and force fields is a field in phase with the carrier. The PDH signal arises from the beat between the carrier (or the sum of the carrier and the noise field) and the two sidebands.

The optical power reaching the photodiode is $P_{PD} = |E_{PD}|^2$. After some algebra, this may be written as

$$\begin{aligned} P_{PD} \propto & \zeta^2 P_F + P_C + 2\zeta \sqrt{P_C P_F} \cos(\phi) |A(\varpi)|^2 + \\ & 2\sqrt{P_S P_C} \{ \Re [A(\varpi) A^*(\varpi + \Omega) - A^*(\varpi) A(\varpi - \Omega)] \cos \Omega t + \\ & \Im [A(\varpi) A^*(\varpi + \Omega) - A^*(\varpi) A(\varpi - \Omega)] \sin \Omega t \} + \\ & 2\sqrt{P_S P_C} \{ \Re [A(\varpi) A^*(\varpi + \Omega) e^{i\phi} - A^*(\varpi) A(\varpi - \Omega) e^{-i\phi}] \cos \Omega t + \\ & \Im [A(\varpi) A^*(\varpi + \Omega) e^{i\phi} - A^*(\varpi) A(\varpi - \Omega) e^{-i\phi}] \sin \Omega t \} \\ & + 2\Omega \text{ terms...} \end{aligned} \quad (5.12)$$

The terms proportional to $\sqrt{P_F P_S}$ may be simplified. In the linear region of the PDH signal, near a cavity resonance,

$$F(\varpi) F^*(\varpi + \Omega) = -F(\varpi) F^*(\varpi - \Omega) \quad (5.13)$$

Using this approximation, we arrive at

$$\begin{aligned}
P_{PD} \propto & \zeta^2 P_F + P_C + 2\zeta\sqrt{P_C P_F} \cos(\phi) |A(\varpi)|^2 + \\
& 2\sqrt{P_S}(\sqrt{P_C} + \zeta\sqrt{P_F} \cos(\phi)) \{ \Re [A(\varpi)A^*(\varpi + \Omega) - A^*(\varpi)A(\varpi - \Omega)] \cos \Omega t + \\
& \Im [A(\varpi)A^*(\varpi + \Omega) - A^*(\varpi)A(\varpi - \Omega)] \sin \Omega t \} \\
& + 2\Omega \text{ terms...}
\end{aligned} \tag{5.14}$$

The photodiode measures high frequency (P_{RF}) and low frequency (P_{DC}) components of the optical field separately. Because the mirror reflectivities are not perfectly matched in this experiment, the P_{DC} is non-zero at resonance.

$$P_{DC} = |A(0)|^2 \left(P_C + 2\zeta\sqrt{P_F P_C} \cos \phi + \zeta^2 P_F \right) \tag{5.15}$$

$$A(0) = \frac{r_2 - r_1}{1 - r_1 r_2} \tag{5.16}$$

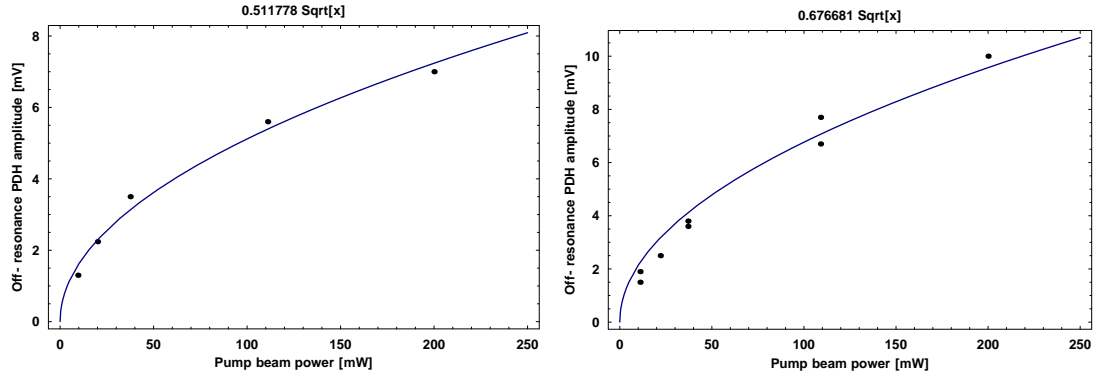
The PDH signal consists of the components of P_{RF} at the sideband frequency, Ω . The low frequency component of this is converted into the measured PDH signal.

$$\begin{aligned}
V_{PDH} = & V_0 \{ \Re [A(\varpi)A^*(\varpi + \Omega) - A^*(\varpi)A(\varpi - \Omega)] \cos \theta + \\
& \Im [A(\varpi)A^*(\varpi + \Omega) - A^*(\varpi)A(\varpi - \Omega)] \sin \theta \}
\end{aligned} \tag{5.17}$$

where θ is the phase shift between the local oscillator and RF inputs at the mixer and V_0 is an arbitrary scale factor.

Cross-coupling can be measured directly with the instrument's polarizing optics set poorly and the cavity off resonance. Measurements of the variations in the PDH signal under these conditions show that the cross-coupling noise is proportional to the square roots of both the carrier and sideband power. Fig. 5.1 plots the cross-coupling for a variety of *pump* and *probe* powers.

Figure 5.1: Cross-coupling dependence on beam power. Left: *probe* power = 16 mW. Right: *probe* power = 26 mW. Data are fit to $P_F^{1/2}$.



5.3 Interferometer identities

In a Fabry-Perot interferometer, the Finesse is the ratio of the line width (FWHM of transmitted power) to the free spectral range (FSR). In frequency units, the FSR is $c/2L$. In length units, it is $\lambda/2$. The conversion factor from frequency to length is simply $\lambda L/c$. The various reflection and transmission coefficients for lossy, asymmetric cavities on resonance are

$$\begin{aligned} \text{Reflection} &= \left(\sqrt{R_1} - T_1 \sum_0^{\infty} (R_1 R_2)^{n/2} \right)^2 \\ &= \left(\sqrt{R_1} - \frac{\sqrt{R_2} T_1}{1 - \sqrt{R_1 R_2}} \right)^2 \end{aligned} \quad (5.18)$$

$$\begin{aligned} \text{Transmission} &= T_1 T_2 \left(\sum_0^{\infty} (R_1 R_2)^{n/2} \right)^2 \\ &= \frac{T_2 T_1}{(1 - \sqrt{R_1 R_2})^2} \end{aligned} \quad (5.19)$$

$$\begin{aligned} \text{Buildup} &= T_1 \left(\sum_0^{\infty} (R_1 R_2)^{n/2} \right)^2 \\ &= \frac{T_1}{(1 - \sqrt{R_1 R_2})^2} \end{aligned} \quad (5.20)$$

Note that $T_1 + R_1 \leq 1$ and $T_2 + R_2 \leq 1$.

5.4 TNI

5.4.1 Mode cleaner electronics

The K_{boost} amplifier in the mode cleaner servo (see §4.7) is critical for lock acquisition. It has two $\times 10$ boost stages at low frequency to increase the DC gain of the servo without affecting its unity gain point. Fig. 5.3 It can be used as a low-noise variable-gain inverting amplifier, with a single boost enabled, or with both boosts enabled¹. It is mounted in a single-width NIM box and requires ± 24 V, regulated down to ± 15 V. The circuit is built in three stages, each based on the AD797 high-speed op amp. The first stage (*gain*) is a variable-gain amplifier with two inputs. In_1 has an input impedance of $1\text{ k}\Omega$ and a range of ± 15 V. In_2 is limited to 800 mV_{pp} and, for small signals, has a $4.7\text{ k}\Omega$ input impedance. The response of the first stage is $V_1 = -G(In_1 + In_2/4.7)$. The second and third stages (*boost2*, *boost2*) are switchable lags: With the switch closed, they are unity-gain inverting amplifiers. With the switch open, their response is $V_2 = -100(V_1(if + 10000)/(if + 100))$. The front panel has BNC connectors for the inputs and outputs, a knob to adjust the gain (VR1), and switches (SW1, SW2) to enable the boosts. The recommended operating range for the gain knob is from 0.4 to 9.5.

The amplifier's input referred noise is 5 nV/rHz at each op-amp stage. There appears to be some high-frequency resonance, possibly because of the inductance of the twisted-pair wires connecting the circuit board to SW1 and SW2 on the front panel. The amplifier also picks up an oscillation at 80 MHz , possibly from an FM broadcast. There is an input offset at each stage of about 100 mV , depending on temperature. Input offsets are adjustable for each chip with trim pots on the circuit board.

¹See the *North Arm Cavity and Beyond* lab notebook, page 114.

Figure 5.2: Schematic of reflection and transmission used in deriving the above formulae. $\sqrt{R_1} = r_1$, etc.

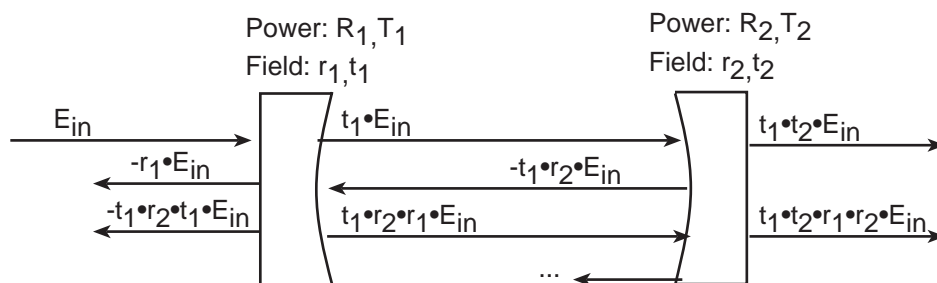
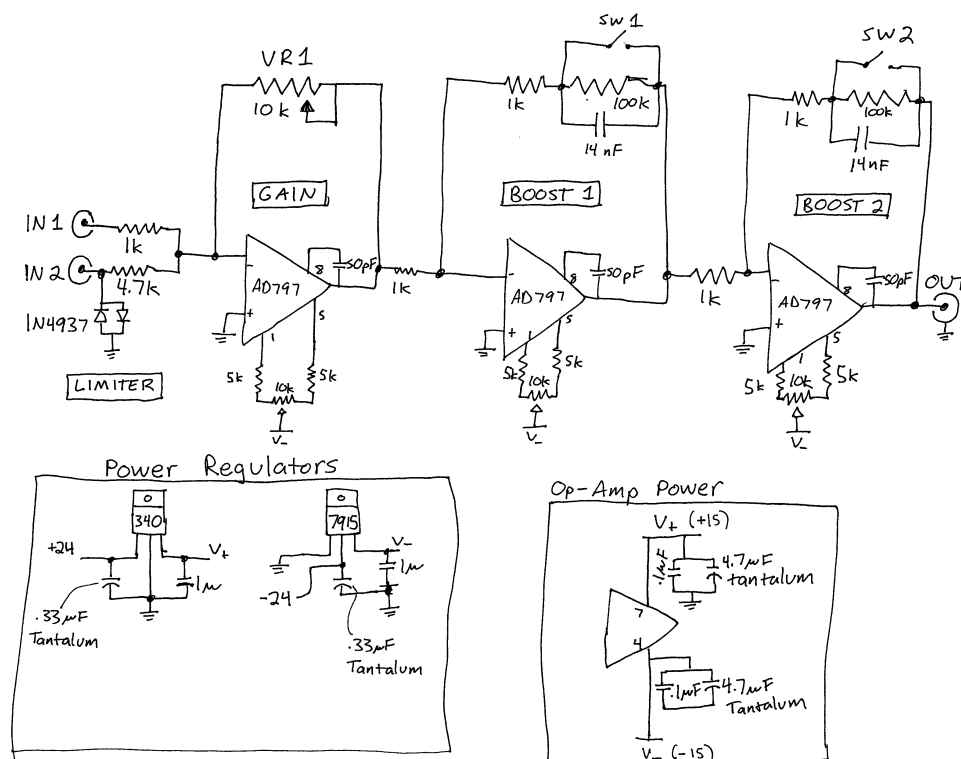


Figure 5.3: Boost amplifier circuit schematic



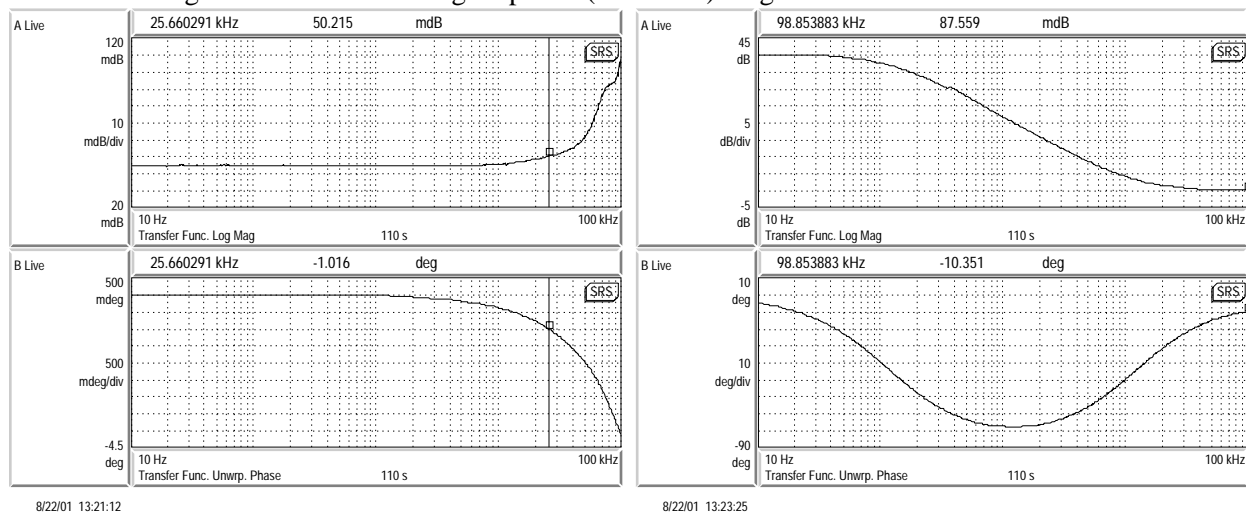
As an inverting amplifier with both boosts off, phase lag is less than 5° at 100 kHz. Either of the two identical boost stages may be activated with the front-panel switches. A transfer function of the amplifier with one boost shows a pole at 100 Hz, a zero at 10 kHz, and a DC gain of 40 dB. Phase lag for each boost at 100 kHz is less than 6° . Fig. 5.4 shows the measured transfer functions for the inverting amplifier configuration and for one boost enabled.

5.4.2 Alignment procedure

The first step to aligning the TNI is to balance the instrument table in the vacuum chamber. If the table is not level, it can drift and tilt enough over a few days to displace the suspended mirrors by more than a millimeter. So all the optics need to be assembled and the table balanced before you can align the beam to the cavities.

It can be difficult to find the resonant axis of the mode cleaner. You should set up a HeNe laser on the auxiliary table, and send it backwards through the mode cleaner. Since dielectric mirrors designed for 1 micron partially reflect red light, the mode cleaner will form a low finesse ring cavity for the HeNe beam. When the HeNe is aligned to the mode cleaner, there is a transmitted bull's-eye

Figure 5.4: Left: inverting amplifier (no boosts). Right: one boost active.



pattern that shifts as the mirrors swing in response to air currents. The cavity is properly aligned the laser when this beam overlaps the NPRO beam.

5.5 Calibration procedure

There are two ways to calibrate the interferometer responses. The simplest is to let the mirror swing through a resonance while measuring the slope of the PDH signal. The other is to measure the open-loop transfer function of the servo, and divide it by the gains of all the components except for the interferometer response. These procedures can be accurate to within 10-20%. A better calibration method would use a photon drive.

5.5.1 OSEM optimization procedure

Local damping works best when the center of the OSEMs' dynamic range coincides with the natural resting position of the mirror. On the mode cleaner, the OSEM circuit boards are constructed such that the LED will burn out if the board contacts touch any piece of grounded metal, such as the insulation on the cables.

1. Turn off the controller.
2. Remove all the sensor/actuators from the suspension. Place them on the table in such a way that you will remember where they belong. Be careful that the circuit boards aren't touching anything metallic. If they do, the LED will blow out and need to be replaced.

3. Set the yaw, pitch, and Z switches to *global* mode to disable feedback.
4. Turn the controller on. Turn all the offset pots to 5.00. The gain knobs have no effect.
5. Insert an OSEM into the suspension. Start with the one that is in the most awkward position (usually LL or LR). Connect the Local Position Monitor signal for this sensor to both input channels of an oscilloscope. Set one of the scope channels to 5 V/div and the other to 0.1 V/div.
6. Move the sensor/actuator around in the SOS until its position measures zero. Tighten the set screw to hold it in place.
7. Repeat steps 5-6 for the remaining mirror-back OSEMs, but not for the horizontal one yet.
8. Re-check all the local position signals. Inspect the front of the mirror and make sure that no fins rub against the inside of the OSEMs.
9. Set the yaw, pitch, and Z switches to *local* mode. The mirror should damp in these degrees of freedom, but is still free to swing from side to side.
10. Insert the horizontal sensor/actuator, monitoring its position as in step 5.
11. Increase the side channel gain on the OSEM controller.
12. The mirror should damp in all degrees of freedom.

5.5.2 Venting the vacuum chamber

1. Check all vacuum gauges. The cold cathode gauge should reach 10^{-6} Torr.
2. If the turbo pump is on, it should say “Normal Operation 56 krpm.”
3. Close all valves to the vacuum chamber. Flip the switch on the gate valve controller box to “close”. Turn the handle on the roughing valve to close it. Turn the handle on the vent valve clockwise to close it.
4. To turn the turbo pump off, press the “Start/Stop reset” button on the controller. The turbo pump controller will say “Ready for local soft start.” The turbo pump and the fan will both stop. After five seconds, the vent valve for the turbo pump will open. Air coming into the

pump will slow down the pump, and you will be able to hear the whine as it spins down. Turn the turbo pump controller off, then turn the diaphragm pump off.

5. Turn the cold cathode gauge off.
6. The roughing valve should be closed, so that the catalyzer trap stays hot and under vacuum.
7. Vent the chamber by slowly opening the vent valve (counterclockwise). Air will flow in for about 20 minutes.

Bibliography

- [1] A. Abramovici, W. Althouse, R. Drever, Y. Gursel, S. Kawamura, F. Raab, D. Shoemaker, L. Sievers, R. Spero, K. Thorne, R. Vogt, R. Weiss, S. Whitcomb, and M. Zucker. *Science*, 256:325–333, 1992.
- [2] Alex Abramovici, Dick Prout, Jake Chapsky, Larry Jones, Julius Jodele, Doug Jungwirth, Lawrence Chu, Oliver McCullough, Boude Moore, Steve Vass, Jordan Camp, Steve Elieson, John Carri, Malik Rakhmanov, and Karl Reithmaier. Review of 12m mode cleaner task. Technical note T950024, LIGO, 1995.
- [3] Alcoa, Inc. Alloy 6061 data sheet. http://www.alcoa.com/adip/catalog/pdf/Extruded_Alloy_6061.pdf.
- [4] Bruce Allen, Maria Alessandra Papa, and Bernard F. Schutz. Optimal strategies for sinusoidal signal detection. *Physical Review D*, 66:102003, 2002.
- [5] P. Ambree, F. Kreller, R. Wolf, and K. Wandel. Determination of the mechanical-stress in plasma-enhanced chemical-vapor-deposited SiO₂ and SiN layers. *J. Vac. Sci. Technol. B*, 11:614, 1993.
- [6] Apache Point Observatory. http://www.apo.nmsu.edu/Telescopes/SDSS/eng.papers/19950926_ConversionFactors/19950926_MProperties.html.
- [7] B. Barish and R. Weiss. Ligo and the detection of gravitational waves. *Physics Today*, 52:44–50, 1999.
- [8] Barry C. Barish and Rainer Weiss. LIGO and the detection of gravitational waves. *Physics Today*, 52:44–50, 1999. LIGO-P990039.

- [9] G. L. Bennis, R. Vyas, R. Bupta, S. Ang, and W. D. Brown. Thermal diffusivity measurement of solid materials by the pulsed photothermal displacement technique. *Journal of Applied Physics*, 84(7):3602–3610, 1998.
- [10] M. Bertolotti, G. L. Liakhou, R. Li Voti, S. Paoloni, and C. Sibilìa. Analysis of the photothermal deflection technique in the surface reflection scheme: Theory and experiment. *Journal of Applied Physics*, 83(2):966, 1998.
- [11] Hans A. Bethe and G. E. Brown. Evolution of binary compact objects that merge. *Astrophysical Journal*, 506:780–789, 1998.
- [12] Biplap Bhawal. Private communication, 2003.
- [13] I A Bilenko, V B Braginsky, and N Yu Markova. Thermal and excess noise in suspension fibres. *Classical and Quantum Gravity*, 19:2035–2038, 2002.
- [14] G. Billingsley, B. Kells, H. Yamamoto, J. Camp, D. Li, H. Armandula, S. Bell, and S. Elieson. Core optics components requirements. Engineering report E980061, LIGO, 1998.
- [15] Eric Black. Thermal Noise Interferometer (TNI). Technical Report G020460, LIGO, 2002.
- [16] Eric Black. Private communication, 2003.
- [17] Eric Black, Seiji Kawamura, Luca Matone, and Shanti Rao. TNI mode cleaner. Technical note T000077, LIGO, 2000.
- [18] Eric Black, Seiji Kawamura, Luca Matone, Shanti Rao, and Kevin Schulz. The TNI first test cavity lock. Technical note T010023, LIGO, 2001.
- [19] Roger Blanford and Kip Thorne. *Applications of Classical Physics*, volume 1. Caltech, 1994. § 5.3.
- [20] I. Blech and U. Cohen. Effects of humidity on stress in thin silicon dioxide films. *Journal of Applied Physics*, 53:4202, 1982.
- [21] P. R. Brady, T. Creighton, C. Cutler, and B. F. Schutz. Searching for periodic sources with LIGO. *Physical Review D*, 57:2101, 98.
- [22] V. B. Braginsky, M. L. Gorodetsky, and S. P. Vyatchanin. Thermodynamical fluctuations and photo-thermal shot noise in gravitational wave antennae. *Physics Letters A*, 264:1, 1999.

- [23] V. B. Braginsky, M. L. Gorodetsky, and S. P. Vyatchanin. Thermo-refractive noise in gravitational wave antennae. *Physics Letters A*, 271:303, 2000.
- [24] V. B. Braginsky, V P Mitrofanov, and K V Tokmakov. Energy dissipation in the pendulum mode of the test mass suspension of a gravitational wave antenna. *Physics Letters A*, 218:164, 1996.
- [25] V. B. Braginsky and A. A. Samoilenko. Measurements of the optical mirror coating properties. *gr-qc/0304100*, 2003.
- [26] V. B. Braginsky and S. P. Vyatchanin. Thermodynamical fluctuations in optical mirror coatings. *cond-mat/0302617*, 2003.
- [27] Adam Bushmaker. Private communication.
- [28] H. B. Callen and R. F. Greene. On a theorem of irreversible thermodynamics. *Physical Review*, 86:702–710, 1952.
- [29] H. B. Callen and T. A. Welton. Irreversibility and generalized noise. *Physical Review*, 83:34–40, 1951.
- [30] G. Carlotti, L. Douce, and M. Dupeux. *J. Vac. Sci. Technol. B*, 14:3460, 1996.
- [31] G P Celata, V P Carey, M Groll, I Tanasawa, and G Zummo, editors. *Nonequilibrium phonon and electron transport in heterostructures and superlattices*, Proc. Int. Conf. Heat Transfer and Transport Phenomena in Microscale. Begell House, Oct 2000. <http://radiation1.mit.edu/Publications/for-web.pdf>.
- [32] M. Cerdonio, L. Conti, A. Heidmann, and M. Pinard. Thermoelastic effects at low temperatures and quantum limits in displacement measurements. *Physical Review D*, 63:082003, 2001.
- [33] Jake Chapsky. OSEM controller schematics. Private communication.
- [34] Corey Collins, CVI Laser. 2003.
- [35] Corning Inc. Corning 7980 data sheet. http://www.corning.com/semiconductormaterials/products_services/semiconductor_materials/hpfs.asp.

- [36] CVI Laser Corp. Optical filters catalog. www.cvilaser.com.
- [37] Jolien D. E. Creighton. Search techniques for gravitational waves from black-hole ringdowns. *Physical Review D*, 60:022001, 1999.
- [38] D R M Crooks, P Sneddon, G Cagnoli, J Hough, S Rowan, M M Fejer, E Gustafson, R Route, N Nakagawa, D Coyne, G M Harry, and A M Gretarsson. Excess mechanical loss associated with dielectric mirror coatings on test masses in interferometric gravitational wave detectors. *Classical and Quantum Gravity*, 19(5):883–896, 2002.
- [39] Crystal Systems, Inc. <http://www.crystalsystems.com/proptable.html>.
- [40] J R Davis, editor. *ASM Handbook*, volume 2. American Society for Materials, 10 edition.
- [41] Timothy Day. *Frequency stabilized solid state lasers for coherent optical communications*. PhD thesis, Stanford University, Stanford, California 94305, 1990.
- [42] Del Mar Ventures. <http://www.sciner.com/Crystals/TiO2.htm>.
- [43] R. W. P. Drever, J L Hall, F V Kowalski, J Hough, G M Ford, A J Munley, and H Ward. Laser phase and frequency stabilization using an optical-resonator. *Applied Physics B*, 31:97, 1983.
- [44] Acernese et al. The present status of the VIRGO Central Interferometer. *Classical and Quantum Gravity*, 19(7):1421–1428, 2002.
- [45] Bondu F, Hello P, and Vinet JY. Thermal noise in mirrors of interferometric gravitational wave antennas. *Physics Letters A*, 246(3-4):227–236, 1998.
- [46] Alexander L. Fetter and John Dirk Walecka. *Theoretical Mechanics of Particles and Continua*. McGraw-Hill, 1980. Ch. 11.
- [47] E E Flanagan and S A Hughes. Measuring gravitational waves from binary black hole coalescences. I. Signal to noise for inspiral, merger, and ringdown. *Physical Review D*, 57(8):4535–4565, 1998.
- [48] Grant R. Fowles. *Introduction to Modern Optics*. Dover, Mineola, NY, 2nd ed. edition, 1968. § 6.1.
- [49] Gorachand Ghosh. *Handbook of Thermo-Optic Coefficients of Optical Materials with Applications*. Academic Press, New York, 1998.

- [50] J. Giame, P. Saha, D. Shoemaker, and L_g Sievers. A passive vibration isolation stack for ligo: Design, modelling, and testing. *Review of Scientific Instruments*, 67:208, 1996.
- [51] J. A. Giame, E. J. Daw, M. Weitz, R. Adhikari, P. Fritschel, R. Abbott, R. Bork, and J. Heefner. Feedforward reduction of the microseism disturbance in a long-base-line interferometric gravitational-wave detector. *Review of Scientific Instruments*, 74(1):218–224, SCIENTIFIC.
- [52] Joseph Giame. *Studies of Laser Interferometer Design and a vibration isolation system for interferometric gravitational wave detectors*. PhD thesis, M.I.T., 1995.
- [53] Aaron Gillespie and Fred Raab. Suspension losses in the pendula of laser interferometer gravitational-wave detectors. *Physics Letters A*, 190:213–220, 1994.
- [54] Aaron Gillespie and Fred Raab. Thermally excited vibrations of the mirrors of laser interferometer gravitational-wave detectors. *Physical Review D*, 52:577, 1995.
- [55] Aaron D. Gillespie. *Thermal noise in the initial LIGO interferometers*. PhD thesis, Caltech, 1995.
- [56] G. Gulsen and M. N. Inci. *Optical Materials*, 18:373, 2002.
- [57] E. Gustafson, D. Shoemaker, K. Strain, and R. Weiss. LSC white paper on detector research and development. Technical Report T990080, LIGO, 1999.
- [58] H Luck et al. Proceedings of the 3rd Edoardo Amaldi conference on Gravitational waves, 2000. ed S Meshkov (Melville, NY: AIP), p 119.
- [59] W. O. Hamilton. Real performance and real promise: Resonant mass detectors of gravitational waves. Proceedings of the Seventh Marcel Grossmann Conference on General Relativity and Gravitation, <http://sam.phys.lsu.edu/Papers/MG7PROCS.PDF>.
- [60] G M Harry, A M Gretarsson, P R Saulson, S E Kittelberger, S ED Penn, W J Startin, S Rowan, M M Fejer, D R M Crooks, G Cagnoli, J Hough, and N Nakagawa. Thermal noise in interferometric gravitational wave detectors due to dielectric optical coatings. *Classical and Quantum Gravity*, 19:897–917, 2002.
- [61] Janeen Hazel, Seiji Kawamura, and Fred Raab. Suspension preliminary design. Technical note T960074, LIGO, 1996.

- [62] Jay Heefner. Private communication.
- [63] Y. L. Huang and Peter R. Saulson. Dissipation mechanisms in pendulums and their implications for gravitational wave interferometers. *Review of Scientific Instruments*, 69:544–553, 1998.
- [64] S A Hughes. Listening to the universe with gravitational-wave astronomy. *Annals of Physics*, 303(1):142–178, 2003.
- [65] S. A. Hughes and K. S. Thorne. Seismic gravity-gradient noise in interferometric gravitational-wave detectors. *Physical Review D*, 58(12):122002, 1998.
- [66] M. N. Inci and T. Yoshino. A fiber-optic wavelength modulation sensor based on tantalum pentoxide coatings for absolute temperature measurements. *Optics REview*, 7(3):205–208, May-Jun 2000.
- [67] W. B. Jackson, N. M. Amer, A. C. Boccara, and D. Fournier. *Applied Optics*, 20:1333, 1981.
- [68] F. Jansen, M. A. Machonkin, N. Palmieri, and D. Kuhman. Thermomechanical properties of amorphous silicon and nonstoichiometric silicon oxide films. *Journal of Applied Physics*, 62:4732, 1987.
- [69] R. Kato, A. Maesono, and R. P. Tye. Thermal conductivity measurement of submicron-thick films deposited on substrates by modified ac calorimetry. *International Journal of Thermophysics*, 22(2):617–629, 2001.
- [70] Seiji Kawamura and Janeen Hazel. Small optics suspension final design (mechanical system). Technical note T970135, LIGO, 1997.
- [71] Bill Kells. Core optics components requirements. Engineering report E950099, LIGO, 1996.
- [72] Bill Kells. Private communication, 2003.
- [73] A. L. Kimball. Internal friction theory of shaft whirling. *Physical Review*, 21:701–703, June 1923. Rapid communication.
- [74] A. L. Kimball and D. E. Lovell. Internal friction in solids. *Physical Review*, 30:948–959, 1927.

- [75] Peter King. Private communication.
- [76] Charles Kittel. Temperature fluctuation: an oxymoron. *Physics Today*, page 93, May 1988.
- [77] Herwig W. Kogelnik and T. Li. Laser beams and resonators. *Applied Optics*, 5:1550–1567, 1966.
- [78] L D Landau and E M Lifshitz. *Statistical Physics (volume 5)* §112.
- [79] Brian Lantz. *Quantum Limited Optical Phase Detection in a High Power Suspended Interferometer*. PhD thesis, M.I.T., Cambridge, MA, 1999. P990003.
- [80] Mike Lauer. Private communication, 1999.
- [81] S-M Lee and David G Cahill. Thermal conductivity of sputtered oxide films. *Physical Review B*, 52:253, July 1995.
- [82] Yuri Levin. Internal thermal noise in the LIGO test masses: A direct approach. *Physical Review D*, 1998.
- [83] Bingcheng Li, Zhaoxin Zhen, and Shunhua He. Modulated photothermal deformation in solids. *Journal of Physics C*, 24:2196–2201, 1991.
- [84] Daqun Li, Dennis Coyne, and Jordan Camp. Optical contamination screening of materials with a high-finesse fabry-perot cavity resonated continuously at 1.06 m wavelength in vacuum. *Applied Optics-OT*, 38(25):5378–5383, 1999.
- [85] David R. Lide, editor. *CRC Handbook of Chemistry and Physics*, volume 77th ed. CRC Press.
- [86] LIGO. LSC subsystem final design. Technical Report T980068, 1998.
- [87] Yuk-Tung Liu. Dynamical instability of new-born neutron stars as sources of gravitational radiation. *Physical Review D*, 65(12):124003, 2002.
- [88] Yuk Tung Liu and Kip S. Thorne. Thermoelastic noise and homogeneous thermal noise in finite sized gravitational-wave test masses. *Physical Review D*, 62:122002, 2000.
- [89] G. W. McLellan and E. B. Shand. volume 3rd ed. McGraw-Hill, New York, 1984. Ch. 2.
- [90] Memsnet.org. <http://www.memsnet.org/material/>.

- [91] N Nakagawa, B A Auld, Eric Gustafson, and M M Fejer. Estimation of thermal noise in the mirrors of laser interferometric gravitational wave detectors: Two point correlation function. *Review of Scientific Instruments*, 68(9):3553, 1997.
- [92] N Nakagawa, A M gretarsson, Peter T. Beyersdorf, and M M Fejer. Estimating the off resonance thermal noise in mirrors, Fabry-Perot interferometers, and delay lines: The half infinite mirror with uniform loss. *Physical Review D*, 65:082002, 2002.
- [93] N Nakagawa, A M gretarsson, Eric K Gustafson, and M M Fejer. Thermal noise in half-infinite mirrors with nonuniform loss: A slab of excess loss in a half-infinite mirror. *Physical Review D*, 62:102001, 2001.
- [94] Kenji Numata. *Direct measurement of mirror thermal noise*. PhD thesis, University of Tokyo, 7-3-1 Hongo, Bunkyo-ku, Tokyo 113-0033, Japan, 2002.
- [95] M. A. Olmstead, N. M. Amer, and S. Kohn. Photothermal displacement spectroscopy: An optical probe for solids and surfaces. *Applied Physics A*, 32:141–154, 1983.
- [96] Opto-Technological Laboratory. <http://www.optotl.ru/BK7Eng.htm>.
- [97] Richard O'Shaughnessy. Private communication.
- [98] B. J. Owen. Search templates for gravitational waves from inspiraling binaries: Choice of template spacing. *Physical Review D*, 53(12):6749–6761, 1996.
- [99] A. Pai, S.V. Dhurandhar, P. Hello, and J.-Y. Vinet. Radiation pressure induced instabilities in laser interferometric detectors of gravitational waves. *The European Physical Journal D*, 8(3):333–346, 2000.
- [100] Teviet Creighton Patrick R. Brady. Searching for periodic sources with LIGO. II. Hierarchical searches. *Physical Review D*, 61:082001, 2000.
- [101] Steven D. Penn, Peter H. Sneddon, Helena Armandula, Joseph C. Betzwieser, Gianpietro Cagnoli, Jordan Camp, D. R. M. Crooks, Martin M. Fejer, Andri M. Gretarsson, Gregory M. Harry, Jim Hough, Scott E. Kittelberger, Michael J. Mortonson, Roger Route, Sheila Rowan, and Christophoros C. Vassiliou. Mechanical loss in tantala/silica dielectric mirror coatings. *gr-qc/0302093*, 2003.

- [102] Shanti Rao. Scattered light control in LIGO. Technical note G000008, LIGO, 2000. Presented at the 2000 Aspen winter conference on gravitational waves.
- [103] Shanti Rao. Mode matching calculator. Technical note T020035, LIGO, 2002.
- [104] F. Reif. *Fundamentals of statistical and thermal physics*. ISBN 07-051800-9. McGraw-Hill, New York, 1965. p. 213.
- [105] Anthony Rizzi. Will the level of seismic noise at livingston observatory interfere with the detection of gravity waves from binary inspirals? *Review of Scientific Instruments*, 73(11):3946–3956, 2002.
- [106] M. De Rosa, L. Conti, M. Cerdonio, M. Pinard, and F. Marin. Experimental measurement of the dynamic photothermal effect in fabry-perot cavities for gravitationalwave detectors. *Physical Review Letters*, 89(23):237402, 2002.
- [107] Maurizio De Rosa. Private communication. 2003.
- [108] Sheila Rowan and Marty Fejer. Thermoelastic dissipation in inhomogenous media: loss measurements and thermal noise in coated test masses. Presented at the April 2003 LSC meeting. LIGO document G030144.
- [109] Garry Sanders. Scientific operation of LIGO. Presentation G030181, LIGO, 2003.
- [110] Peter R. Saulson. Thermal noise in mechanical experiments. *Physical Review D*, 42(8):2437–2445, 1990.
- [111] Peter R. Saulson. *Fundamentals of Interferometric Gravitational Wave Detectors*. World Scientific, ISBN: 981-02-1820-6, 1994. § 7.9.
- [112] Joe Suina and Dale Ouimette. Length sensing and control photodiode circuit. Technical Report D980454, 1998.
- [113] Inc. The Aluminum Association. *Aluminum standards and data*. 1979.
- [114] Inc. The MathWorks. *Matlab and PDETool*. The MathWorks, Inc., Natick, MA, version 6.5 edition, 2002.
- [115] ThorLabs, Inc. Det110 data sheet. <http://www.thorlabs.com/Thorcat/2100/2199-s01.pdf>.

- [116] K. S. Thorne and C. J. Winstein. Human gravity-gradient noise in interferometric gravitational-wave detectors. *Physical Review D*, 60(8):082001, 1999.
- [117] Kip Thorne. Probing black holes and relativistic stars with gravitational waves. 1997. gr-qc/9706079.
- [118] Chuen-Lin Tien, Cheng-Chung Jaing, Cheng-Chung Lee, and Kie-Pin Chuang. Simultaneous determination of the thermal expansion coefficient and the elastic modulus of Ta₂O₅ thin film using phase shifting interferometry. *Journal of Modern Optics*, 47(10):1681–1691, 2000.
- [119] K. Tsubono. Gravitational wave experiments, proc. 1st edoardo amaldi conf., 1995. ed S Meshkov (Singapore: World Scientific), p112.
- [120] Michele Vallisneri. Prospects for gravitational-wave observations of neutron-star tidal disruption in neutron-star-black-hole binaries. *Physical Review Letters*, 84(16):3519–3522, 2000.
- [121] Steve Vass. Private communication.
- [122] Xinwei Wang, Hanping Hu, and Xianfan Xu. Photo-acoustic measurement of thermal conductivity of thin films and bulk materials. *Transactions of the ASME*, 123:138, Feb 2001.
- [123] Phil Willems. Private communication. 2003.
- [124] Phil Willems and Dan Busby. Report to the down-select committee. Technical Report T030087, LIGO, 2003.
- [125] Wolfram Research Inc. *Mathematica*. Wolfram Research, Inc., Champaign, Illinois, version 4 edition, 1999.
- [126] Z L Wu, M Reichling, X-Q Hu, K Balasubramanian, and K H Guenther. Absorption and thermal-conductivity of oxide thin-films measured by photothermal displacement and reflectance methods. *Applied Optics - OT*, 32(28):5660, 1993.
- [127] J. H. Zhao, T. Ryan, and P. S. Ho. Measurement of elastic modulus, Poisson ratio, and coefficient of thermal expansion of on-wafer submicron films. *Journal of Applied Physics*, 85:6421, 1999.
- [128] Eric D. Black. How to Measure Braginskii's Photo-Thermal Effect. Technical Report T000001, LIGO, 2000